ELECTRICAL RESISTIVITY VARIATIONS AND FAULT CREEP

BEHAVIOR ALONG STRIKE-SLIP FAULT SYSTEMS

by

David V. Fitterman

Geoph. Eng. Colorado School of Mines

Golden, Colorado

(1969)

SUBMITTED IN PARTIAL FULFILLMENT
OF THE REQUIREMENTS FOR THE
DEGREE OF DOCTOR OF
PHILOSOPHY

at the

MASSACHUSETTS INSTITUTE OF TECHNOLOGY

October, 1974
(≤ February 1975

Signature of Author..
    Department of Earth and Planetary Sciences, Oct., 1974

Certified by..
    Thesis Supervisor

Accepted by..
    Chairman, Departmental Committee on Graduate Students

ELECTRICAL RESISTIVITY VARIATIONS AND FAULT CREEP BEHAVIOR ALONG STRIKE-SLIP FAULT SYSTEMS

by

David V. Fitterman

Submitted to the Department of Earth and Planetary Sciences

7 October 1974

in Partial Fulfillment of the Requirements for the

Degree of Doctor of Philosphy

ABSTRACT

The strong stress dependence of the electrical resistivity of rocks suggests the monitoring of earth resistivity to detect stress changes due to tectonic motion. This work considers actual observations of resistivity changes during creep events, and theoretical calculations of resistivity changes around a stressed strike-slip fault to see if detectable resistivity variations are associated with these types of tectonic motions. Laboratory measurements on the effect of stress on the resistivity of clays were also carried out to supplement the existing data on rocks and to allow modelling of stress effects on weathered near surface and fault gouge materials.

A small-scale resistivity monitor was installed along the San Andreas fault at Melendy Ranch where active creep activity has been observed. No resistivity variations which could be attributed to creep activity were detected even when sensitivities of 0.005% were employed. Long term resistivity variations O(1%/year) were noted, and can be explained by the temperature variations of the ground.

The laboratory studies on clays, which more closely represent the material in the creep zone, showed the resistivity-porosity relationship of clay was similar to that of rock, but that resistivity changes during triaxial loading were quite different from that of rock. Resistivity variations of only 5-25% were observed on clay samples strained to failure with resistivity increasing for compressional tests and decreasing for extensional tests.

These results are attributed to alignment of the clay particles perpendicular to the maximum stress direction. The negative field results can be explained by the assumption that the clay particle alignment is close to a steady state and any changes occuring are confined to a narrow zone about the fault plane.

A simple model of a strained strike-slip fault is analysed to see if observable resistivity variations would be produced by strain accumulation. Fault displacement is found to produce only pure shear loading. Estimates of the effect of this stress system on rock resistivity are made by using resistivity data measured during isotropic and triaxial loading. For a model of the San Andreas fault, 50cm of fault displacement are found to produce variations of resistivity measured on the surface of about 1%. Resistivity variations produced by non-tectonic processes could mask this variation.

The model considered requires long periods of time (>20 years) to produce barely observable resistivity variations. This is in contrast with reported observations of large resistivity changes (>20%) developing in a period of several months before an earthquake. If more observational data confirm pre-earthquake resistivity changes, very different models must be considered to explain such results.

Thesis Supervisor: Theodore R. Madden
Title: Professor of Geophysics

ACKNOWLEDGEMENTS

While at M.I.T. it has been my pleasure to work with Professor T. R. Madden. His physical insight has been invaluable in trying to unravel the numerous problems encountered, and his many suggestions and criticisms are truly appreciated.

Dr. R. T. Martin was most helpful with the work performed on clays. The M.I.T. Soil Mechanics Division of the Department of Civil Engineering graciously provided laboratory space and equipment for these tests. Mr. Ernst Shmid's advice and help in design and construction of the test cell were sound and thorough.

George Keough, Sam Hendyrx, Dave Riach, and Jacques Hurst are thanked for their help in the construction of various instruments.

Discussions with Yed Angoran, Ray Brown, Ken Anderson, and Paul Kasameyer were most helpful. In particular, Paul helped put many things into their proper perspective.

Robert Burford of the U.S. Geological Survey kindly furnished data on creep event times and displacements. Gordon Green, also of U.S.G.S.-N.C.E.R., made arrangements for monthly servicing of the Melendy Ranch resistometer.

Without the encouragement of my parents the difficult times at M.I.T. would have been insurmountable.

Our dear friend Elizabeth Romanow Lev provided metaphysical advice at many critical times, and to her I dedicate

5

Figure 5-4.

My best friend and wife, Ruth was a source of strength. Her conscientious help in typing and editing the manuscript was indispensable.

Sara Brydges, Dorothy Frank, and John Laporta are thanked for their help in typing.

TABLE OF CONTENTS

LIST OF FIGURES

FIGURE   PAGE

FIGURE   PAGE

FIGURE   PAGE

LIST OF TABLES

LIST OF ABBREVIATIONS

BBC   Boston blue clay

CID   isotropically consolidated, drained triaxial test

CIU   isotropically consolidated, undrained triaxial test

OCR   overconsolidation ratio $\bar{\sigma_c}/\bar{\sigma}_{c_{max}}$

PRN   pseudo-random network

SFI   shear failure index $(\sigma_1-\sigma_2)/(\sigma_1-\sigma_2)_{failure}$

CHAPTER 1:   ELECTRICAL RESISTIVITY AND THE EARTHQUAKE

PREDICTION PROBLEM

> There was a time when the earthquake was
> equally enveloped in mystery, and was forecast
> in the enigmatic phrases of the astrologer and
> oracle; and now that it too has passed from
> the shadow of the occult to the light of
> knowledge, the people of the civilized earth ---
> the lay clients of the seismologists --- would
> be glad to know whether the time has yet come
> for a scientific forecast of the impending
> tremor. The outlook for earthquake forecasting
> is my theme for today.[1]

1.1   Introduction

While current interest in the problem of earthquake

prediction is intense, the idea is far from new. In the

early 1900's there was much activity in trying to find

methods of predicting earthquakes. Much of the work focused

on finding periodicity of earthquakes and correlations with

tidal stresses (Cotton, 1923; Hodgson, 1924). These were

rather formidable undertakings considering that all calcula-

tions were done by hand. The results were far from conclu-

sive. G. K. Gilbert (1909) took a broader look at the prob-

lem believing that the quality of an earthquake forecast was

of great importance with the quality being measured by accu-

racy of time and place. With these points in mind he tried

to determine the factors controlling both variables.

---

[1]G.K. Gilbert, Earthquake forecasts, Science (New Series),
29, 121-138, 1909.

Gilbert felt the following factors were important in predicting the earthquake location: 1) previous locations, 2) proximity of high mountain ranges and rift zones, and 3) the strength of geologic formations. The time of the event was felt to be influenced by: 1) rhythm, 2) alternation, 3) trigger, and 4) prelude. Rhythm referred to possible periodicities in earthquake sequences. The notion that once an earthquake has occurred in an area it is more likely for the next earthquake to be somewhere else is alternation. Some of the mechanisms proposed for trigger were tides, snow pressure, barometric pressure, and wandering of the earth's axis. Prelude is the most interesting of all.

> It depends on the recognition of premonitory signs, and also, to some extent, on the recognition of the earliest phases of the event itself. If they are veritable preludes, connected in a systematic way with the mechanisms of earthquakes, they are probably analogous to the cracklings and crepitations observed in strained beams and strained blocks before rock collapse occurs.[2]

Geophysicists are to the point where they have ideas about what kinds of precursors to look for. Measurements are being made to detect these precursors, and in some cases satisfactory predictions have been made.

This thesis is concerned with an aspect of using electrical resistivity variations for earthquake prediction. In particular, it explores the resistivity variations associated

---

[2]Op. cit.

with creep events and long term strain accumulation along strike-slip faults. A discussion of the basis for using resistivity variations for earthquake prediction is presented, followed by an outline of the thesis.

1.2 Resistivity, Travel Time Anomalies, and Dilatancy

Brace and Orange (1968a) observed a drastic change in the electrical resistivity of stressed rocks as failure was approached. As a crystalline rock is stressed cracks are closed causing the resistivity to increase. Crack closure continues until the stress in the rock is about half that required for failure. At this point new void space is created by the opening of pre-existing cracks and the formation of new cracks. The rock is said to have dilated. If enough pore fluid is available to fill these new voids, a dramatic decrease in resistivity results. If the new void space is only partially saturated a resistivity decrease will also result. This is because the newly formed cracks are smaller than those already present, and they preferentially attract water due to capillary action resulting in an increased surface conduction contribution to the total conductivity. If dilatancy occurs prior to earthquakes, resistivity changes seem like a plausible prediction tool.

There have been phenomena observed before earthquakes which can be explained by dilatancy. Variations in the ratio of compressional wave to shear wave velocities (V_p/V_s)

were first reported prior to earthquakes in the Garm region of the Tadzhik Soviet Socialist Republic (Nersesov et al., 1969; Semenov, 1969). The ratio V_p/V_s was found to decrease from its background level for a period and return to its normal value. Shortly after the return a large earthquake occurred. The duration of the anomalous period appears to be proportional to the magnitude of the earthquake. These results were first explained by a dilatancy model by Nur (1972) and Scholz et al. (1973).

The model relies on the fact that the compressional wave velocity of dry rock is considerably less than that of saturated rock, while the shear wave velocity is not greatly affected by the degree of saturation (Nur and Simmons, 1969). The hypocentral zone is hypothesized to dilate as it is stressed causing undersaturation and a drop in V_p while V_s is relatively unaffected. Under-saturation also creates a region with abnormally low pore pressure which starts fluid flow into the dilatant zone. The rise in pore pressure decreases the strength of the rock and an earthquake results.

Scholz et al. (1973) have suggested that the resistivity of the dilatant zone decreases prior to the earthquake. This may well happen, but the electrical behavior of tectonically stressed rocks must be examined. In addition, the size of the dilatant zone is important. If the zone is small, detection of precursory phenomena from surface measurements may not be possible. These are some of the problems considered

in this work.

1.3 Outline of the Thesis

The thesis is divided into two parts. The first part is concerned with the electrical resistivity of clays and small-scale resistivity measurements as related to creep events. The second part considers the electrical behavior of rocks and the resistivity changes due to stress accumulation on a strike-slip fault. Two different types of geologic materials which behave in dramatically different ways are involved in these cases.

The factors influencing the electrical resistivity of clays are studied in Chapter 2. The effects of pore fluid conductivity, porosity, and stress are considered.

The third chapter presents the results of a small-scale resistivity monitor along the San Andreas fault at Melendy Ranch. Observations during creep events are presented and explained using laboratory findings on clay resistivity. The problem of surface effects influencing resistivity measurements is analyzed.

Chapter 4 is a review of the electrical behavior of rocks. Of primary concern is the effect of stress on resistivity. This chapter also serves as a comparison to show the vast difference between clay and rock resistivity properties. Estimates of the effect of pure shear on rock resistivity are made.

Chapter 5 presents a theoretical analysis of resistivity variations due to tectonic motion around a strike-slip fault. Resistivity variations measurable by a surface resistivity monitor are computed.

CHAPTER 2: ELECTRICAL RESISTIVITY OF CLAYS

2.1 Introduction

Rock and clay represent two extremes of the spectrum of geologic materials. The former is strong with its physical properties greatly influenced by the myriad of tiny cracks running through it. The mineral grains are firmly connected to each other but the crack shapes and sizes can change in response to applied stresses. Clay, on the other hand, is composed of particles which are not interconnected. The surface charge on the particles produce electric fields which allow the particles to interact with each other (van Olphen, 1963). Stresses applied to rocks will open and close cracks depending upon their orientation (Nur, 1969). Clays, on the other hand, will undergo rearrangement of the particles due to stressing (Martin and Ladd, 1970).

The mobility of the clay particles, on one side, and the rigidly fixed interrelationship of the rock cracks, on the other, create vast differences in their mechanical and electrical properties. Clay, for example, deforms plastically at low stresses because the clay particles are free to move about (Worral, 1968). Rock, at moderate crustal stresses, behaves elastically because of the interconnectivity of the mineral grains. In both cases, the electrical properties are governed by the behavior of the pore size distribution, but the distributions behave differently in response to a given

stress system.

The properties of fault gouge, which are influential in the study of fault creep, probably lie somewhere between that of rock and clay. While the electrical behavior of rock subjected to various stress systems is understood rather well (Brace et al., 1965; Brace and Orange, 1968a and 1968b) the same can not be said for clay. A great deal of work has been done to understand the effect of clay on the electrical properties of rocks (Winsauer and McCardell, 1953; Hill and Milburn, 1956; Waxman and Smits, 1968; Waxman and Thomas, 1974). The results presented in this chapter are different in that the effect of stress on the resistivity of a pure clay system is explored. These new results combined with previous work done on rocks provide bounds for the electrical behavior of fault gouge. The electrical resistivity variations observed during creep events will later be explained using the results of this chapter.

Clay resistivities were measured with two types of experiments, consolidation tests and triaxial loading tests. The consolidation tests provide information about the effect of porosity and pore fluid salinity on resistivity, while the triaxial experiments explore what happens to the clay resistivity during failure.

Models of clay conductivity using the random interconnection of the clay pore passages were developed in order to investigate the effects of porosity and fabric on the

electrical conductivity.

2.2 Description of One-Dimensional Consolidation Experiments

One-dimensional consolidation tests are a standard test used by soil engineers to determine how much and how fast a structure will settle. A sample of soil is placed in a cylinder, and loaded in one direction. As water is squeezed out of the sample, changes in the sample length are recorded. After the deformation is complete, the load is increased and the deformation again monitored. This process is repeated until the stress range of interest is covered. If the sample impedance is also measured during the test, it is possible to compute the resistivity-porosity (ρ-n) relationship for the clay.

2.2.1 Equipment

Consolidation experiments were performed using the oedometer (a device which measures changes in volume) shown in Figure 2-1. The cell consists of a plastic cylinder and piston with drainage ports at both ends. Porous stainless steel plates with 2 μm pores provided drainage paths for the pore fluid, as well as serving as electrodes for measuring the sample impedance. The sample length, impedance, and temperature were measured as a constant load was placed on the sample. The sample length was measured with a precision of .001". The impedance was measured with a precision of better than one part
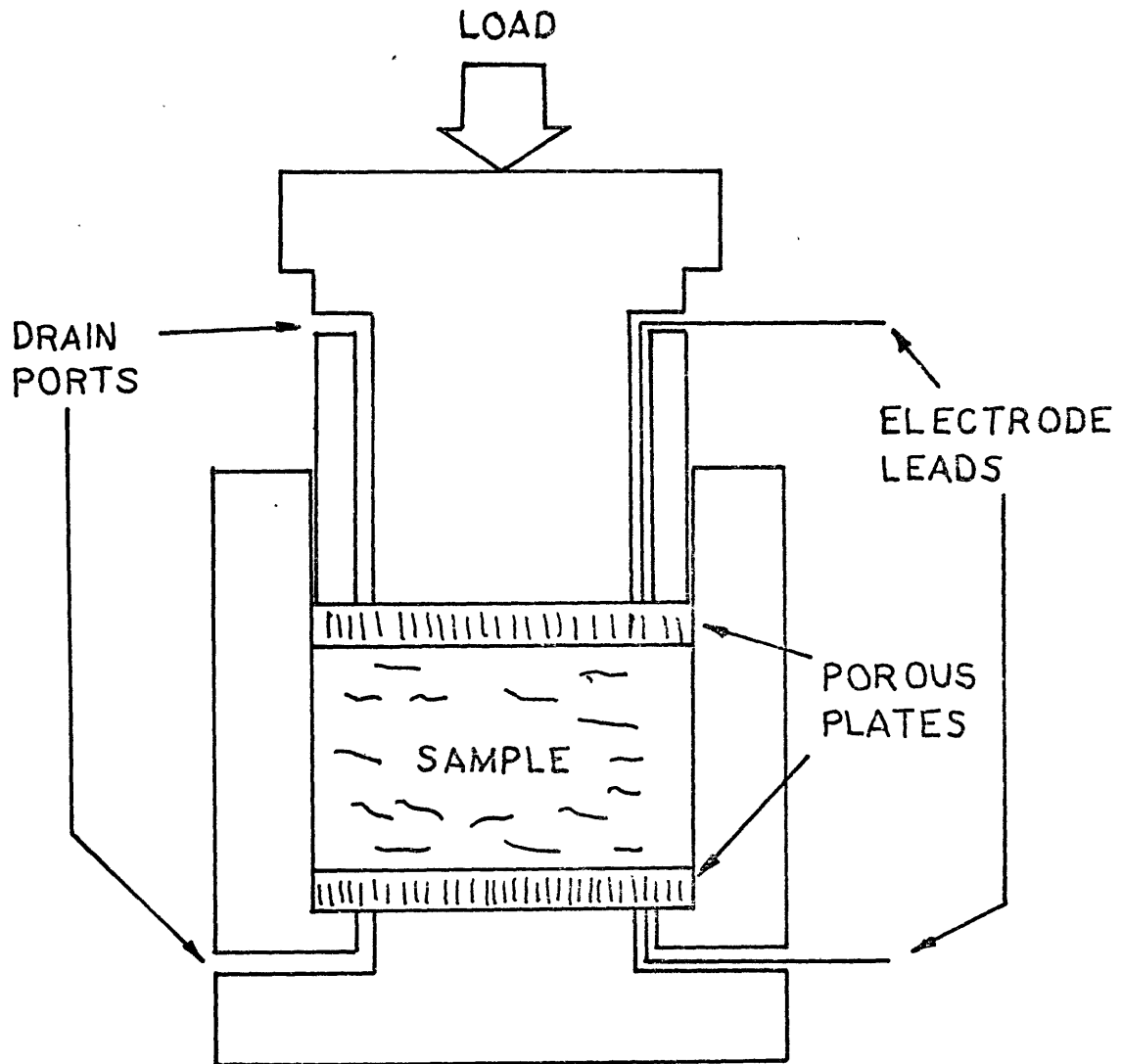
FIGURE 2-1 CONSOLIDATION OEDOMETER

in 10^3. A 5 hz constant current was passed through the sample
and a dummy impedance (a parallel resistor-capacitor combina-
tion). The dummy impedance was adjusted until the difference
in voltage across the sample and the dummy impedance was mini-
mized. Phase shifts of the sample impedance were typically
less than 0.02 radians. The phase shift remained constant
throughout any one experiment. To the accuracy of the measure-
ments, the complex part of the impedance is negligible.

2.2.2 Sample Preparation and Procedures

Samples of South Carolina kaolin were prepared by two
methods. In the first method, called wet-up, the oedometer
is filled with the kaolin in a dry powdered form. Pore fluid
is then allowed to slowly enter from the bottom of the cham-
ber. The second procedure starts with a slurry of the kaolin
and pore fluid which is poured into the oedometer. Initial
porosities of 80-85% are typical for the slurry preparation
while the wet-up procedure gives lower initial porosities
(55-65%). Tests were run using tap water and 0.1 M KCl to
examine the effect of pore fluid resistivity. The clay fab-
ric produced by the two preparation methods is quite differ-
ent. Samples prepared by the wet-up method have rather ran-
dom particle orientation, while the slurry preparation allows
preferential horizontal alignment of the clay particles
(Martin and Ladd, 1970).

After the sample was in the oedometer, a load (typically

$0.2-0.3$ kg/cm^2) was applied. Impedance and length were moni-
·tored until deformation was complete. The load was then
doubled and the process repeated. Final loads were between
9 kg/cm^2 and 19 kg/cm^2. Following the last loading, the sam-
ple was removed and its water content determined. From the
water content and final length, the volume of the clay
particles can be computed. The sample volume and clay particle
volume are used to calculate the porosity during loading.

2.3 Consolidation Results

2.3.1 Resistivity and Porosity Changes During Consolidation

The results of a consolidation experiment are shown in
Figure 2-2. Plotted on logarithmic coordinates are resistiv-
ity and porosity. Resistivity is seen to increase with
decreasing porosity. There are, however, small jogs in the
curve where a small porosity decrease is accompanied by a
resistivity decrease. These points correspond to the
application of a new load (arrows in diagram) and are due to
incomplete saturation of the sample.

The effect of incomplete saturation can be removed as
follows. The horizontal axis represents total porosity, i.e.,
saturated and unsaturated voids. The electrical measurement,
however, is sensitive only to fluid filled pores, the effective
porosity, which is the product of the total porosity and the
degree of saturation. To get the curves plotted against the
effective porosity they should be shifted to the left. The
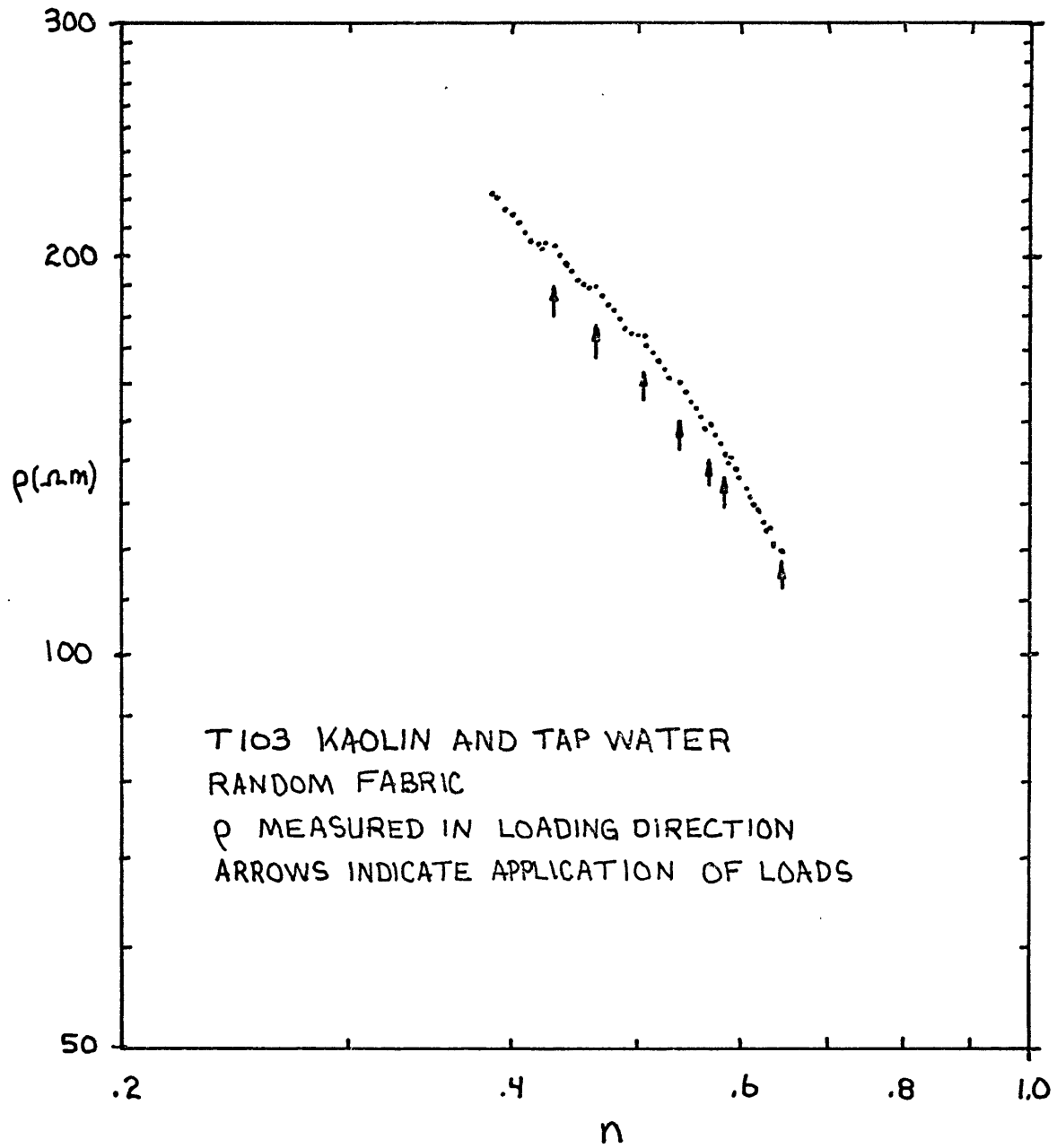
FIGURE 2-2   RESISTIVITY VS. POROSITY FOR
              RANDOM FABRIC KAOLIN AND TAP WATER

procedure used to correct the data assumes that the final data point is completely saturated. Data from previous loading segments are shifted horizontally to the left (decreasing porosity) until they form a smooth continuation of the last data segment. The remaining data segments are treated in a similar manner. From this procedure, inital saturation was found to be 93% for wet-up samples and 98% for slurry formed samples.

Once the data are corrected for saturation effects, the pore fluid resistivity (ρ_o) is estimated by extrapolating the data back to a porostiy of 1.0. In Figure 2-3 are shown the results of four experiments: two oriented and two random fabric samples with pore fluids of tap water and 0.1 M KCl. The data are normalized to their pore fluid resistivity for comparison. Also shown is the line corresponding to

$$\rho = \rho_o n^{-m}$$ 2-1

with m = 2 which has been found to describe the resistivity-porosity behavior of rocks (Archie, 1942; Brace et al., 1965). The samples prepared with tap water have lower formation factors (ρ/ρ_o) than those prepared with 0.1 M KCl by 10-40%. Oriented fabric samples are more resistive by a factor of 1.7 to 2.3 than samples with random fabric. The random fabric sample with 0.1 M KCl follows the square law quite well until lower porosities are reached, while the random tap water
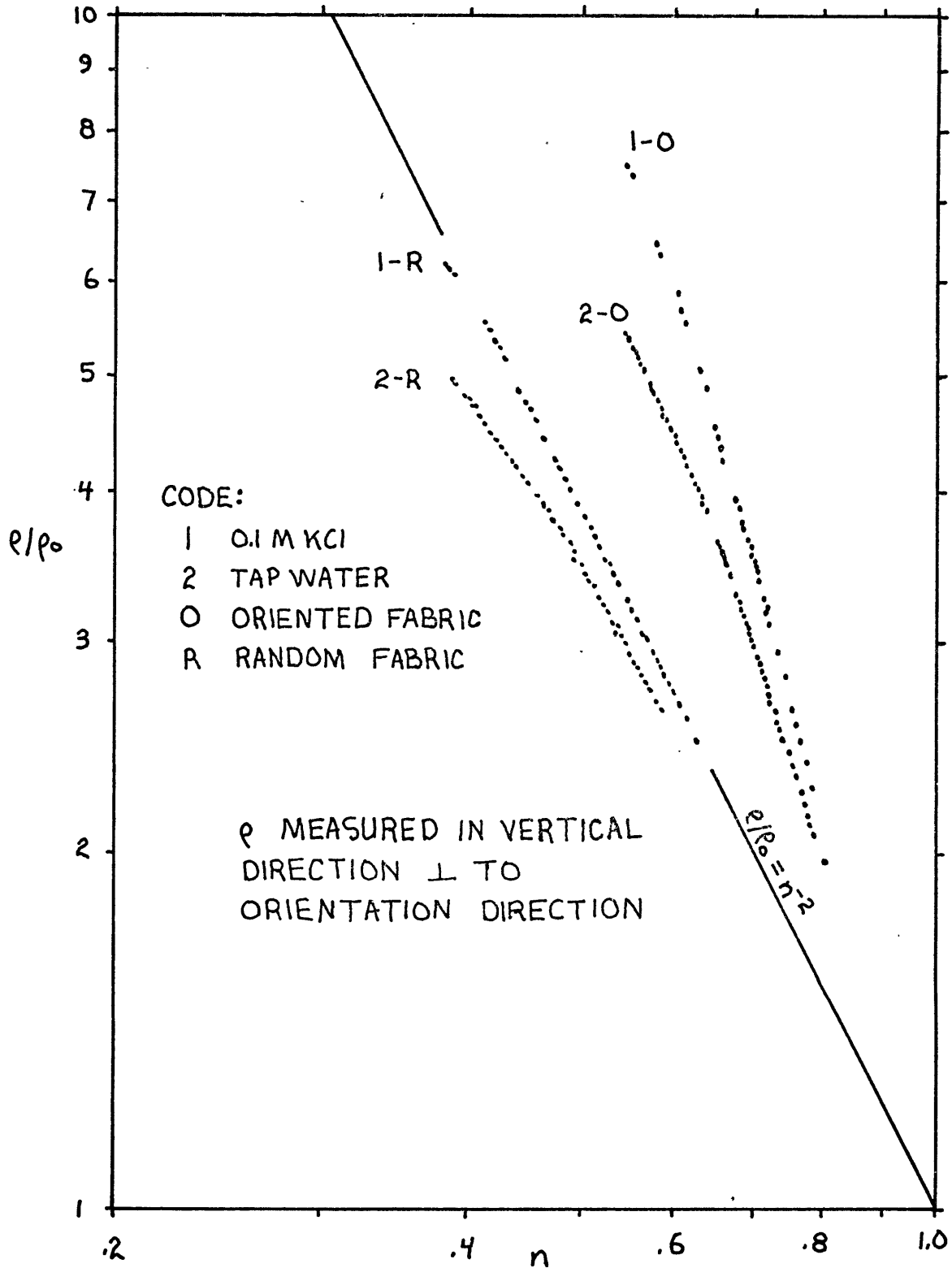
FIGURE 2-3 FORMATION FACTOR VS. POROSITY
FOR KAOLIN

sample is just below the square law. The oriented samples, whose resistivity was measured perpendicular to the direction of particle orientation, are significantly more resistive than the square law prediction.

2.3.2 Conductivity and Pore-Size Distribution

Electrical conduction in clays is composed of a volume conduction component through the pore fluid and a surface conduction component due to the excess of ions associated with the charged clay particles (Winsauer and McCardell, 1953). The volume conductance is proportional to the fluid conductivity and the area of the pore, while the surface conductivity depends on the square root of the ionic concentration and the zeta potential, the potential of the immobile charge layer associated with the particle. Using estimates of 50-75 mV for the zeta potential (Street and Buchanan, 1956) and ionic concentrations of 0.1 M and 0.001 M for the two pore fluids used, the surface conductivity is estimated to be 0.5×10^{-9} Ω^{-1} and 0.5×10^{-10} Ω^{-1} for the 0.1 M KCl and tap water respectively (Madden, 1961). The conductance of a pore is then

$$Y_p = \sigma_o D + 2\sigma_s \qquad 2-2$$

where σ_o is the pore fluid conductivity, D the pore width, σ_s the surface conductivity, and it has been assumed that the pores are of equal length and width. This assumption is suggested by the equidimensional shape of kaolinite particles (Lambe and Whitman, 1969).

We must now know the pore size distribution of the clay, and how to average the pore conductivities in order to obtain an estimate of the clay conductivity. Measurements of clay pore size distributions have been made by Diamond (1970) using a mercury intrusion technique. The method requires that the sample be oven dried which causes some of the larger pores to collapse. A measured cumulative pore volume distribution is shown in Figure 2-4 for a kaolin sample with a fabric similar to that produced by the wet-up preparation. For this sample, the mercury intruded 96% of the pore space. The remaining 4% of the porosity has been assumed to be composed of small pores with diameters between .0045 μm and .02 μm. Addition of the unintruded volume as small diameter pores is justified because the smallest pores require the highest pressure for the mercury to intrude, and are thus the last pores to be filled.

Pseudo-random networks, which are discussed in Appendix C, provide a means of averaging the pore conductivity distribution (Madden, 1972). To use the method the conductivity, σ_i and probability P_i, of the pores must be determined. The first step is to break the cumulative volume distribution into discrete segments. The probability of a particular size pore can be assigned on the basis of number density, or volume density. The number density probability P_{ni} is proportional to the volume of a particular segment divided by the mean pore thickness. From the number density distribution the mean pore thickness is defined by
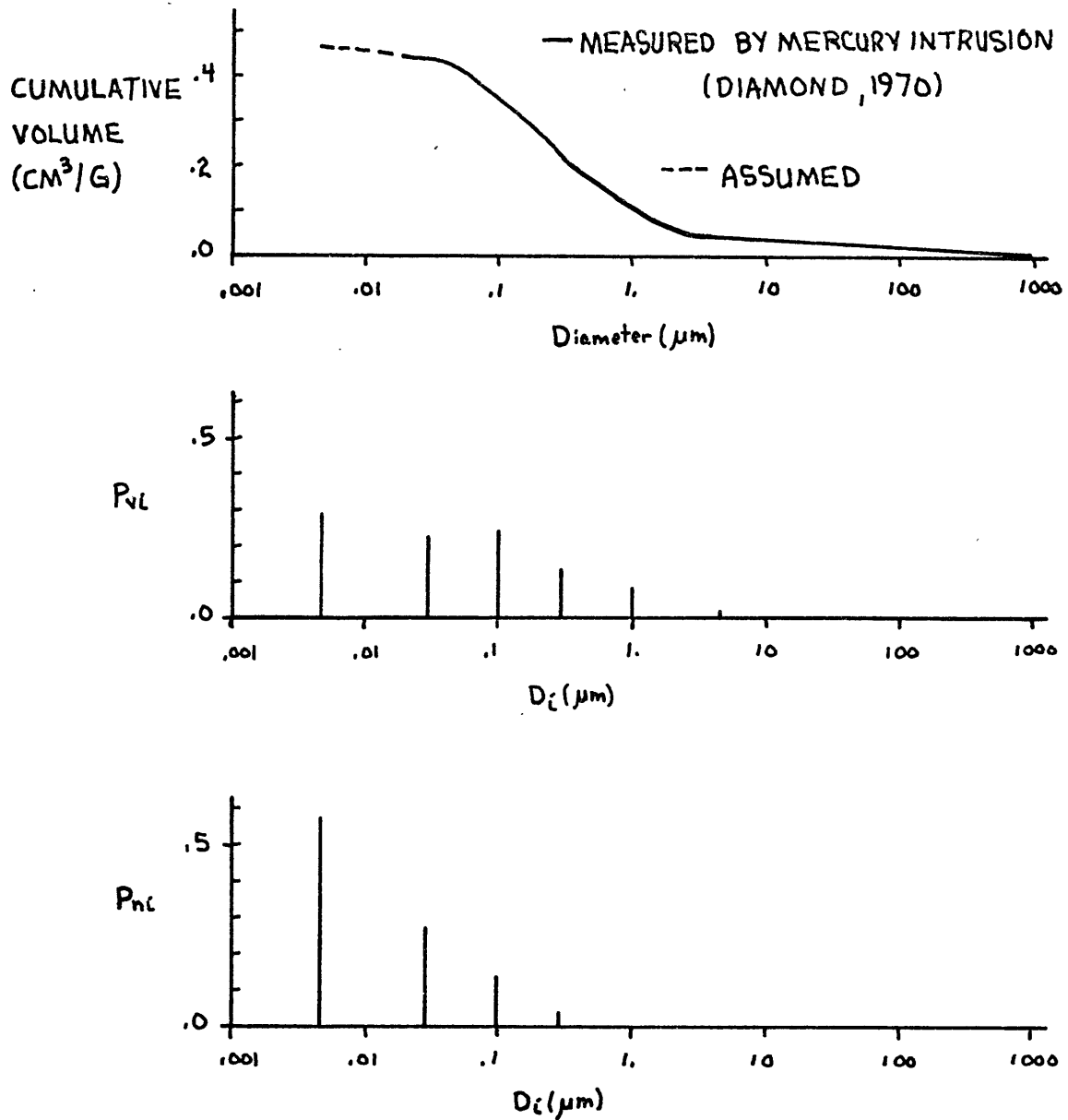
FIGURE 2-4   CUMULATIVE PORE-SIZE DISTRIBUTION
             FOR KAOLIN, AND VOLUME AND NUMBER
             NORMALIZED PORE-SIZE DISTRIBUTIONS

$$\bar{D} = \sum_i P_{ni} D_i \qquad \text{2-3}$$

The average particle thickness T must satisfy the relation

$$\text{Porosity} = \frac{\bar{D}}{\bar{D} + T} \qquad \text{2-4}$$

The volume density probability is the probability of a particular pore-particle combination

$$P_{vi} = \frac{P_{ni}(D_i + T)}{\sum_j P_{nj}(D_j + T)} = \frac{P_{ni}(D_i + T)}{\bar{D} + T} \qquad \text{2-5}$$

The number density normalization assumes an equal volume is associated with each pore, proportional to $\bar{D}+T$, while the volume density normalization assumes that each size pore has a different volume proportional to $D_i + T$ associated with it. The pore conductivities corresponding to these normalizations are

$$\sigma_{ni} = \frac{Y_i}{\bar{D} + T} \qquad \text{2-6}$$

and

$$\sigma_{vi} = \frac{Y_i}{D_i + T} \qquad \text{2-7}$$

for the number and volume density normalizations respectively.
In the low porosity limit of $D_i << T$, which is the case of rocks,
the two methods are equivalent. The normalized pore size
distributions (Figure 2-4) are used to form conductivity
distributions and cascaded using the pseudo-random network
(PRN) formulation.

The results of cascading the two distributions for tap
water and 0.1 M KCl pore fluid are presented in Table 2-1.
As would be expected, the volume normalization gives higher
conductivities than the number normalization because it assigns
a smaller volume of material to the smaller pores than does
the number density normalization. The geometric mean of the
distribution

$$\bar{\bar{\sigma}} = \prod_i \sigma_i^{P_i} \qquad\qquad 2\text{-}8$$

is remarkably close to the cascaded value. The closeness of
the two values has been observed for numerous distributions
suggesting its use as a simple method of computing the
conductivity of a composite material. The geometric mean of
$\bar{\bar{\sigma}}_n$ and $\bar{\bar{\sigma}}_v$ is seen to agree quite well with the measured clay
conductivity of the randomly oriented sample.

The increasing resistivity with decreasing porosity might
be effected by an increase of the pore fluid resistivity during
consolidation. Engelhardt and Gaida (1963) found that the

Table 2-1: Comparison of PRN and Measured Conductivities

D_i (μm)	P_{vi}	P_{ni}	0.1 M KCl		Tap water	
			σ_{vi}	σ_{ni}	σ_{vi}	σ_{ni}
.0045	.292	.576	.150	.0763	.00544	.00276
.03	.223	.259	.499	.430	.0122	.0105
.1	.238	.130	.765	1.40	.0174	.0319
.3	.133	.029	.906	4.18	.0202	.0930
1.	.086	.006	.970	13.9	.0214	.307
4.5	.019	.0003	.993	62.4	.0219	1.38
30.	.008	.00002	1.00	416.	.0220	9.16

$\overline{D}$ = .040μm   n = .555   T = .032μm

Pore Fluid	σ_o	σ_s	$\dfrac{<<\sigma_{vi}>>}{\sigma_o}$	$\dfrac{<<\sigma_{ni}>>}{\sigma_o}$	$\dfrac{\overline{\overline{\sigma}}_{vi}}{\sigma_o}$	$\dfrac{\overline{\overline{\sigma}}_{ni}}{\sigma_o}$	$\dfrac{(\overline{\overline{\sigma}}_{vi}\overline{\overline{\sigma}}_{ni})^{\frac{1}{2}}}{\sigma_o}$	$\dfrac{\sigma_{meas}}{\sigma_o}$
0.1 M KCl	1.0	$.5\times10^{-9}$	.468	.193	.454	.202	.303	.303
Tap water	.022	$.5\times10^{-10}$	.545	.265	.545	.278	.389	.345

Notes: Measured conductivity for random fabric
All conductivities in $\Omega^{-1}m^{-1}$ except σ_s which is in Ω^{-1}.
$<<\sigma_i>>$ is the PRN cascaded conductivity. $\overline{\overline{\sigma}}_i = \prod_i \sigma_i^{P_i}$

pore fluid ion concentration of kaolinite did not change during consolidation. Clays with a much higher cation exchange capacity did undergo a decrease in pore fluid concentration during compaction. The increase of resistivity during consolidation must be due to the pore size distribution changes in response to the applied load. Determination of how the distribution varies based on resistivity and porosity measurements is very non-unique. Pore size distribution measurements of impact-compacted clay indicates that the large pores are closed first increasing the relative abundance of the small pores (Diamond, 1971).

A simple model composed of a fixed conductivity σ_2 = .01, and a variable conductivity σ_1 with probabilities P_2 and P_1 respectively is informative to show that such a trend would explain the observed n^2 conductivity-porosity behavior. The conductance of the medium will be taken as the geometric mean of the distribution and the porosity will be the arithmetic mean. The lower conductivity is kept fixed to represent the lower conductivity limit imposed by a minimum separation behavior of the clay particles. Figure 2-5 shows the values of σ_1 and P_1 necessary to follow the square law. As the porosity decreases, it is necessary for the variance of the distribution to increase by increasing the probability of the smaller conductor in order to follow the square law.
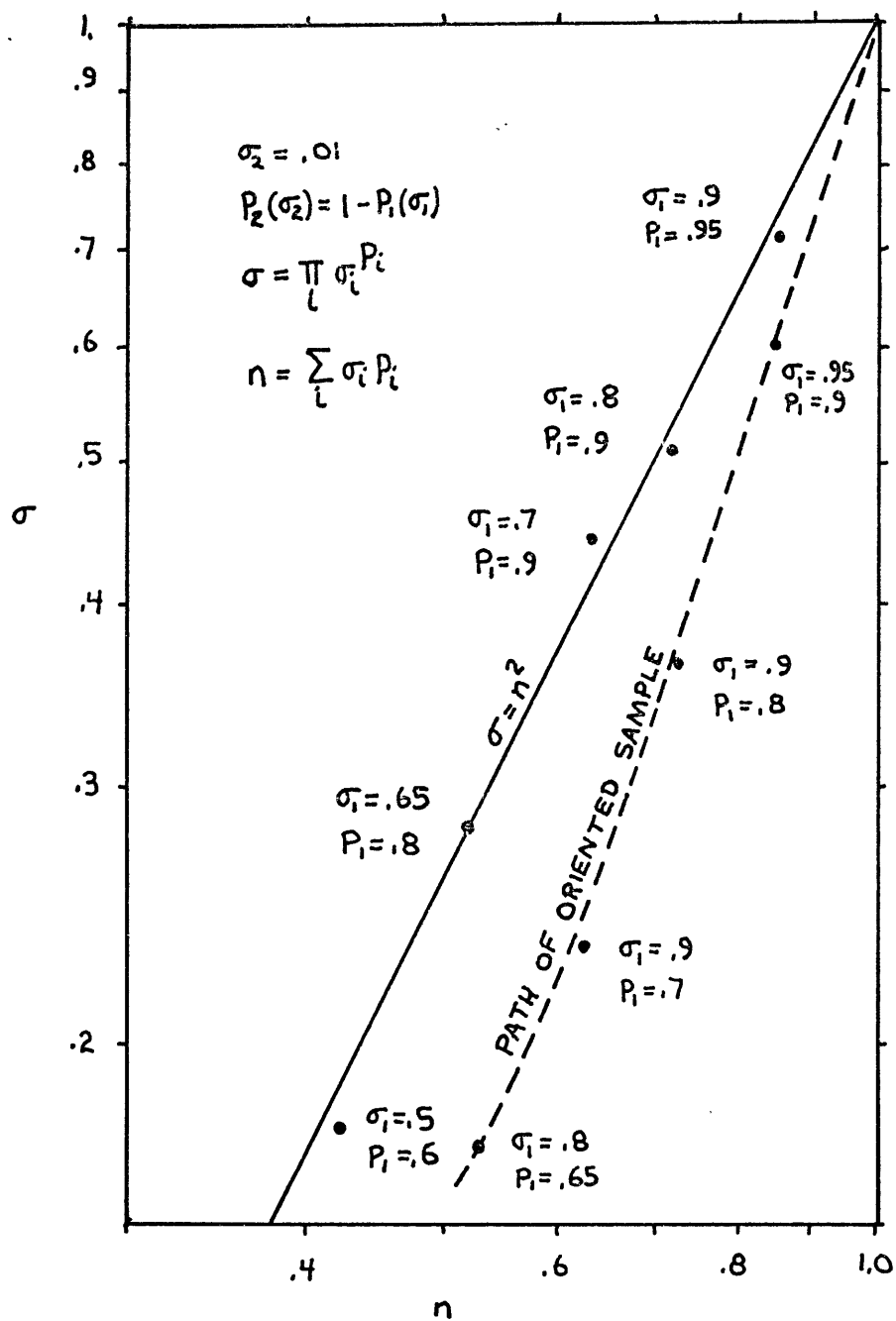
FIGURE 2-5   CONDUCTIVITY AND PROBABILITY OF
TWO CONDUCTOR MODEL

2.3.3 The Effect of Fabric on Resistivity

As was seen from the consolidation results, samples with different fabric had significantly different conductivities. To understand how influential fabric can be on the resistivity of clay, some kaoline samples were prepared using the wet-up and slurry techniques described previously. The fabrics produced are called random-loose (RL) and oriented (O) respectively. In addition a random-packed (RP) fabric was made by using the wet-up procedure on clay which had been tamped before saturating. The consolidated samples were removed from the oedometer and cut into right-rectangular prisms, and their resistivity measured in perpendicular directions. Silver-silver chloride screens covered with moistened blotter paper were used for electrodes. If the blotter covered electrodes were too moist, water was absorbed by the sample and the measurements changed drastically with time. Insufficient moisture on the blotters produced high contact resistance. Measurements were repeated until a stable value was obtained.

The ratio of vertical resistivity (ρ_v) to horizontal resistivity (ρ_h) is called the resistivity anisotropy, A, where the vertical direction is the direction of loading in the oedometer. The oriented fabric has a resistivity anisotropy (A = ρ_v/ρ_h) ranging from 1.6-1.8 (Table 2-2). The random fabrics have an anisotropy of 1.2-1.7, with the best estimate being 1.3. This value is not unity due to the

Table 2-2

Resistivity Anisotropy of Consolidated Clay Samples

Sample	Fabric	$\bar{\sigma}_c$ (kg/cm^2)	(KCL) (mole/ℓ)	ρ_v	ρ_{h1}	ρ_{h2}	$\bar{A}=\rho_v/\rho_h$
T303	O	4	.001	184	98.6	102	1.83
T306	O	4	.001	422	254	261	1.60
T308	RL	4	.001	243	210	203	1.18
T311	RP	4	.001	261	178	191	1.45
T311	RP	4	.001	284	231	235	1.20
T313	RL	4	.01	65.7	42.5	44.3	1.55±.25[§]
T319	RP	4	.01	27.6	16.9	---	1.65±.18[†]
T320	RP	8	.01	31.5	24.5	26.2	1.25
T321	RP	4	.01	35.4	27.3	26.0	1.35
T322	RP	8	.01	39.6	28.5	26.5	1.44
T323	RP	2	.01	37.3	30.6	27.6	1.28
T318*	U	-	---	7.61	5.88	---	1.30±.09[†]

All Resistivities in Ω-m

Fabric Code

O - oriented   to vertical direction

RL - random loose

RP - random packed

U - undisturbed, most likely oriented

*All samples kaolinite except T318 which is Boston Blue Clay, $\bar{\sigma}_c \sim 4.0$ kg/cm^2

[§] 3 samples

[†] 6 samples

anisotropic consolidation procedure.

A clay conductivity model which takes into account the effect of fabric will now be developed. It will be used later to explain the resistivity changes observed using triaxial loading (Section 2.5) which are felt to be caused by small stress-induced fabric changes.

Fabric can be thought of as a measure of the proportion of number and volume normalized conductivity averages in the clay. Zones where the clay particles have increased parallel alignment behave more like the volume normalized conductivity since the normalization procedure is tantamount to paralleling small pore widths together. Consider a small region of the clay to have its particles aligned at some angle θ to the horizontal. Let the conductivity distribution in the alignment direction be given by the volume normalized distribution, and the orthogonal conductivity be given by the number normalized distribution. A tensor rotation of the form

$$\sigma_{hor} = \frac{\sigma_v + \sigma_n}{2} + \frac{\sigma_v - \sigma_n}{2} \cos 2\theta \qquad \text{2-9a}$$

$$\sigma_{vert} = \frac{\sigma_v + \sigma_n}{2} + \frac{\sigma_v - \sigma_n}{2} \cos 2\theta \qquad \text{2-9b}$$

can be used to obtain the distributions in the horizontal and vertical directions. The actual procedure used was to first cascade σ_v and σ_n one level using the technique discussed in

Appendix C. The resulting distributions were considered the principal direction distributions. Putting all possible combinations of these distributions into Equation 2-9 the horizontal and vertical distributions are generated. These distributions are then cascaded until the geometric mean of the cascaded distributions becomes stable.

The results of these computations for the distributions used before (Figure 2-4) are shown in Figure 2-6 for tap water and 0.1 M KCl pore fluids. The average particle inclination angle for this porosity and fabric is from 22° to 25° (Martin and Ladd, 1970). The model predicts an anisotropy of 1.4-1.6 which is in fair agreement with the values measured. This model will be used later to explain the triaxial test results.

The oriented sample results could not be fitted by a similar model because a pore size distribution for that type of preparation was not available. However, it is possible to say a few things about the oriented sample distribution. In order to get a greater anisotropy it is necessary for the pore size distribution to span a wider range. This makes the number and volume normalized distributions much more different. The oriented sample resistivity is a factor of 1.7-2.3 more resistive than the random sample. This is equal to or larger than the anisotropy of 1.6-1.8 meaning the resistivity in the oriented direction (horizontal) is greater than the random sample resistivity. The two conductor model (Figure 2-5) illustrates the general behavior of the oriented sample

43
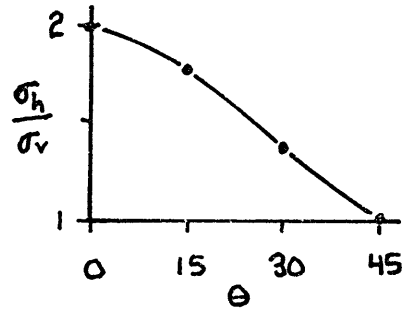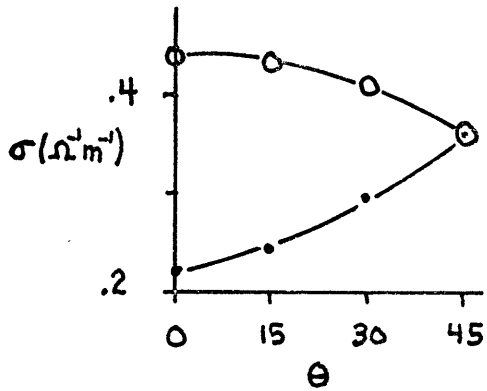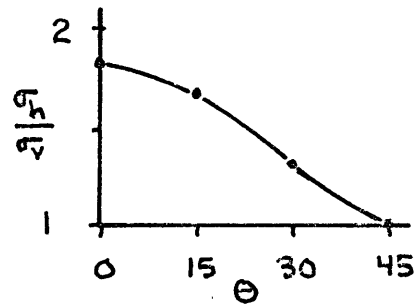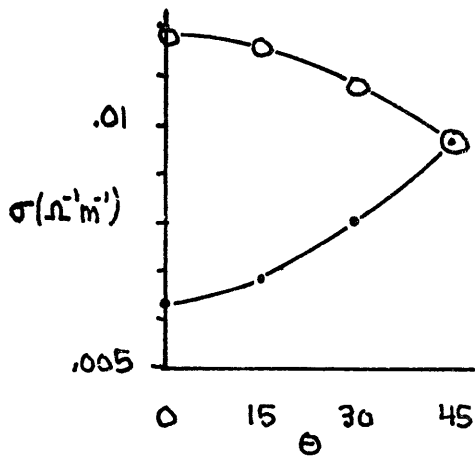
FIGURE 2-6 CONDUCTIVITY AND ANISOTROPY OF
            RANDOM FABRIC KAOLIN AS A FUNCTION
            OF AVERAGE INCLINATION ANGLE, θ
            σ_v (•) σ_h (o)

conductivity distribution necessary to follow the observed σ-n curve. The oriented sample distribution must be wider, and have a greater abundance of small conductors than the random sample distribution at the same porosity.

2.4 Description of Triaxial Experiments

2.4.1 Equipment

.Triaxial compression tests were next run to determine what happens to the resistivity of clay during failure. A standard test cell used for soil mechanics work was modified to permit measurement of the sample impedance during loading (Figure 2-7). The sample is mounted in the chamber and enclosed in a thin rubber jacket. An isotropic confining stress can be applied by means of a hydraulic pressure system. Drainage lines at the top and bottom of the sample allow pore fluid to flow in and out of the sample in response to changes in the applied stresses. Any volume change is measured by means of a burette attached to the drainage line. In addition to isotropic confining stress, a deviator stress can be applied in the vertical direction. The deviator stress is applied by means of a motor drive which pushes or pulls against a load frame. The drive rate is set low enough to allow pore pressures to dissipate in the sample during loading. The magnitude of the vertical force is measured by means of a proving ring, while a dial gauge monitors changes in axial

1 LOAD
2 SAMPLE
3 ELECTRODE & POROUS STONE
4 PLASTIC END CAPS
5 RUBBER JACKET
6 CONFINING PRESSURE
7 DRAINAGE LINE TO BURETTE
8 IMPEDANCE COMPARATOR
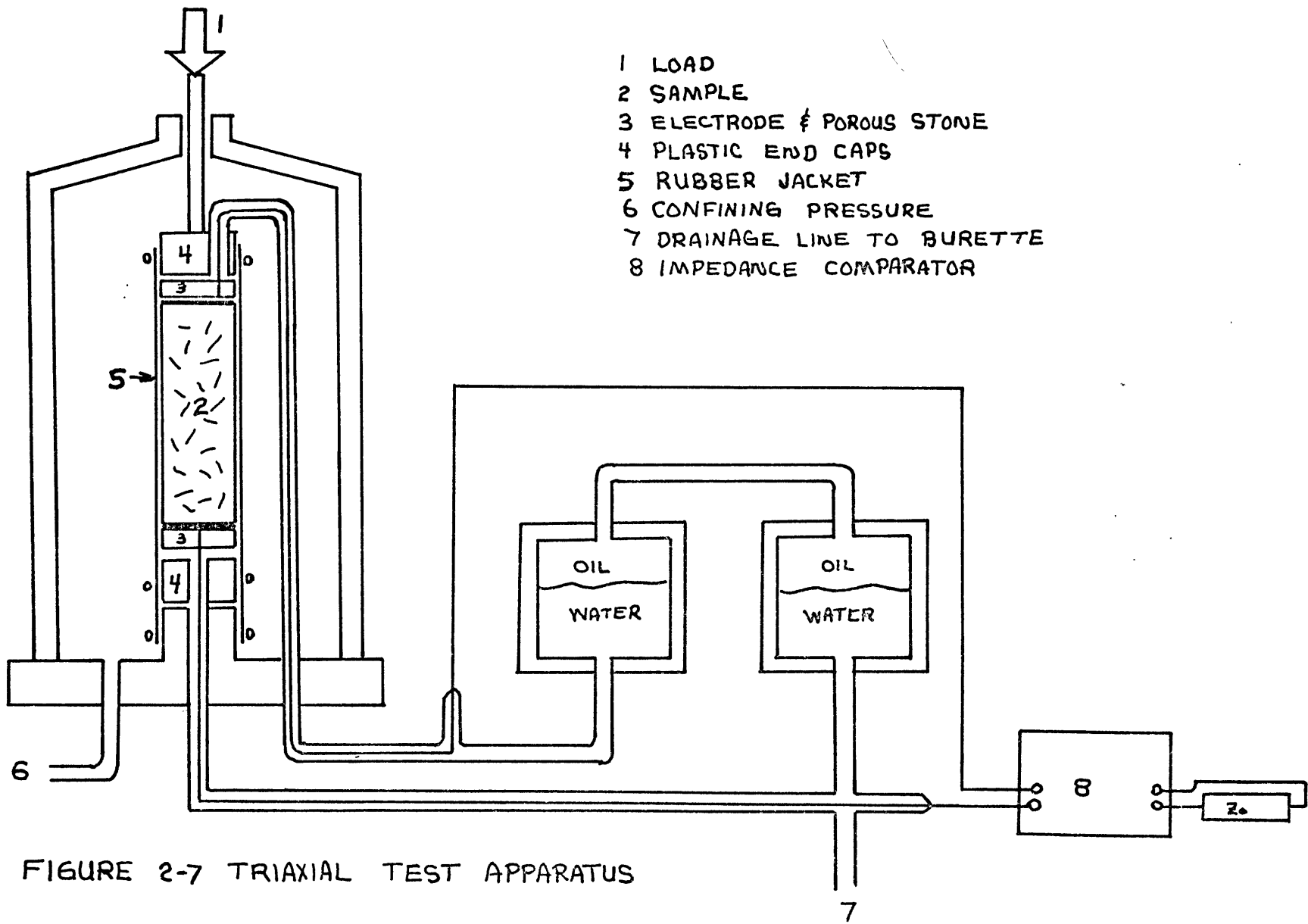
FIGURE 2-7 TRIAXIAL TEST APPARATUS

length of the sample.

Slight modification of the test cell was required for the impedance measuring system. A silver-silver chloride screen electrode was epoxied to the porous stones at each end of the sample. The porous stone rested on a plastic end cap to insulate the sample from the rest of the cell. Silver wire connected the electrodes to the impedance comparator. Since the two drainage lines had to go to the same burette, the impedance measured would be the parallel combination of the sample impedance, and the impedance through the fluid filled tubing where the top and bottom drainage lines connected. To provide electrical isolation while maintaining hydraulic continuity, two reservoirs were inserted in one of the drainage lines. The lower half of the reservoirs contained the pore fluid, while the upper half was silicone oil (Dow-Corning 200 fluid). This arrangement gave a back impedance in excess of 1.5 MΩ which was at least 100 times larger (typically 10^3-10^4) than the sample impedance. Contact impedance of the electrodes was less than 70 Ω which was significantly less than the sample impedance. The same impedance measuring system described in Section 2.2.1 was used. Phase shifts were found to be negligible. The temperature of the cell was monitored by means of a thermistor fastened to the outside of the cell. During experiments, the cell temperature did not vary by more than 1°C.

2.4.2 Sample Preparation

Samples were prepared by packing about 450 g of dry powdered South Carolina kaolin into the oedometer used for the consolidation experiments (RP fabric). Pore fluid was allowed to flow in slowly through the bottom port. After the sample was saturated, fluid was allowed to drain from the cell overnight. The piston was then placed in the cell and loaded to the confining stress at which the triaxial test was to be run. After the sample was well into secondary compression ($\sim$2 days) it was removed from the cell and trimmed to a length of 8.0 cm and a circular cross-sectional area of 10.0 cm^2. For extension tests it was necessary to reduce the length to 5.0 cm. Samples prepared in this method had an initial resistivity anisotropy of about $\rho_v/\rho_h = 1.3$.

Several tests were run on undisturbed samples of Boston Blue Clay (BBC) from Revere, Massachusetts. BBC is a marine illite clay. Its resistivity anisotropy was $\rho_v/\rho_h = 1.3$. This is comparable to its permeability anisotropy of 1.67 (Guertin, 1967).

2.4.3 Types of Tests Run

After the samples were trimmed and placed in the cell, they were isotropically consolidated. During this step water flows out of the sample. In Figure 2-8 is shown a typical consolidation time plot. Primary consolidation is allowed to complete before axial loading is initiated. The sample can
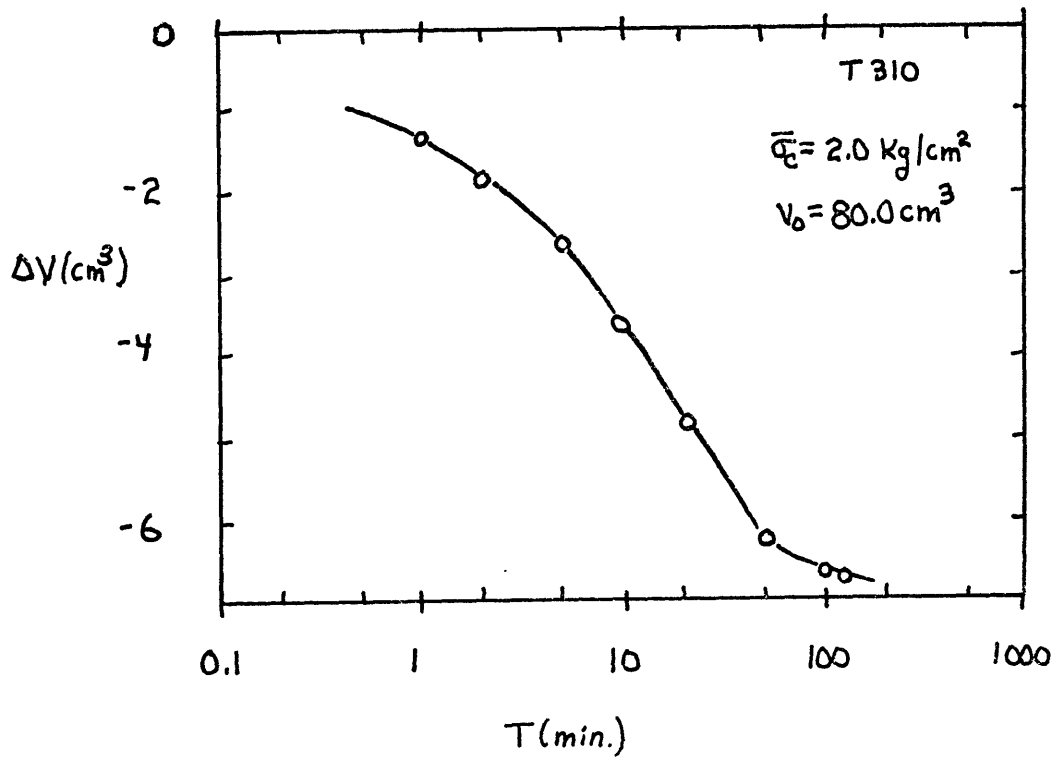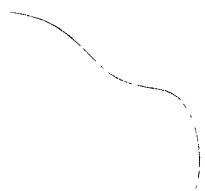
FIGURE 2-8 TYPICAL CONSOLIDATION TIME PLOT

be either normally or over-consolidated before loading. A
normally consolidated sample is one which has never experienced
a confining stress greater than the confining stress used
during failure. An over-consolidated sample has at sometime
in its history been subjected to a confining stress greater
than the one used during failure. The measure of over-
consolidation is the over-consolidation ratio (OCR) which is
the ratio of maximum past consolidation stress to the present
consolidation stress. Highly over-consolidated clays (OCR>5)
dilate and draw water into themselves during failure, while
weakly over-consolidated soils tend to keep rather constant
water content during failure.

After the sample is consolidated the drainage lines can
be left open or closed while the sample is failed. If the
lines are left open the test is called drained (CID), while
closing the lines results in an undrained test (CIU). Failing
the sample by increasing the vertical compressive stress is
called a compression test. This configuration has the
maximum principal stress oriented vertically in the direction
impedance is measured. An extension test results when the
vertical compressive stress is decreased with the maximum
principal stress being perpendicular (horizontally aligned)
to the impedance measuring direction. The pore fluid salinity
was also varied to see what effect it might have.

2.4.4. Resistivity Computation

The measured impedance must be converted to a resistivity. If the sample were of uniform cross-section area A, and length L, the impedance Z is related to the resistivity by

$$\rho = \frac{A}{L} Z = K_g Z \qquad \text{2-10}$$

where K_g is called the geometry factor. If on the other hand, the sample does not have a constant cross-sectional area, the problem becomes a little more complicated. If the slope of the silhouette does not differ greatly from the vertical, the current flow can be approximated to first order to be vertical. Then a differential form of Equation 2-10 can be set up for a thin slice of the sample.

$$d Z(z) = \frac{\rho \, dL}{A(z)} = \frac{\rho \, dz}{A(z)} \qquad \text{2-11}$$

Integrating over the length of the sample gives

$$Z = \rho \int_{-H}^{H} \frac{dz}{A(z)} = \frac{4 \rho}{\pi} \int_{-H}^{H} \frac{dz}{D^2(z)} = \frac{\rho}{K_g} \qquad . \qquad \text{2-12}$$

where D(z) is the sample diameter. The problem comes in determining the silhouette D(z) because the sample is inside a chamber which distorts the observed shape of the sample.

In Appendix A a method of determining D(z) is described. The method is not convenient as the development of negatives and photographs, and the digitization of the silhouette is required.

A simpler way to estimate K_g is to assume the sample deforms as a right cylinder. Knowing the sample volume and length, an average A/L is computed

$$K_g = \frac{A}{L} = \frac{V_o + \Delta V}{(L_o + \Delta L)^2} \qquad\qquad 2\text{-}13$$

where V_o and L_o are the original volume and length respectively, and ΔV and ΔL are their respective changes. The simple correction was found to be as accurate as the optical correction which had an accuracy of better than 3%.

2.5 Triaxial Results

2.5.1 Resistivity and Porosity Changes During Stressing

Results from a typical compression experiment are shown in Figure 2-9. Presented are the volume change, resistivity, and deviator stress as a function of axial strain. As the sample is strained water flows out at an ever-decreasing rate. The resistivity is seen to increase as failure is approached. This behavior is very different from that of rock. There is no large decrease in resistivity before failure, and the actual change during loading is small compared to the changes seen in
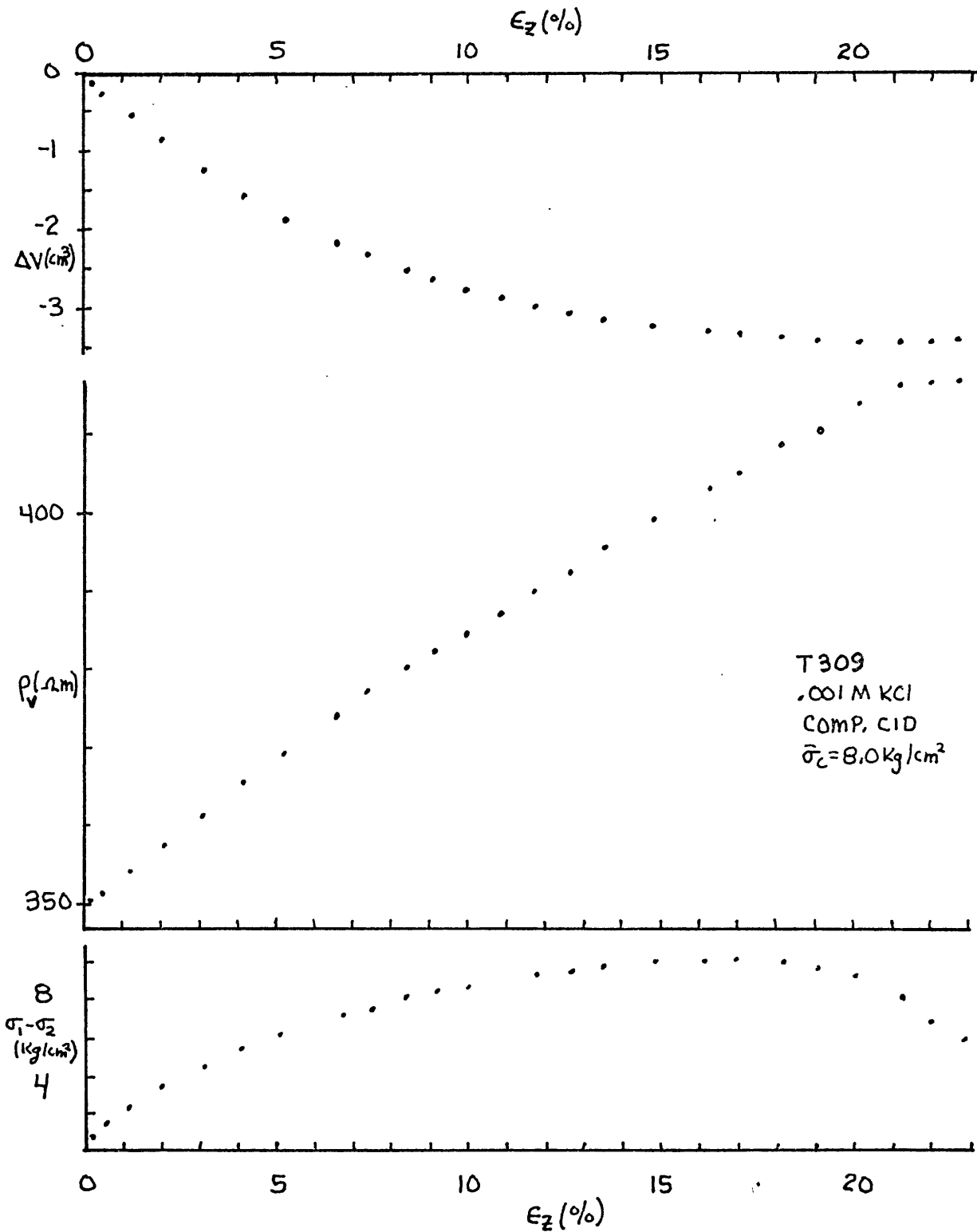
FIGURE 2-9 VOLUME CHANGE, RESISTIVITY AND DEVIATOR STRESS AS A FUNCTION OF AXIAL STRAIN, T309

rock. At first glance one would say there is nothing
extraordinary about this result, because the porosity decreased
so the resistivity increased. Also, since the clay behaved
in a plastic sort of way one would not expect cracks to form
and cause a precursory drop in resistivity.

A quick check on the idea of whether the porosity change
is responsible can be made by plotting resistivity against
porosity on logarithmic coordinates (Figure 2-10). From
the consolidation stage of this experiment it is known what
the resistivity-porosity relationship is. The resistivity
during failure increases at a faster rate as a function of
porosity than during consolidation. A more dramatic example
is given in Figure 2-11 where the resistivity increases even
though the porosity is held constant. In fact, for a highly
overconsolidated sample which drew water in during failure
(porosity increasing), the resistivity was found to increase.
This result, increasing resistivity during failure, was
exhibited by all compression experiments regardless of the
pore fluid salinity, consolidation and drainage conditions.
An undisturbed sample of Boston Blue Clay, which is a marine
illite clay, behaved in a similar manner.

As the consolidation results had pointed out the
importance of directional properties of the clay, it was
decided to try some extension tests as this would orient the
maximum principal stress at right angles to the direction
impedance is measured. Much to the relief of this experimenter,
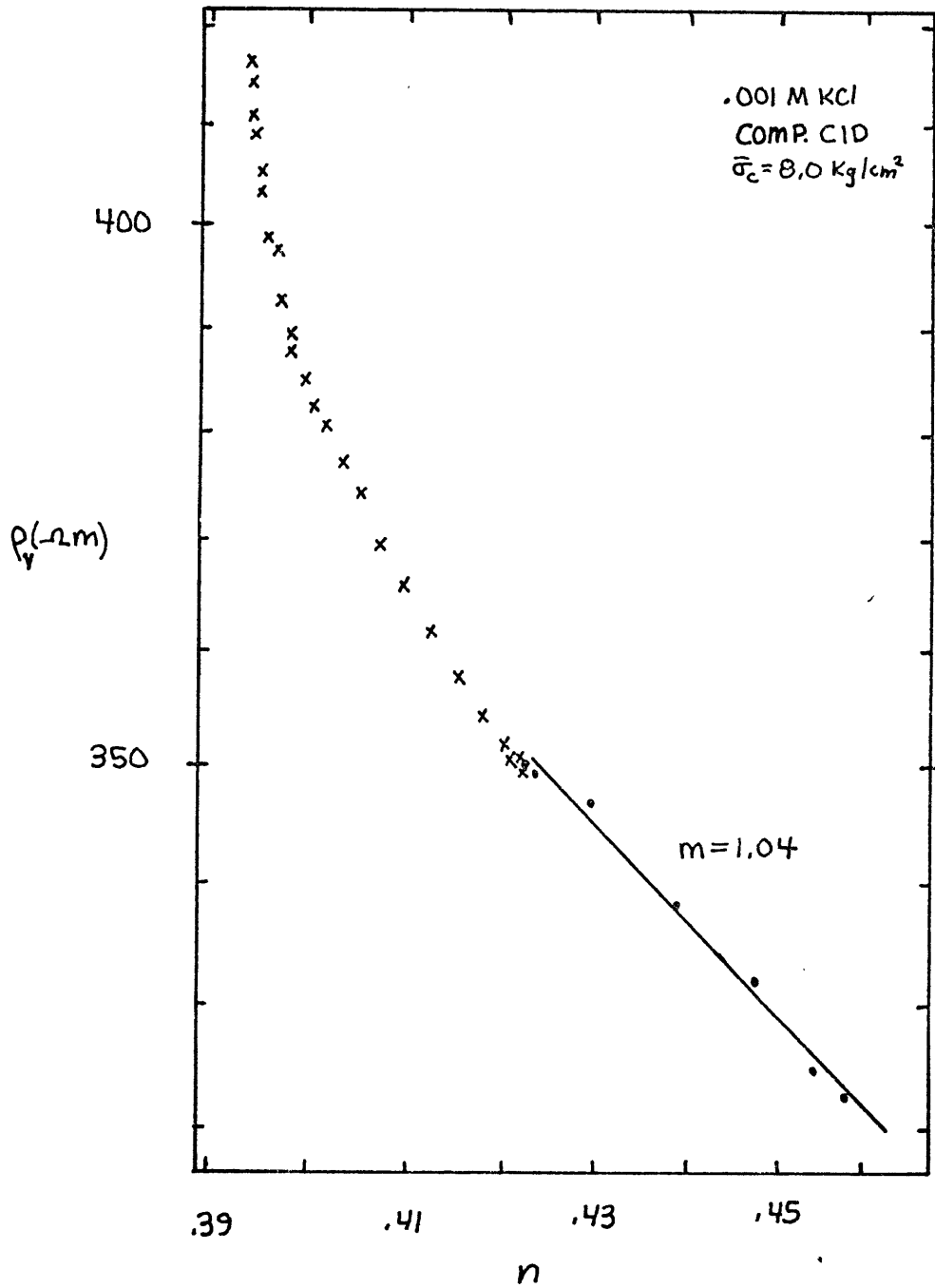
FIGURE 2-10 RESISTIVITY VS. POROSITY, T309
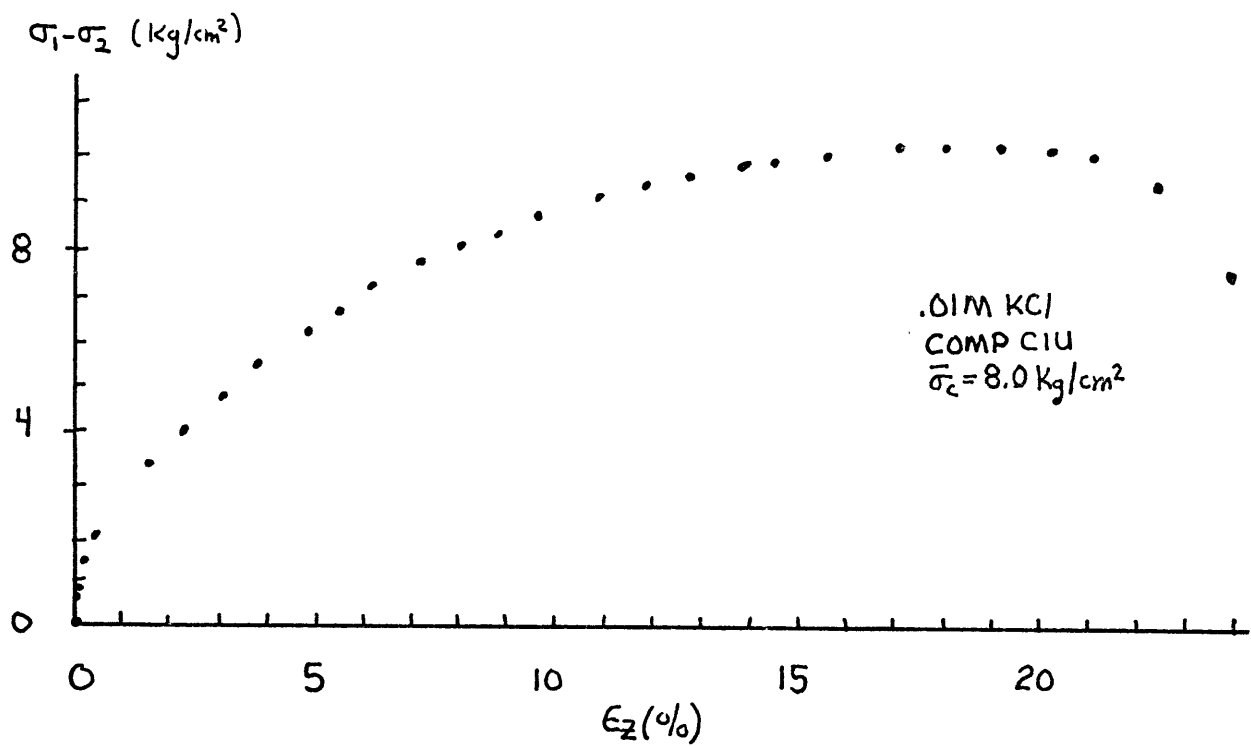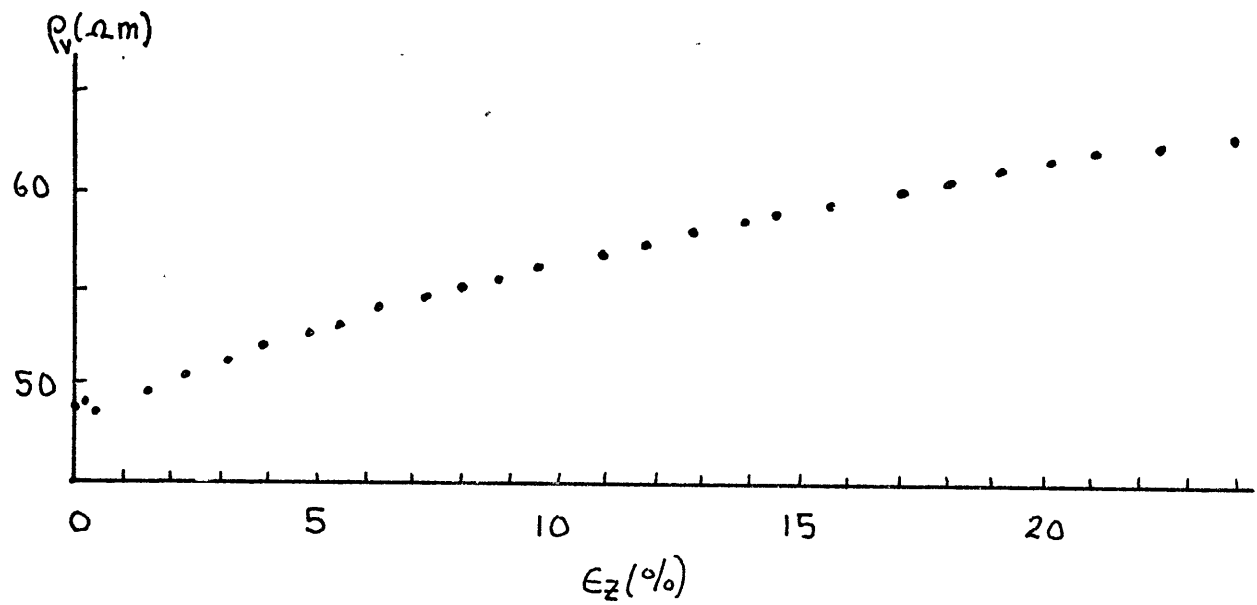
FIGURE 2-11   RESISTIVITY AND DEVIATOR STRESS   VS.
AXIAL STRAIN, T316

there was a reversal in the resistivity change during straining -- it decreased (Figure 2-12). The water content decreased slightly. Plots from other experiments are given in Appendix B.

Table 2-3 presents a summary of all experiments. Of special interest are the relative change in porosity $\frac{\Delta n_f}{n_o}$, the measured relative change in resistivity $\frac{\Delta \rho_f}{\rho_o}$, and the relative change in resistivity predicted using a differential form of Equation 2-1, $\left(\frac{\Delta \rho_f}{\rho_o}\right)_n$. In all cases the predicted value is too small by at least a factor of 1.5. For the highly overconsolidated sample (T302) and the extension tests, the sign of the change is incorrect. The magnitude of the resistivity variation increases with confining stress (Figure 2-13a) and similarly for failure stress (Figure 2-13b). The BBC behaved in a manner similar to the kaolinite, but the magnitude of the variation was less than for kaolinite under the same confining stress.

2.5.2 The Effect of Stressing on Fabric

Fabric changes during stressing are a likely candidate for explaining the triaxial results presented above. It has been suggested by several sources (Lambe and Whitman, 1969; Ladd, 1973) that reorientation mechanisms are responsible for soil deformation during settlement and failure. A simple experiment can illustrate how particle reorientation comes about. Toothpicks, which will represent the clay particles,
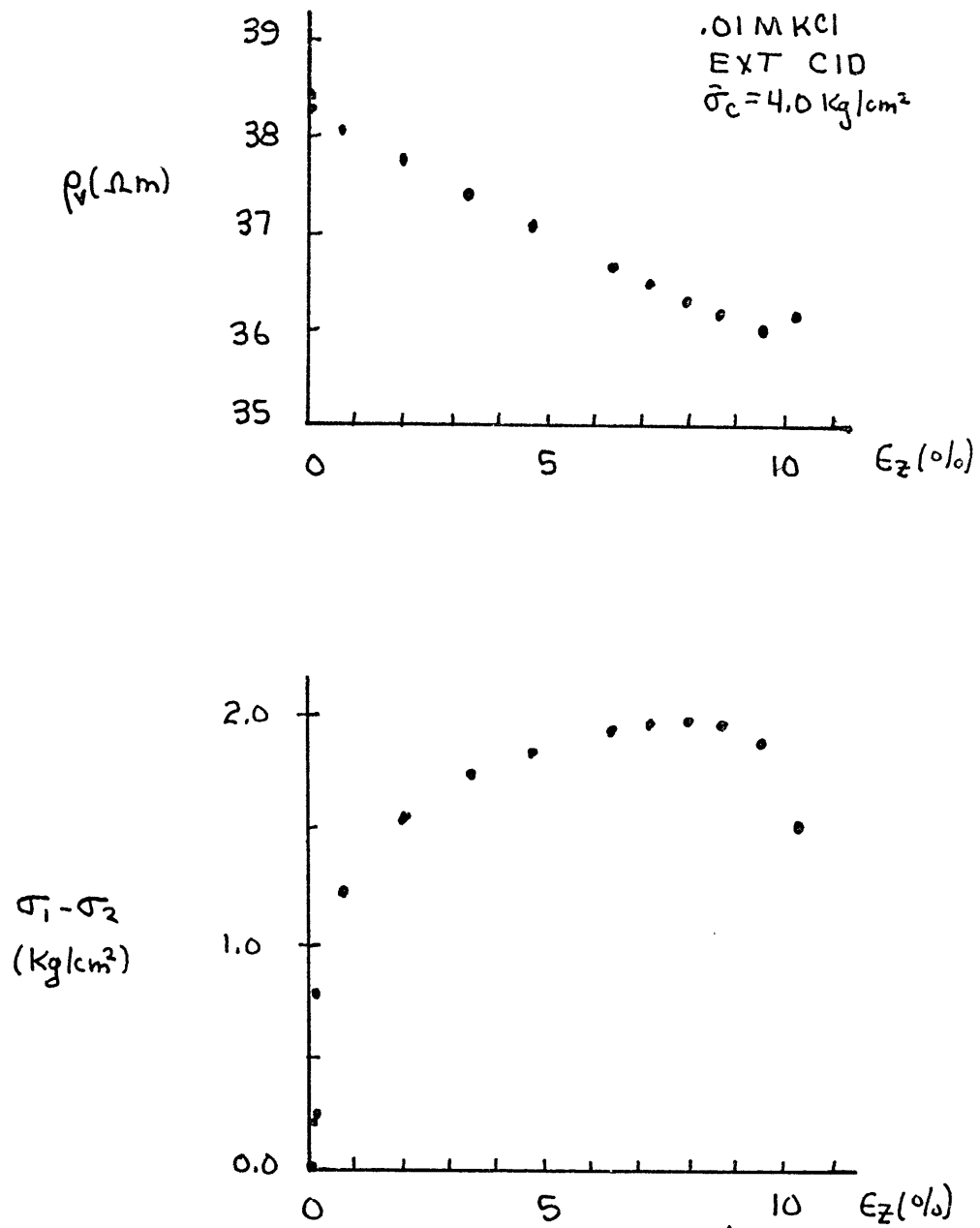
FIGURE 2-12 RESISTIVITY AND DEVIATOR STRESS
VS. AXIAL STRAIN, T321

Table 2-3: Summary of Triaxial Results

TEST	CONDITIONS		(KCl)	$\bar{\sigma}_c$	$(\sigma_1-\sigma_2)_f$	ε_f	n_o	$\dfrac{\Delta n_f}{n_o}$	ρ_o	$\dfrac{\Delta \rho_f}{\rho_o}$	$(\dfrac{\Delta \rho_f}{\rho_o})_n$	m
T302	CID	OCR=8	.001	1.0	2.57	9.5	.451	+.006	267.2	+.0479	-.003	.44
T304	CID	OCR=4	.001	1.0	2.28	10.2	.463	-.002	257.	+.0447	+.002	1.04
T305	CID	OCR=2	.001	2.0	2.69	15.9	.455	-.022	276.6	+.0991	+.022	1.02
T307	CID	COMP	.001	4.0	6.29	18.0	.441	-.059	277.5	+.178	+.059	1.0
T309	CID	COMP	.001	8.0	10.3	17.0	.422	-.064	350.	+.157	+.067	1.04
T310	CID	COMP	.001	2.0	3.29	15.5	.468	-.045	270.	+.128	+.051	1.14
T312	CID	COMP	.01	8.0	12.0	19.1	.445	-.067	45.0	+.242	+.067	1.0
T314	CID	COMP	.01	4.0	6.21	17.0	.452	-.049	45.0	+.151	+.075	1.54
T315	CID	COMP	.01	2.0	2.90	12.0	.455	-.035	44.4	+.0923	+.067	1.90
T316	CIU	COMP	.01	8.0	10.2	19.1	.426	.0	49.0	+.245	.0	1.30
T317	CIU	COMP	.01	4.0	6.00	17.2	.446	.0	41.0	+.205	.0	1.42
T321	CID	EXT	.01	4.0	1.93	8.0	.443	-.004	38.4	-.0547	+.005	1.2*
T322	CID	EXT	.01	8.0	4.11	8.0	.414	-.005	49.1	-.0499	+.006	1.2*
T323	CID	EXT	.01	2.0	1.03	8.6	.448	-.004	32.2	-.0217	+.005	1.2*
T318	CIU	COMP	---	4.0	3.39	9.8	.474	0.	11.87	+.0817	.0	---
T324	CIU	EXT	---	4.0	1.79	1.3	.465	0.	10.68	-.0112	.0	---

NOTE: All tests kaolinite except T318 and T324 (BBC)
   concentration (mole/liter)
   stress (kg/cm^2)
   strain (%)
   resistivity (Ωm)
   *assumed m=1.2

$(\dfrac{\Delta \rho_f}{\rho_o})_n$ based on $\dfrac{d\rho}{\rho}=-m\dfrac{dn}{n}$
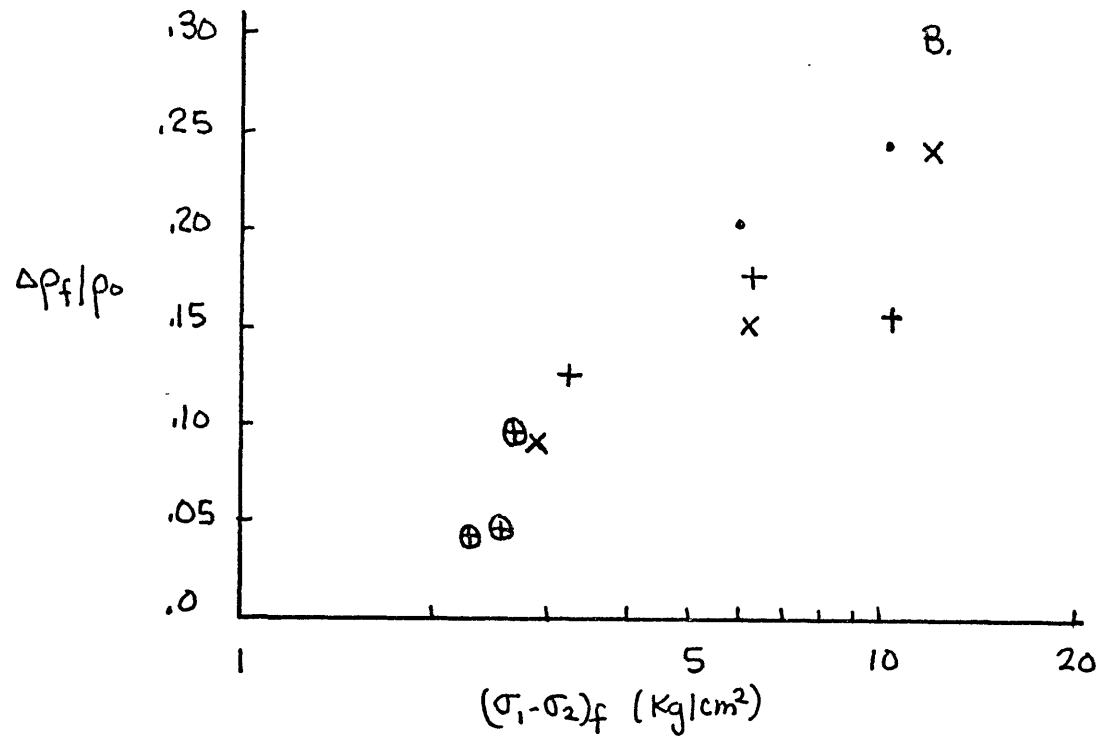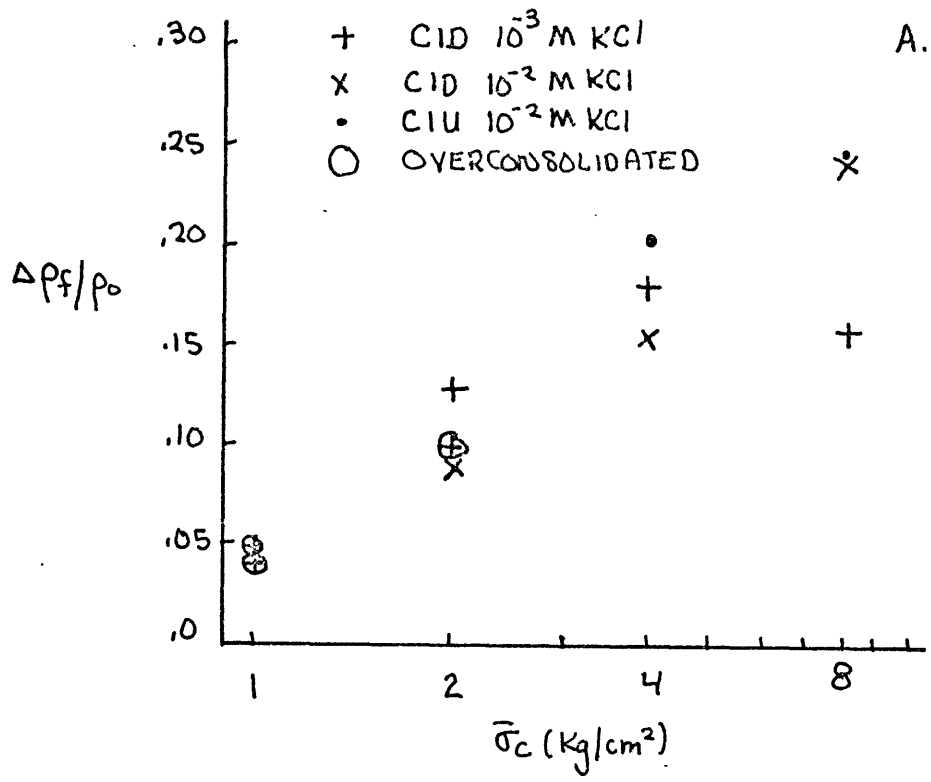
FIGURE 2-13 $\Delta \rho_f / \rho_o$ VS $\bar{\sigma}_c$ AND $(\sigma_1 - \sigma_2)_f$ FOR COMPRESSION TESTS

are dropped onto a table. Two parallel sticks are then used
to push the toothpicks together (Figure 2-14). As the sticks
come closer together, the toothpicks are rotated perpendicular
to the direction of applied force. The model is not ideal as
there are no forces to keep the particles from touching each
other, but it does illustrate the reorientation mechanism.

There is evidence from X-ray diffraction studies that
stress changes can modify clay fabric. Experiments on the
effect of stress on fabric reported by Martin and Ladd (1970)
are rather informative. Oriented and random samples of kaolin
were consolidated and the degree of particle orientation
determined by an X-ray diffraction method (Martin, 1966).
Increased consolidation stress was found to increase particle
orientation. Changes in fabric with increased consolidation
stress tend to be smaller for samples with more aligned fabric.
Samples which are at higher stress levels require a larger
increase of stress to alter their fabric.

Experiments which changed the direction of consolidation
were also reported by Martin and Ladd. In these experiments,
samples were first consolidated to 1 kg/cm^2 and then reloaded
in a perpendicular direction. There was a tendency for the
orientation of the particles to be rotated perpendicular to
their original orientation direction. It does take a great
deal of stress to completely rotate the orientation direction,
but small changes of average particle orientation are possible.

These findings cast some light on the triaxial experiment
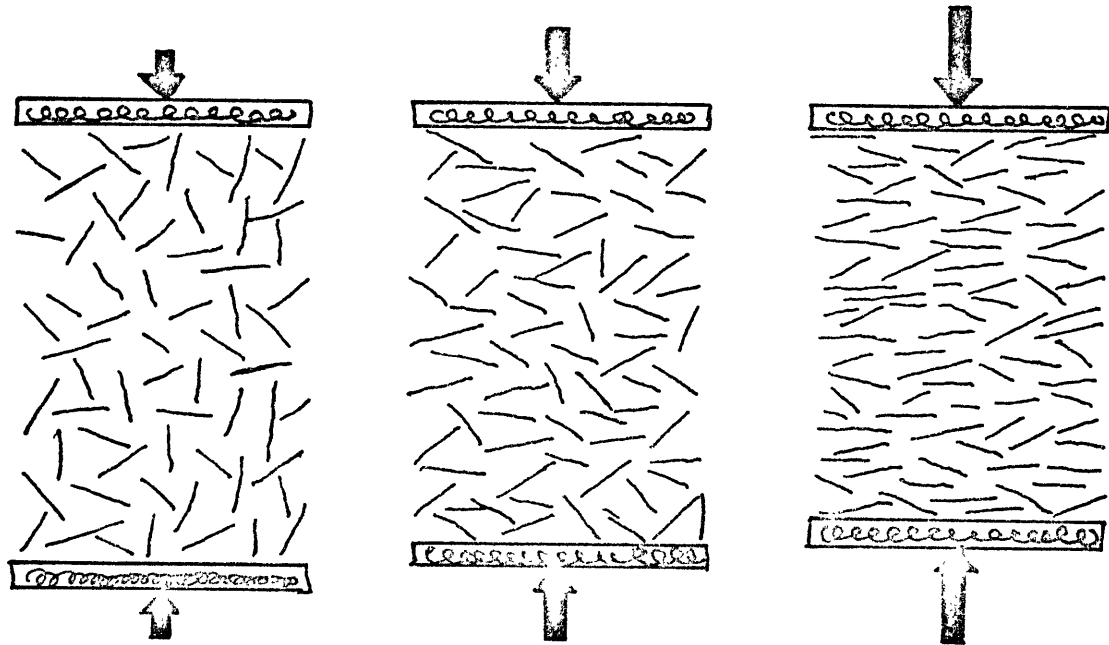
FIGURE 2-14 TOOTHPICK EXPERIMENT

results. First, the increased change of resistivity with
increased deviator stress at failure (Figure 2-13) is
consistent with increased particle orientation with increased
stress. The particles would tend to align perpendicular to
the maximum stress direction (vertical) and cause an increase
of resistivity along the principal stress direction. Secondly,
the smaller change of resistivity observed for the unloading
experiments is consistent with the finding that once the clay
particles become aligned it is much more difficult to disrupt
their alignment. Finally, the small resistivity changes found
in the BBC is probably due to much better particle alignment
in the naturally sedimented clay than in the remolded randomly
oriented samples.

2.5.3 Random Network Model Predictions

Using the random network model presented in Section 2.3.3
it is possible to estimate how much particle reorientation
is necessary to produce the measured resistivity changes, and
to see whether or not this value is realistic. Let us consider
the vertical conductivity of the tap water case in Figure 2-6.
For an average inclination angle of 24° the vertical conduc-
tivity σ_V will change by about 1% per degree change of
inclination angle.

The effect of porosity change must be removed from the
data before estimating the average angle change. This is
done by subtracting $\left(\frac{\Delta\rho_f}{\rho_o}\right)_n$ in Table 2-3 from $\left(\frac{\Delta\rho}{\rho_o}\right)_f$

The result, $\left(\frac{\Delta \rho_f}{\rho_0}\right)_{fabric}$ is plotted against $(\sigma_1 - \sigma_2)_f$ for

kaolinite samples in Figure 2-15. The triangles (Δ) are

from the extension tests, and are actually negative values,

and the circled values ($\odot$) are from undrained tests. If

the two points from the undrained tests are not considered,

the remaining data lie along the line shown. There is

reason to believe the undrained values should be lower.

During an undrained test, pore pressure in the sample and

the drainage lines increases. If the drainage system, which

is made of plastic, expands there is a possibility of fluid

flow out of the sample taking place. This would mean the

porosity actually decreases slightly, and the resistivity

change due to fabric would be smaller.

The data are consistent with the notion of increased

reorientation with increased stress. Using the network model

as well as the data in Figure 2-15 it is estimated that the

average inclination angle changes from 1°-10° for a failure

deviator stress of from 1-10 kg/cm^2. These estimates are

somewhat larger than those of Martin and Ladd (1970), but it

must be remembered the stress system used in their experiments

were not as anisotropic as those used in the triaxial tests.

The model used to predict the angular changes has made some

assumptions about what the conductivity distributions are in

the principal conductivity directions. It is possible that

the principal conductivities are more aniostropic than those
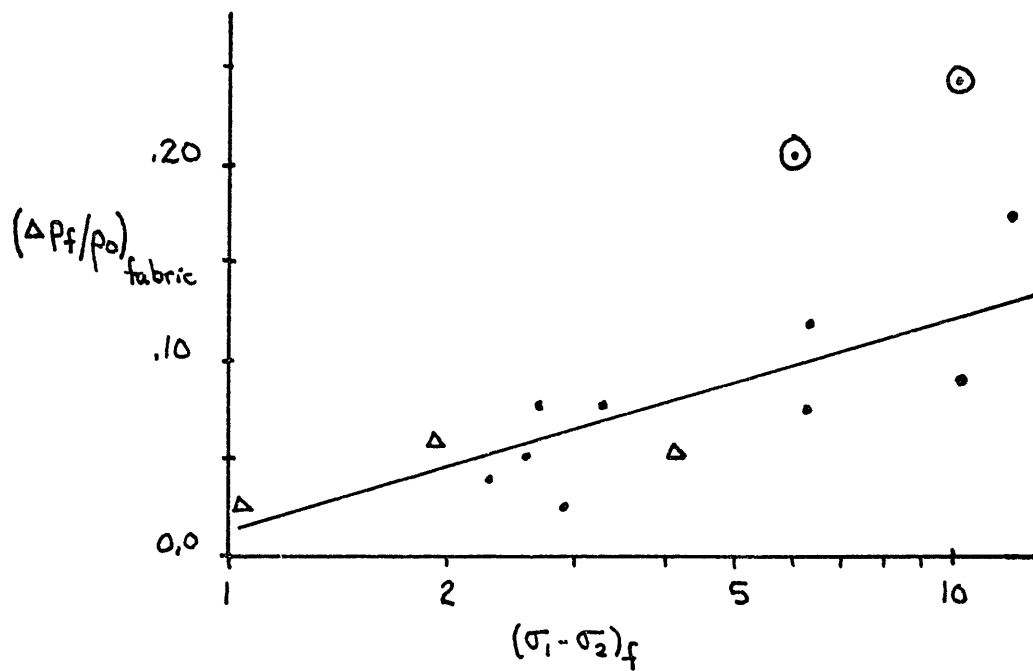
FIGURE 2-15   RELATIVE RESISTIVITY CHANGE AT
FAILURE DUE TO FABRIC VS. DEVIATOR
STRESS AT FAILURE FOR KAOLIN

CIRCLED VALUES (⊙) ARE FROM
UNDRAINED TESTS, TRIANGLES ARE
NEGATIVE VALUES FROM EXTENSION
TESTS

used here making the cascaded conductivity more sensitive to
angular variations and thus requiring smaller angular rotations
of the particles.

2.6 Discussion

The resistivity of clay has been found to depend on the
inverse square of porosity in a manner similar to that of
rocks. Departures from this behavior occur when surface
conduction becomes important. Increased importance of surface
conduction, which occurs at lower porosities and higher pore
fluid resistivity, causes the clay resistivity to drop below
the square law value. Fabric will cause departures in clay
resistivity above the square law prediction. Increased
particle orientation will raise the resistivity in the directions
parallel and perpendicular to the orientation directions while
at the same time increasing the resistivity anisotropy. Using
a measured pore size distribution, a pseudo-random network
model was developed which predicts the measured clay resis-
tivity quite well for samples with random fabric.

Changes in clay resistivity due to changes of stress are
quite different from those observed in rocks. First, there
are no dramatic changes of clay resistivity as confining
stress is increased as is observed in rock (Brace et al.,
1965). Secondly, resistivity changes during triaxial failure
are rather small compared to those of rock. These differences

are explained in terms of the behavior of the pore spaces
in response to the stress system. The voids in rock can
open and close in response to an applied stress, but can not
reorient themselves. Rock cracks have fixed spatial locations.
Clay particles, on the other hand, are not rigidly held in
place, but rather are free to move in response to applied
stresses and thus change the orientation of the pore spaces.
Because of these differences, rocks fail in a dramatic fashion
with large precursory changes of resistivity (Brace and Orange,
1968a). Clay, on the other hand, fails in a plastic manner
without very large changes of resistivity.

Figure 2-16 shows a conceptualization of what is happening
to the clay particles during triaxial loading. Originally the
particles have a slight horizontal alignment. Loading makes
the particles rotate perpendicular to the direction of maximum
stress. For the extension case this increases the average
inclination angle of the particles and decreases the vertical
resistivity. When the stress system is rotated 90° (compression
test), the average inclination angle decreases and ρ_V increases.

Using the pseudo-random network model developed to explain
the resistivity of consolidated kaolin, the amount of particle
reorientation associated with failure of clay was estimated.
Average particle inclination angles are estimated to change
by 1°-10° depending upon the strength of the clay. These
estimates are higher than those estimated for one-dimensional
consolidation at similar stress levels.
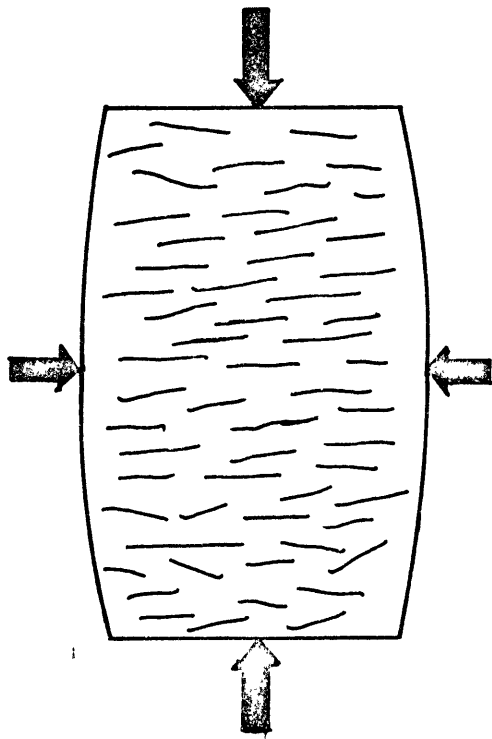
COMPRESSION AND INCREASED   ORIGINAL SAMPLE WITH   EXTENSION AND INCREASED
HORIZONTAL ORIENTATION   HORIZONTAL ORIENTATION   VERTICAL ORIENTATION
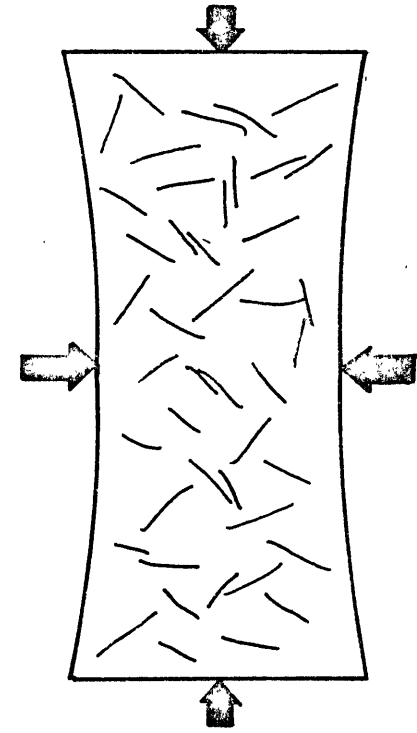
FIGURE 2-16   MODEL OF PARTICLE REORIENTATION DURING COMPRESSIONAL AND

EXTENSIONAL FAILURE

In view of the resistivity anisotropy of clay it was of interest to determine if the clay stiffness was also anisotropic. Assuming the clay sample to be azimuthally symmetric, the strain-stress relationship is given by

$$
\begin{bmatrix}
\epsilon_{xx} \\
\epsilon_{yy} \\
\epsilon_{zz} \\
\epsilon_{yz} \\
\epsilon_{zx} \\
\epsilon_{xy}
\end{bmatrix}
=
\begin{bmatrix}
S_{11} & S_{12} & S_{13} & & & \\
S_{12} & S_{11} & S_{13} & & \bigcirc & \\
S_{13} & S_{13} & S_{33} & & & \\
& & & S_{44} & & \\
& \bigcirc & & & S_{44} & \\
& & & & & 2(S_{11}-S_{12})
\end{bmatrix}
\begin{bmatrix}
\sigma_{xx} \\
\sigma_{yy} \\
\sigma_{zz} \\
\sigma_{yz} \\
\sigma_{zx} \\
\sigma_{xy}
\end{bmatrix}
\qquad 2\text{-}14
$$

for transversely isotropic material. In the laboratory system $\sigma_{xx} = \sigma_{yy} = P$, the confining pressure, and $\epsilon_{xx} + \epsilon_{yy} = \epsilon_{nn}$.

$$
\begin{bmatrix}
\epsilon_{nn} \\
\epsilon_{zz}
\end{bmatrix}
=
\begin{bmatrix}
2(S_{11}+S_{12}) & 2S_{13} \\
2S_{13} & S_{33}
\end{bmatrix}
\begin{bmatrix}
P \\
\sigma_{zz}
\end{bmatrix}
\qquad 2\text{-}15
$$

The total stresses and strains in Equation 2-15 can be replaced by differential quantities. Two stress systems are used: first a differential isotropic increase of stress, and then a differential increase of the vertical stress alone.

The compliances are given by rewriting Equation 2-15

$$
\begin{bmatrix} d\epsilon_{nn} \\ d\epsilon_{zz} \end{bmatrix} = \begin{bmatrix} 2dP & 2d\sigma_{zz} & 0 \\ 0 & 2dP & d\sigma_{zz} \end{bmatrix} \begin{bmatrix} S_{11}+S_{12} \\ S_{13} \\ S_{33} \end{bmatrix} \qquad 2\text{-}16
$$

where the differential quantities in the 3x2 matrix are column vectors with values from the two differential loadings. These two loading systems are alternated until the sample fails. The data is used in a least squares estimation to obtain the compliances.

$$
\begin{bmatrix} S_{11}+S_{12} \\ S_{13} \\ S_{33} \end{bmatrix} = \begin{bmatrix} 4dP^T dP & 4dP^T d\sigma_{zz} & 0 \\ 4d\sigma_{zz} dP & 4(d\sigma_{zz}^T d\sigma_{zz}+dP^T dP) & 2dP^T d\sigma_{zz} \\ 0 & 2d\sigma_{zz}^T dP & d\sigma_{zz}^T d\sigma_{zz} \end{bmatrix} \begin{bmatrix} 2dP^T d\epsilon_{nn} \\ 2(d\sigma_{zz}^T d\epsilon_{nn}+dP^T d\epsilon_{zz}) \\ d\sigma_{zz}^T d\epsilon_{zz} \end{bmatrix} \qquad 2\text{-}17
$$

The stiffnesses (inverse tensor of the compliances) obtained for a normally and over-consolidated kaolinite sample are given in Table 2-4 as a function of effective confining stress ($\overline{\sigma}_c$) and shear failure index (SFI) which is the ratio of the maximum shear stress in the material to the shear stress at failure. Failure occurs at SFI = 1.0. The stiffnesses of the normally consolidated sample increased with increasing SFI. This is misleading because $\overline{\sigma}_c$ is also increasing which drives out water and strengthens the sample.

Table 2-4

Kaolinite Stiffness Coefficients

Normally Consolidated

$\overline{\sigma}_c$	SFI	$C_{11}+C_{12}$	C_{13}	C_{33}	$\dfrac{C_{11}+C_{12}}{C_{33}+C_{13}}$
4.0	0.0	252.	74.4	195.	.938
5.0	.38	371.	97.3	177.	1.35
6.0	.82	352.	187.	267.	1.22

Over-Consolidated

$\overline{\sigma}_c$	OCR	SFI	$C_{11}+C_{12}$	C_{13}	C_{33}	$\dfrac{C_{11}+C_{12}}{C_{33}+C_{13}}$
.75	10.7	0	178.	61.8	192.	.699
1.0	8.0	.86	660.	275.	308.	1.13
1.25	6.4	1.0	505.	208.	248.	1.11

Note: All stresses and stiffnesses in kg/cm^2.

The sample is mildly anisotropic as seen by some of the values of $(C_{11}+C_{12})/(C_{33}+C_{13})$ which differ slightly from unity. The overconsolidated sample shows an increase in stiffness with increasing $\bar{\sigma}_c$ until SFI = 1.0 at which point the stiffness decreases. The only indication of anisotropy comes at the first load increment where $(C_{11}+C_{12})/(C_{33}+C_{13}) = 0.7$. This is probably due to the high degree of overconsolidation. Straining between the first and second differential loading removed this anisotropy. The mechanical anisotropy appears to be less than or equal to the resistivity anisotropy.

2.7 Summary

The most important result of this chapter is that the resistivity of clay does not behave like rock during failure. Changes in the resistivity of clay result primarily from modifications of fabric. The clay particles, because they are not bonded tightly to each other, are free to move in response to the applied stress. The particles try to align themselves so that they are perpendicular the direction of maximum stress. The result is a small O(5%-25%) resistivity increase for compression tests and resistivity decrease for extension tests measured in the direction of maximum and minimum principal stress respectively. The model predicts an increase in ρ_v/ρ_h for compression, while ρ_v/ρ_h is expected to decrease for extension tests. Simultaneous measurement of

resistivity in perpendicular directions are needed to test this hypothesis.

If the resistivity anisotropy is changed prior to failure, it might present a way of monitoring the stability of slopes. However, the anisotropy change might be so small that it is hard to separate from changes caused by meteorologic and other influences.

Archie's law (square law) was found to give reasonable estimates of clay resistivity provided the importance of surface conductivity is small and the clay fabric is rather random. Knowing the pore size distribution of the clay, it is possible to estimate the clay conductivity quite well using pseudo-random networks. The geometric mean of the conductivity distribution gives a very good approximation to the pseudo-random network value.

CHAPTER 3:   SMALL-SCALE RESISTIVITY MEASUREMENTS ALONG

THE SAN ANDREAS FAULT

3.1 Introduction

A small-scale resistivity monitor was installed direct-
ly adjacent to the San Andreas fault at Melendy Ranch, Cali-
fornia in March 1972. The site was chosen because of the
large amount of fault creep activity, and a creepmeter at the
site allowed monitoring of tectonic motion. Due to the small
scale of the measurements the monitor was well suited for
studying fault creep as well as resistivity variations in
the near surface environment which might influence large-
scale measurements.

Melendy Ranch is situated 40 km southeast of Hollister,
California in Bear Valley. The San Andreas fault runs through
the valley with a northwesterly strike. The geology of the
area is primarily tertiary sediments with some volcanic in-
trusions to the southwest (Wilson, 1943). Quaternary ter-
races and alluvium are scattered throughout the valley floor.

Nason (1971) has reported evidence of fault creep during
the last 27 years. Early evidence is in the form of dis-
placement of man-made structures. Displacement of a corral
fence at Melendy Ranch was about 53 cm over a 21 year period.
This corresponds to a slippage rate of 2.5 cm/year. At a
point 2.5 km southeast of the corral the slippage inferred
from fence deformation is 0.9 cm/year. At this point the

San Andreas appears to have more than one active trace, and the total creep rate could be larger (Brown, 1970).

In June of 1969 a creepmeter was installed at Melendy Ranch by the U.S. Geological Survey. The instrument consists of a 10 m wire stretched between two piers on either side of the fault. The wire is housed in a pipe, covered by not more than a meter of soil. On one of the piers the wire rides over a pulley and is attached to a weight. A displacement transducer is used to measure changes in the position of the weight, which represents offsets between the two sides of the fault. Sensitivities of fractions of a millimeter are possible. Because of the proximity of the creepmeter and the resistivity monitor, correlations between observations of the two instruments seemed like a reasonable thing to look for.

3.2   Resistivity Survey of the Site

To determine whether any peculiar conditions existed at the site, and to get a feeling for the electrical environment, rather extensive resistivity surveys were made. Three dipole-dipole sections were made, as well as three Schlumberger expansion type arrays (Figure 3-1). The dipole-dipole data are plotted at the intersection of 45° sloping lines emanating from the center of the dipoles. Sections A and B, which are oriented perpendicular to the fault, are shown in Figure 3-2. The resistivity is very low (5-20 Ωm) due to the extensive
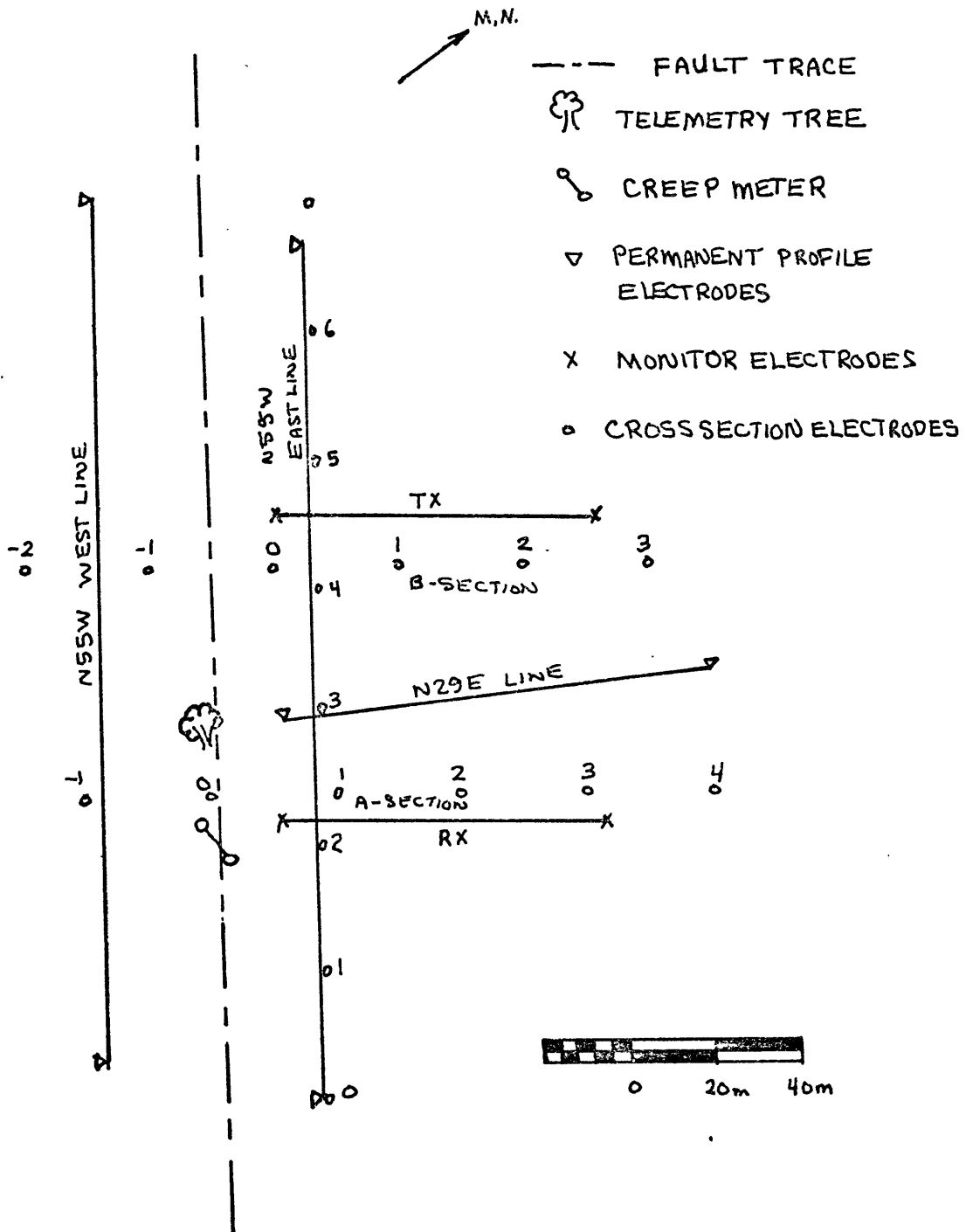
FIGURE 3-1 MAP OF MELENDY RANCH SITE

-5 -4 -3 -2 -1 0 1 2 3 4 5 6

DIPOLE SPACING

1.3   16.1   16.4   5.8   — 60m

11.3   9.25   5.4   9.3   — 90m

10.5   3.4   7.9   10.8   — 120m

SECTION B

-5 -4 -3 -2 -1 0 1 2 3 4 5 6

DIPOLE SPACING

36   15.8   15.2   9.3   26.8   12.1   — 60m

20.6   18.9   6.5   10.8   17.0   12.1   5.7   — 90m

10.6   6.5   6.5   24   7.1   4.5   10.2   — 120m

SECTION A
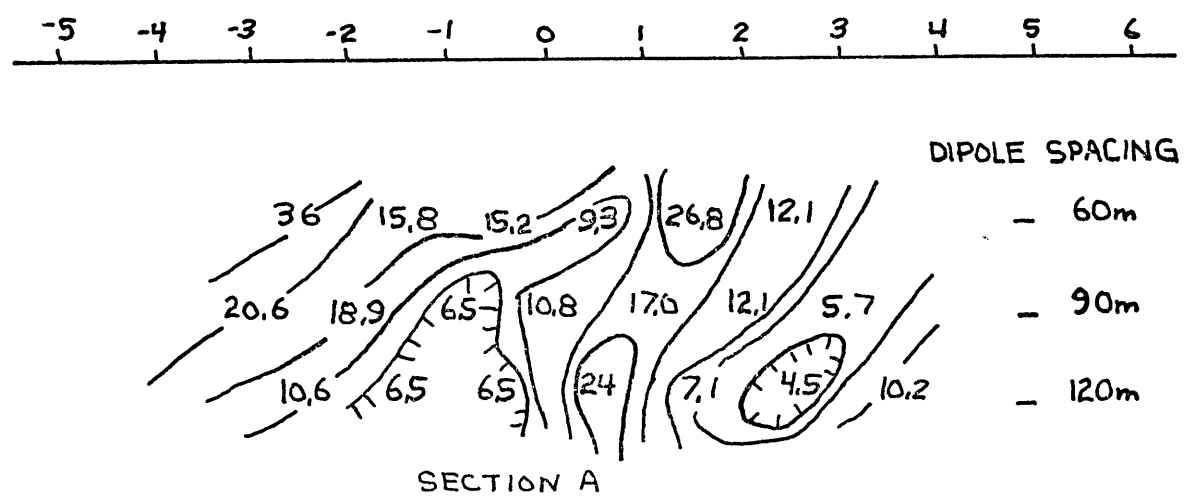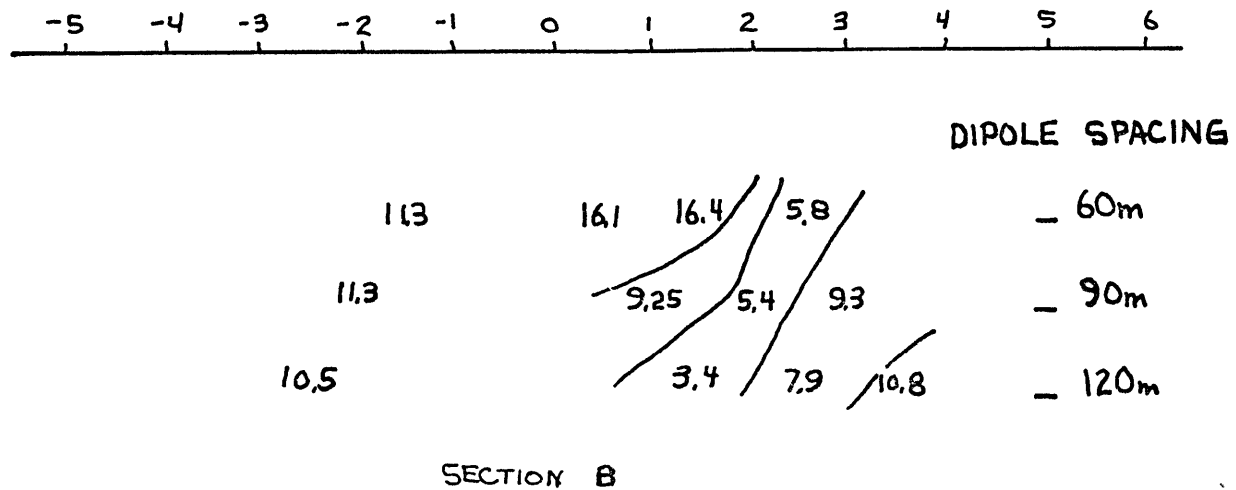
FIGURE 3-2   MELENDY RANCH RESISTIVITY CROSS-SECTION PERPENDICULAR FAULT
DIPOLE LENGTH = 30 m   VALUES IN Ω-m

clay deposit in the area. A section along the fault (Figure 3-3) shows similar values (5-25 Ωm). There is a slight decrease in resistivity with depth, but nothing really significant.

The three Schlumberger expansion soundings are shown in Figure 3-4. The data are characterized by a resistive upper layer whose resistivity varied from 300-1800 Ωm. This layer is about .15 m thick and represents a dried crust. The resistivity of the second layer is in the range of 5-10 Ωm. As mentioned above these are rather low resistivities, and are associated with clay. Measurements made at the Almaden Cienega Winery 26 km to the north, and measurements halfway between Melendy Ranch and Tres Pinos (Figures 3-5 and 3-6) show similar values. These values are probably representative of alluvial covered areas in this region. Borings to depths as great as 28 m revealed primarily clay running from a dark black color at the surface to brown and finally blue at depth. Rock chips, sand and silt were present at all depths with no distinctive transitions suggesting the site is an old scour which has been filled with river deposits. There is evidence that the clay is underlain by a fine-grained, cross-bedded, green sandstone which is quite friable. Laboratory measurements found its resistivity to be 4.5 Ωm which is probably due to clay content and saline pore fluid.

| | -1 | | | | 0 | | | | 1 | | | | 2 | | | 3 |

0　1　2　3　4　5　6　7　8　9　10　11　12

DIPOLE SPACING

4.7　7.5　18.5　15.1　25.4　18.6　17.2　　— 60m

6.2　13.9　13.8　13.6　10.0　8.2　　— 90m

9.8　10.7　11.9　5.1　7.1　　— 120m

6.3　　　　　6.7　　　— 200m

7.0　　　　　9.1　— 300m
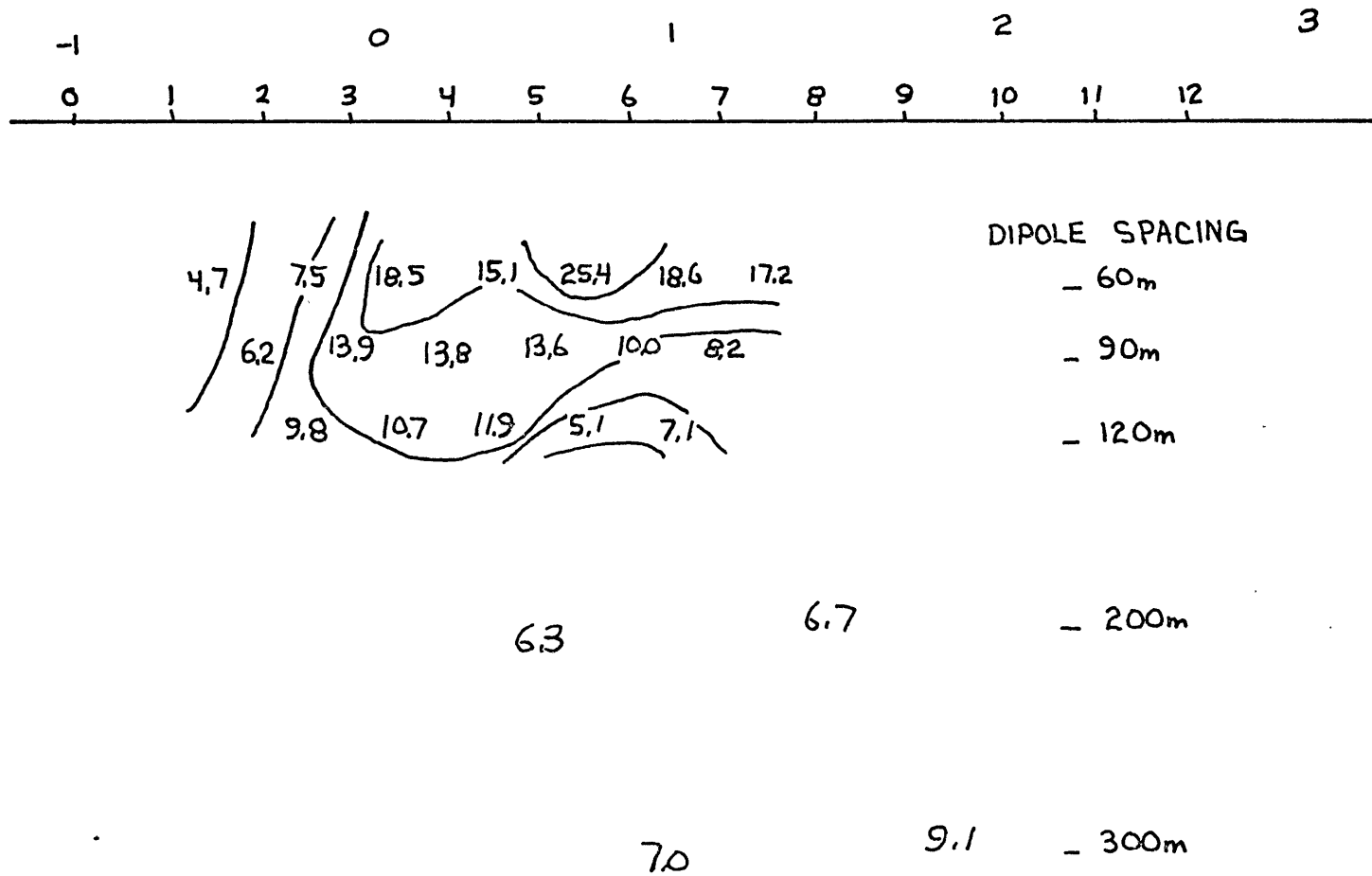
FIGURE 3-3　MELENDY RANCH RESISTIVITY CROSS-SECTION PARALLEL FAULT

DIPOLE LENGTH = 30m & 100m　　　VALUES Ω-m
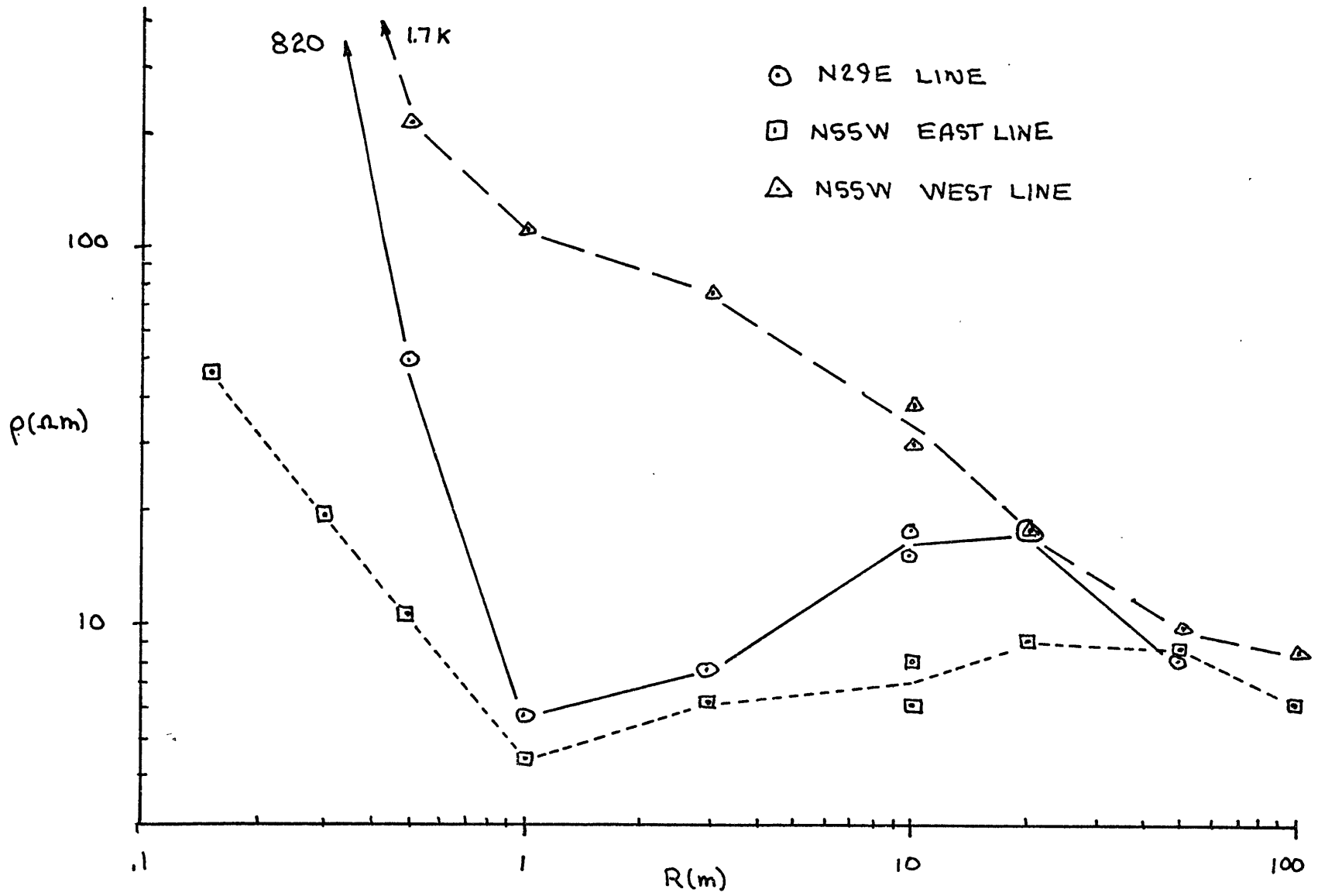
FIGURE 3-4 MELENDY RANCH SCHLUMBERGER PROFILES

820   1.7K

⊙ N29E LINE

⊡ N55W EAST LINE

△ N55W WEST LINE

ρ(Ωm)

100

10

R(m)

.1   1   10   100
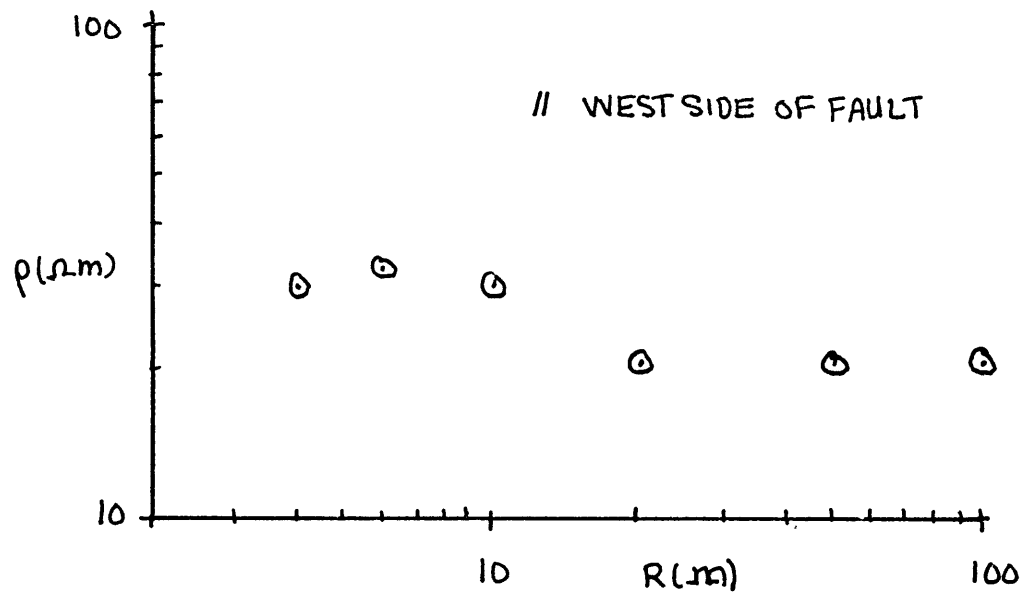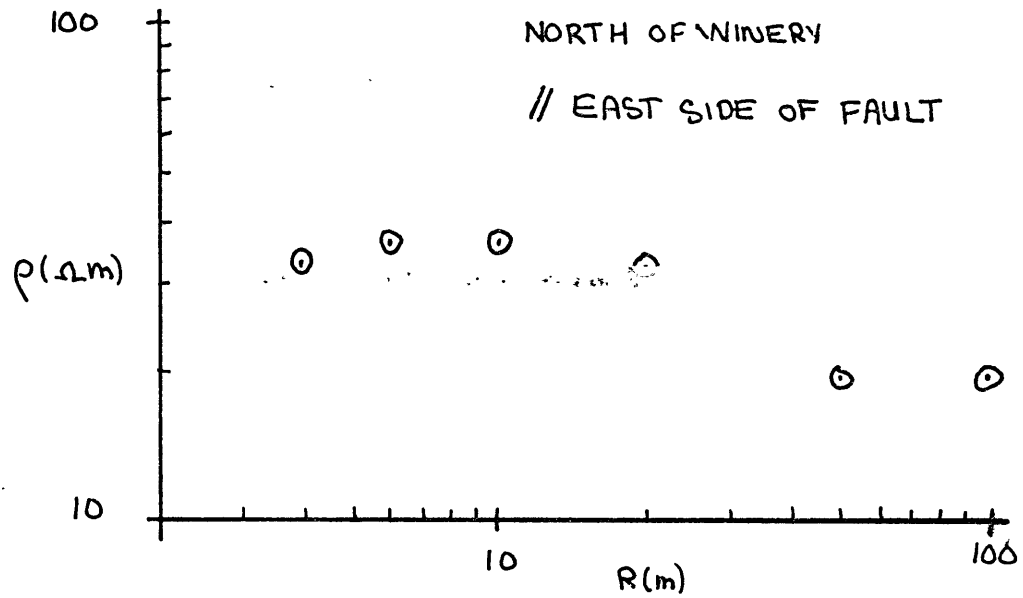
FIGURE 3-5   ALMADEN CIENEGA WINERY PROFILES

DIPOLE SPACING

24   13   _200m

18   15   _300m

        15   _400m

FIGURE 3-6 VALLEY FLOOR MEASUREMENTS BETWEEN TRES PINOS AND

MELENDY RANCH   DIPOLE LENGTH =100m   ALL VALUES Ω-m

3.3 The Resistivity Monitor

The resistivity monitor consists of a transmitter and
receiver unit capable of running unattended for a month at a
time. The transmitter produces a 1 hz square wave of con-
stant current as large as 1 ampere. Current regulation is
provided by means of a feedback system, and is stable to at
least 0.01%. The receiver is essentially a highly stable
tuned voltmeter. The receiver electrodes are fed into a pre-
amp external to the receiver which is followed by an ampli-
fier and 1 hz bandpass filter. The signal is then rectified
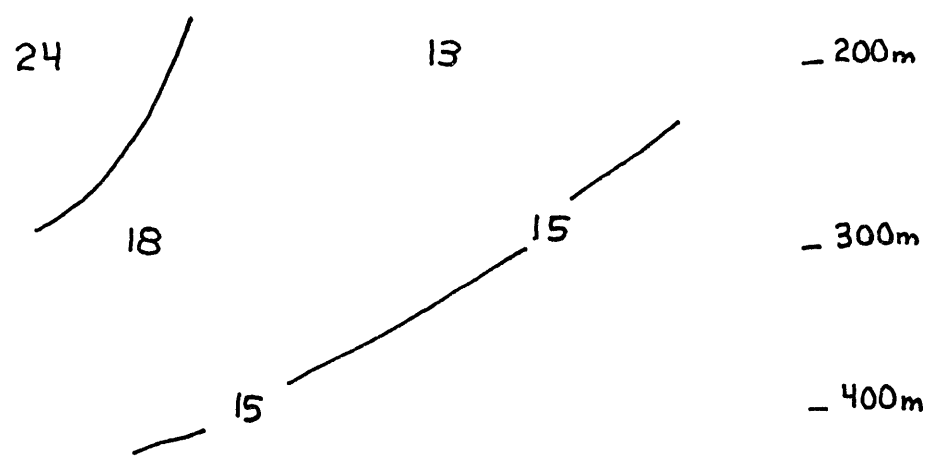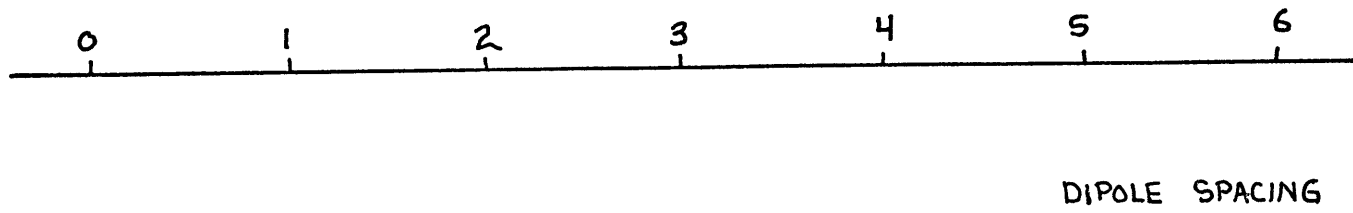and averaged, and a highly stable voltage is subtracted from
the signal. This difference signal is amplified and recorded.
It is also high-pass filtered and amplified to provide a sen-
sitive detector of short term resistivity variations. The
usable gain is limited only by the noise level. Typical
recordings were made using a sensitivity of 0.1%. Later im-
provements allowed increasing the sensitivity to 0.002%.

One of the major technical problems was the elimination
of temperature dependence from the system. At first the sys-
tem was placed in a foam-line plywood box without any sort of
temperature control. Apparent diurnal variations of 0.4%-
0.7% were observed; however, a sensitivity analysis showed
that diurnal temperatures could produce at most a 0.004% re-
sistivity change by varying the temperature of the ground.
The variations had to be due to temperature effects in the
equipment. Subsequent addition of temperature compensation

and a temperature controlling system eliminated the apparent diurnal variations.

The original electrode configuration was two 75 m parallel dipoles oriented perpendicular to the fault (Figure 3-1). This configuration was later changed to a Schlumberger array situated along the strike of the fault with a 200 m transmitting dipole and a 60 m receiver dipole. Eventually a second receiver was built which used electrodes 23 m and 28 m below the first receiver electrodes.

3.4 Diurnal and Long-Term Resistivity Variations

When the resistometer was first installed, apparent diurnal resistivity variations of 0.4%-1.0% were observed. These variations were correlated with the day-night cycle. Installation of a temperature recorder revealed the changes were very well correlated with equipment temperature. Several different temperature controlling and compensating devices were tried. When atmospheric temperature variations are not severe, and the controller is able to keep the box temperature to within 1°C of the operating temperature (40°C), the resistivity is constant at the 0.02% level. On days when the temperature is really well controlled the resistivity varies by less than 0.005%. It is fair to say that diurnal variation of the ground resistivity was not observable at the scale of

these measurements.

The question of long term resistivity variations is important for two reasons. First it limits the maximum gain which can be used with an unattended instrument. Since the monitor has no automatic gain ranging device, large variations could send the recordings off scale between monthly servicings. Second, stability of the near surface layer is an important factor in larger scale measurements. If the upper 100 m of ground had really large seasonal variations it would be difficult to monitor resistivity changes of deeper areas. Sensitivity to surface variations will be considered more fully in Section 3.5. Data from various segments of the period March 1972 to December 1973 of resistivity variation are shown in Figures 3-7 through 3-13. During the period 22 March 1972-22 May 1972, a decrease of about 1% occurred. The two week segment missing at the end of April 1972 was due to the paper drive jamming. The continuous segment (24 June 1972-4 August 1972: Figure 3-7) had a -0.1% change. Another 0.2% decrease occurred from 12 September 1972 to 23 October 1972. A 0.7% rise occurred from 25 October 1972 to 13 November 1972. During the next month (13 December 1972-13 January 1973) resistivity remained constant, but was followed by a 0.9% increase ending on 6 February 1973. Equipment changes put a large jump in the record. Another 0.7% increase followed this. The system was off the air until June 1973.
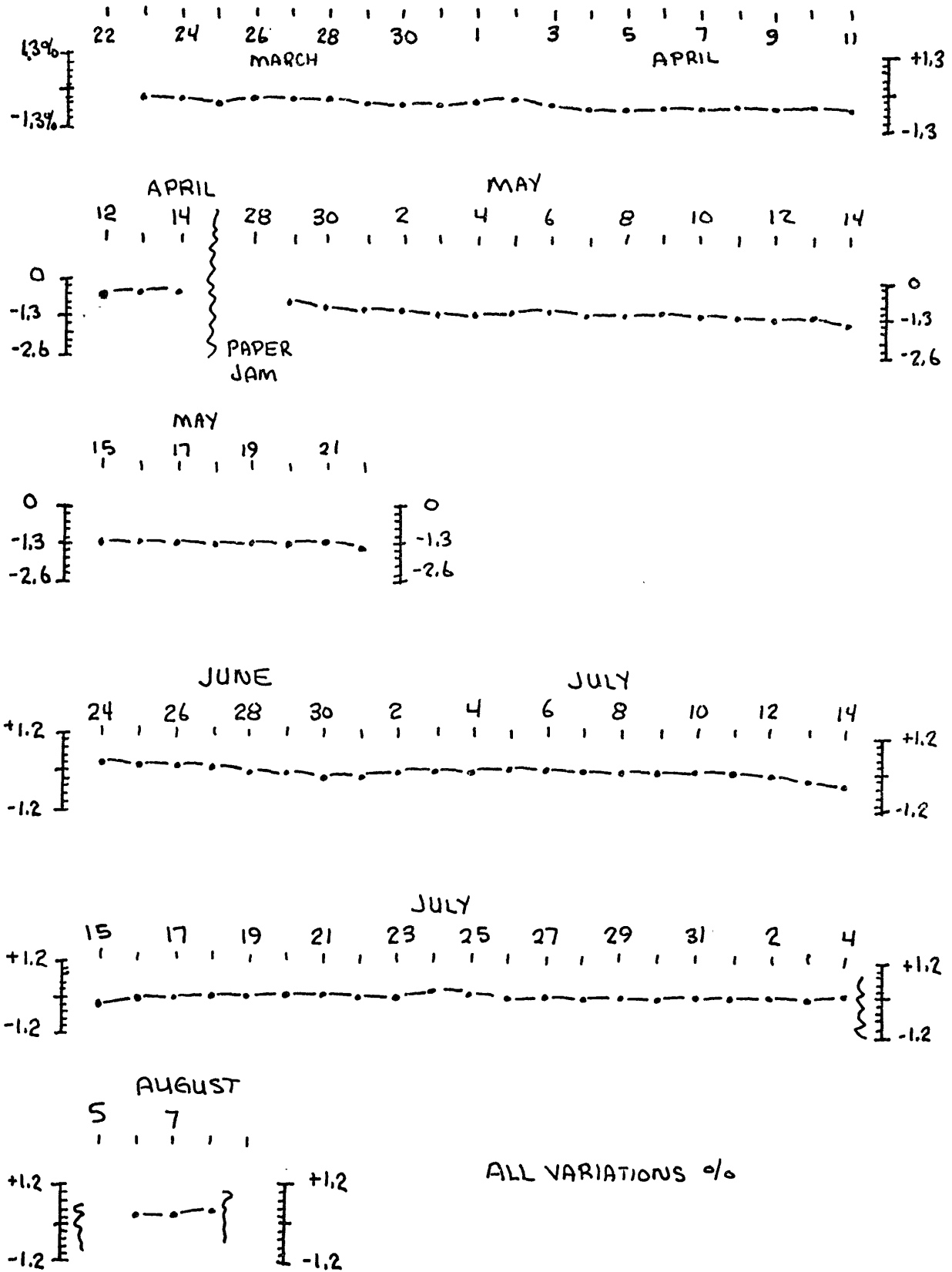
FIGURE 3-7 MELENDY RANCH RESISTIVITY VARIATIONS MARCH - AUGUST, 1972.

SEPT

11 13 15 17 19 21 23 25 27 29 1

+1.3

-1.3

OCT.

2 4 6 8 10 12 14 16 18 20 22

+1.3

-1.3

OCT
23   1

+1.3

-1.3

TELEMETRY
CHANGED

OCT   NOV

25 27 29 31 2 4 6 8 10 12 14

+2.6

+1.3

0.
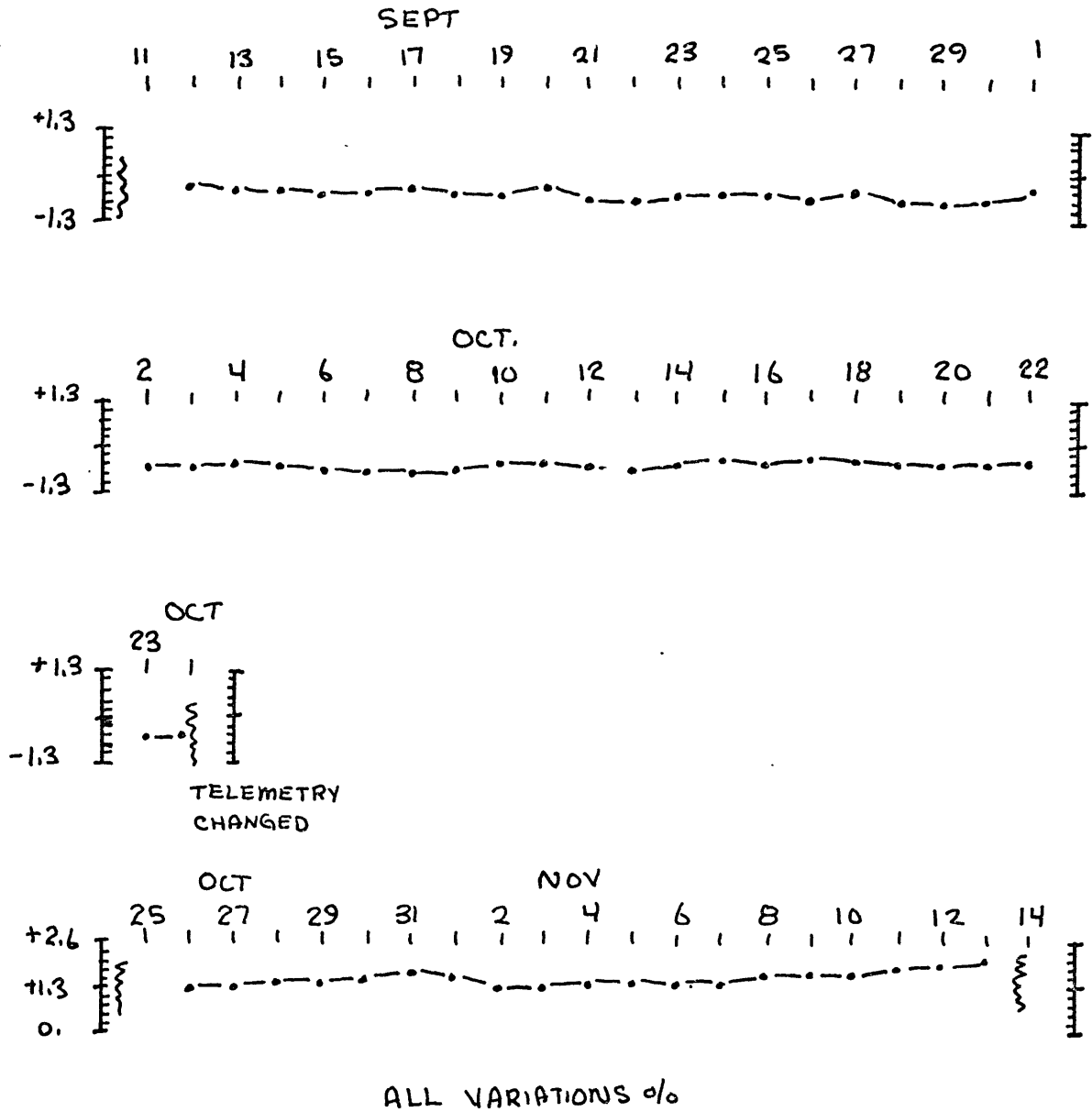
ALL VARIATIONS %

FIGURE 3-8 MELENDY RANCH RESISTIVITY VARIATIONS

SEPT- NOV 1972

87
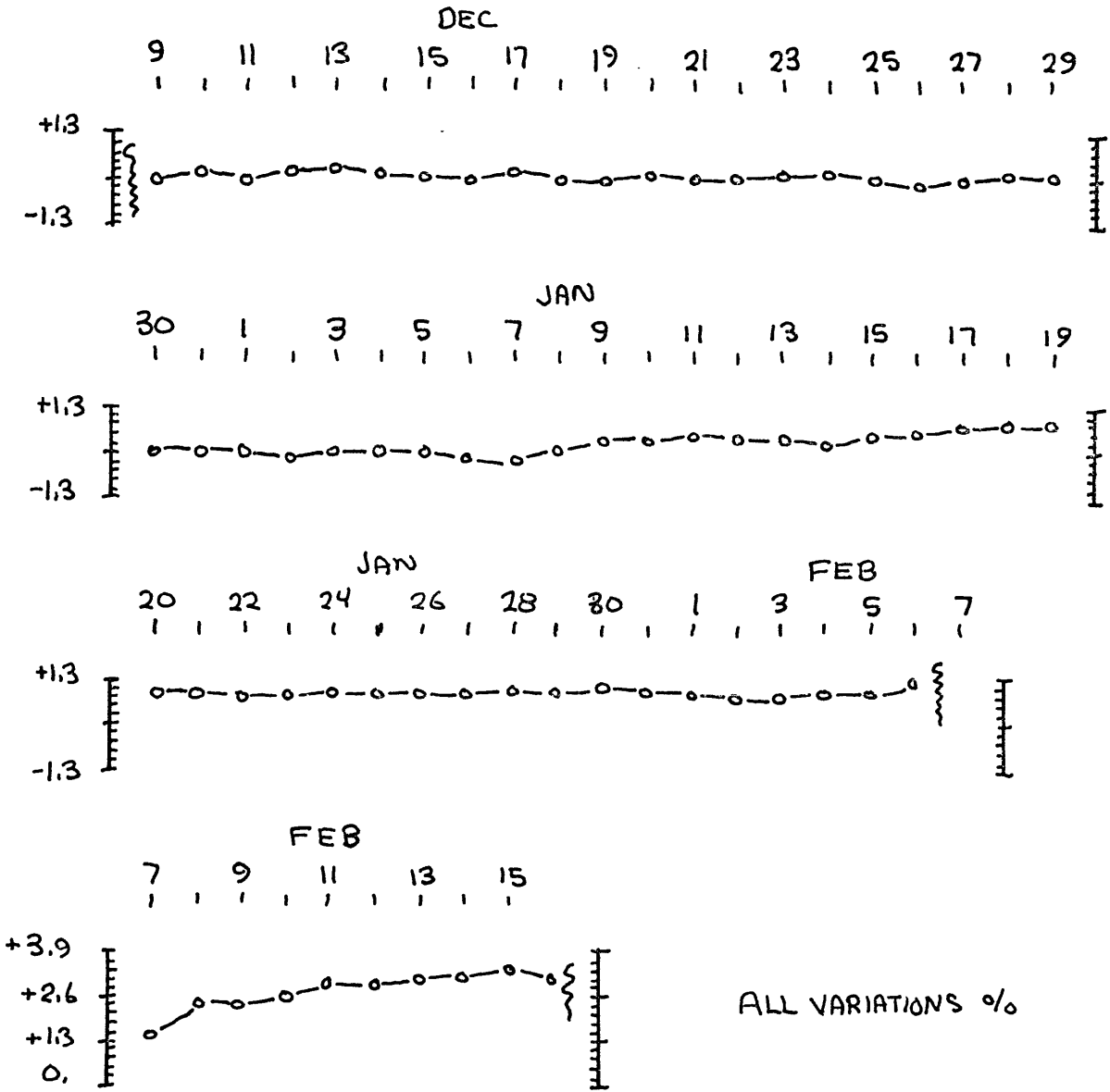
FIGURE 3-9 MELENDY RANCH RESISTIVITY VARIATIONS
DEC 1972 - FEB 1973

FIGURE 3-10 MELENDY RANCH RESISTIVITY VARIATIONS , DEEP RX ,

JUNE - JULY 1973 NO TEMP. CONTROL READINGS

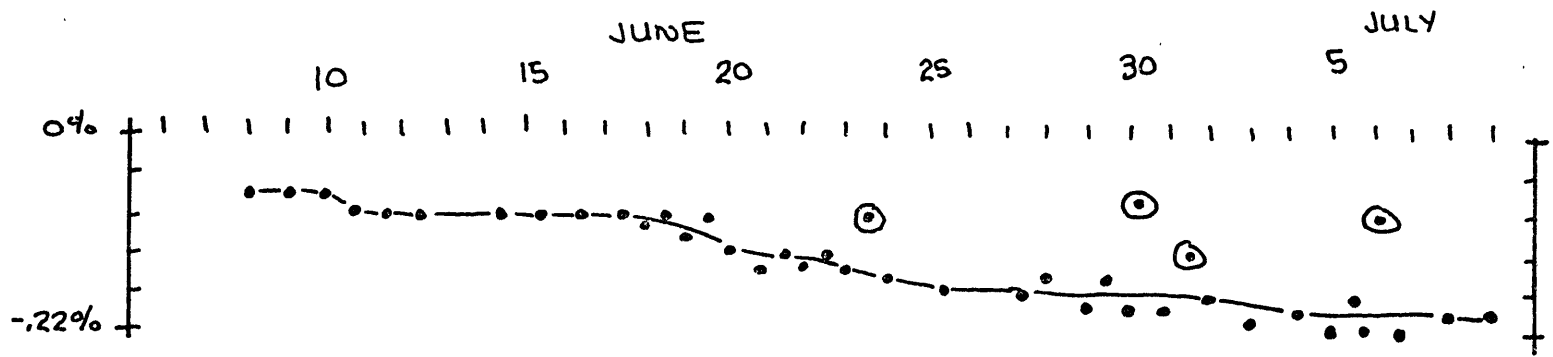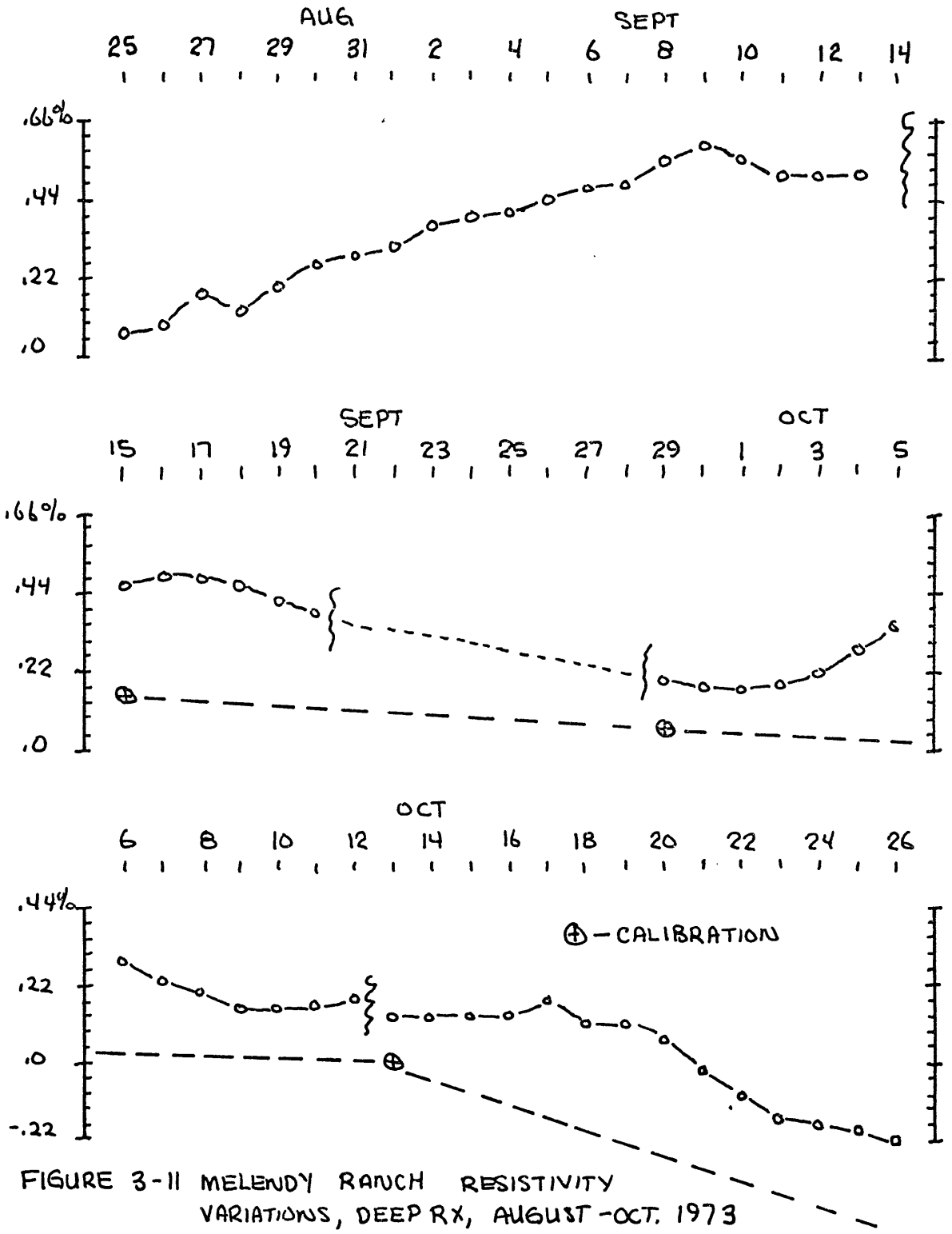AT 40°C CROSSINGS ⊙ INDICATES HIGH $\frac{\partial T}{\partial t}$

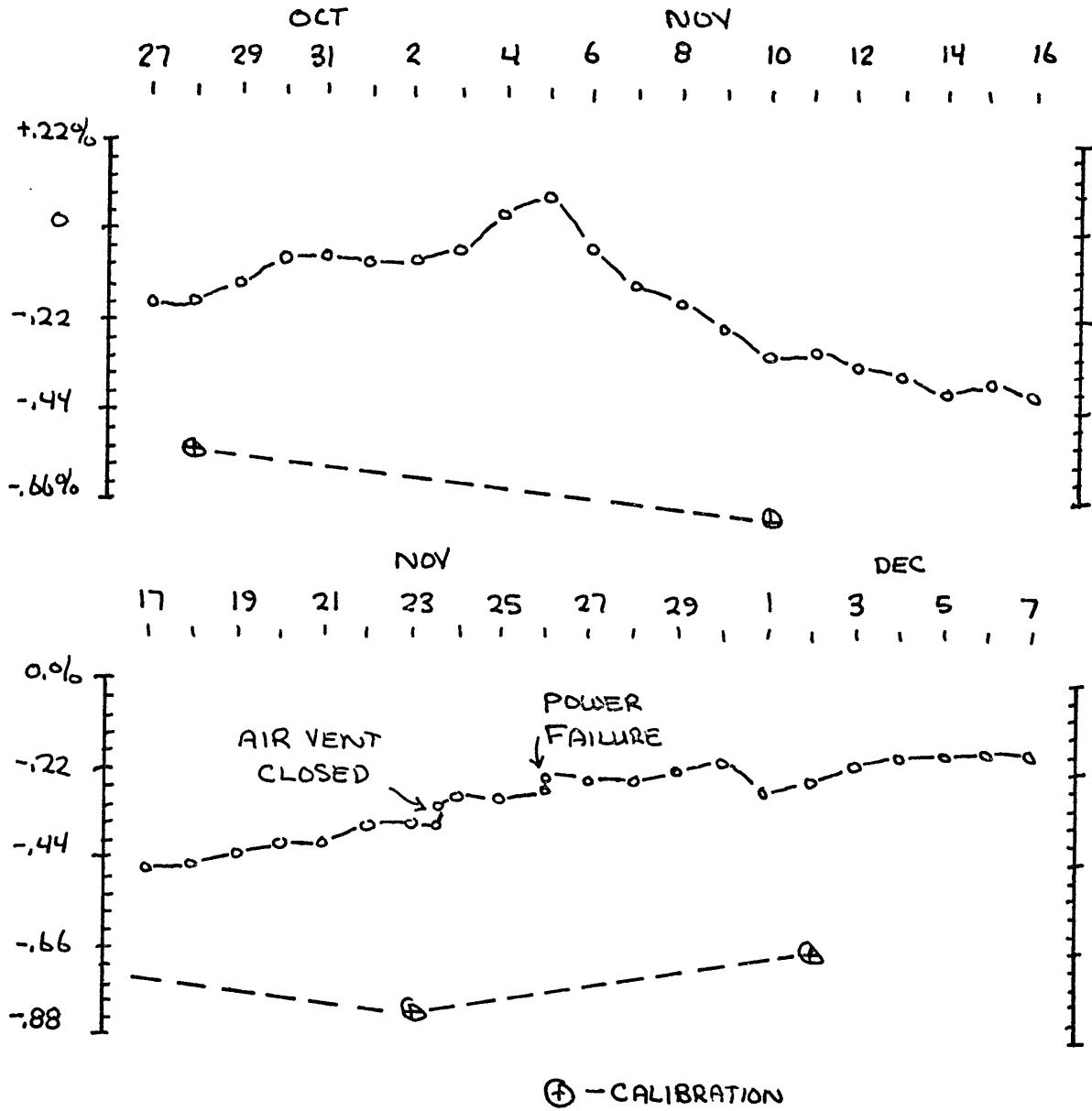FIGURE 3-11 MELENDY RANCH RESISTIVITY VARIATIONS, DEEP RX, AUGUST-OCT. 1973

FIGURE 3-12 MELENDY RANCH RESISTIVITY VARIATIONS,
.DEEP RX, OCT - DEC ,1973
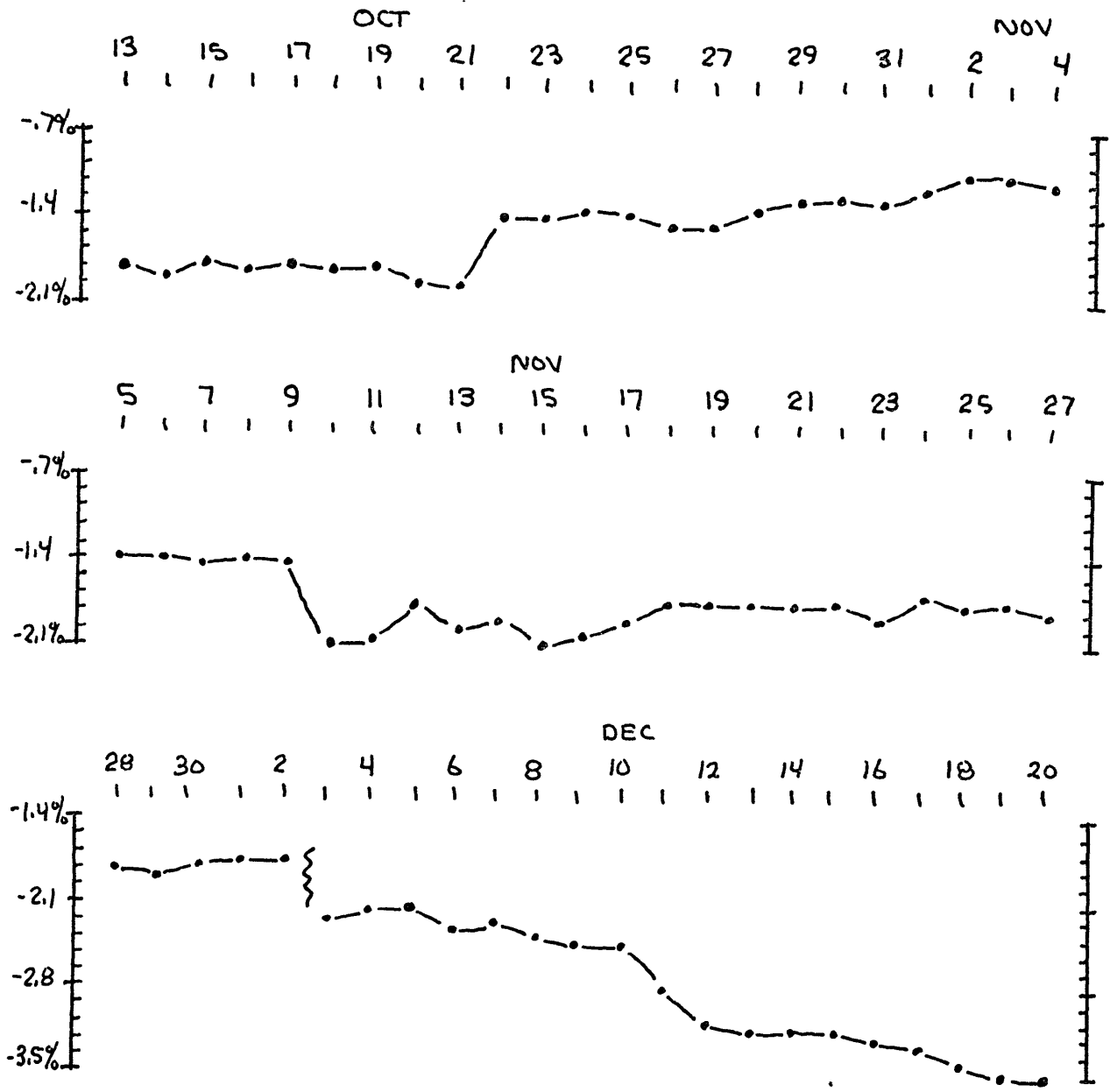
FIGURE 3-13 MELENDY RANCH RESISTIVITY VARIATIONS, SHALLOW RX, OCT 1973 - DEC 1973

The period 10 June 1973 to 9 July 1973 experienced a steady 0.15% decrease. This data segment is interesting because no temperature controller was being used. In spite of this, readings taken at 40°C temperature crossings were very constant. The transmitter electrode went dry and was not fixed until mid-September. This problem occurred several times, and was probably due to a small net D.C. current which drives water away from one of the electrodes by electro-osmosis. Pouring water around the drying electrode alleviated the problem.

Long term variations continued to decrease for both the deep and shallow receiver (Figures 3-11, 3-12, and 3-13). During October and November 1973 the shallow receiver remained constant, but dropped by about 0.1% in early December. The deep receiver, for this same period of time, showed an 0.5% increase in early September 1973. Beginning in mid-September, periodic calibration of the deep receiver was performed. The general trend to the resistivity variations appears to be correlated with the calibration value. There does, however, appear to be a 0.2% increase over this period. During the first two months of 1974 there was a large decrease of over 1.0%. Since the system has not been recalibrated since December 1973, it is not possible to say if these variations are real.

The general trend seems to be an increase in resistivity during the months when one would expect the average temperature

to be decreasing. In the spring, as temperatures rose, the resistivity usually decreased. Such a temperature dependence is to be expected. Diurnal variations are not seen because the depth to which the temperature variation penetrates is very small.

The surface layer ($\sim$50m) appears to be a very stable zone which undergoes long term changes of not more than 2.0% in a year. This is an important finding for people planning on measuring resistivity variations on a large scale, as large surface changes could hide variations attributable to to deeper zones. Rain did not appear to greatly influence the resistivity. This is most likely due to the low permeability of the clay found at the field site. Large ponds of water were often noticed, indicated that water percolates very slowly into the ground.

3.5 Influence of Surface Variation on Measurements

It is of interest to know the influence of surface resistivity variations on resistivity measurements. Several two layer cases will be considered with $\rho_1/\rho_2 = 100$, 1, and 1/100. The Schlumberger resistivity is given by (Grant and West, 1965)

$$\rho = R^2 \int_0^\infty \lambda^2 J_1(R\lambda) \bar{Z}(\lambda) d\lambda \qquad 3\text{-}1$$

For two layers

$$Z(\lambda) = \frac{\rho_1}{\lambda} \frac{\rho_2 + \rho_1 \tanh(\lambda \Delta z)}{\rho_1 + \rho_2 \tanh(\lambda \Delta z)} \qquad 3\text{-}2$$

where R is the electrode spacing and ΔZ the first layer
thickness. Sensitivity to the first layer is given by

$$S_1 = \frac{\rho_1}{\rho} \frac{\partial \rho}{\partial \rho_1} \qquad 3\text{-}3$$

The derivative in Equation 3-3 was computed analytically,
while the actual resistivity was computed for a pole-pole
geometry and numerically differentiated with respect to R
to obtain the Schlumberger (pole-dipole) results.

The results are presented in Figures 3-14, 3-15, and
3-16 for a variety of ΔZ's. For all cases S_1 decreases with
increasing electrode spacing with larger ρ_1/ρ_2 resulting in
a faster decrease. This means that for a site like Melendy
Ranch with a resistive surface layer, the influence of sur-
face variations will be minimal. For example when $\rho_1/\rho_2 = 100$,
$\Delta Z = 1$ m, and R = 100 m, S_1 is estimated to be much less
than 10^{-6}. When $\rho_1/\rho_2 = 1/100$ the sensitivity is increased
to $S_1 = 0.53$. In a case like this, surface variations pre-
sent a much greater problem. In general, surface variations
will be enhanced by a conductive surface zone. The effect of
surface variations for layered media can always be reduced
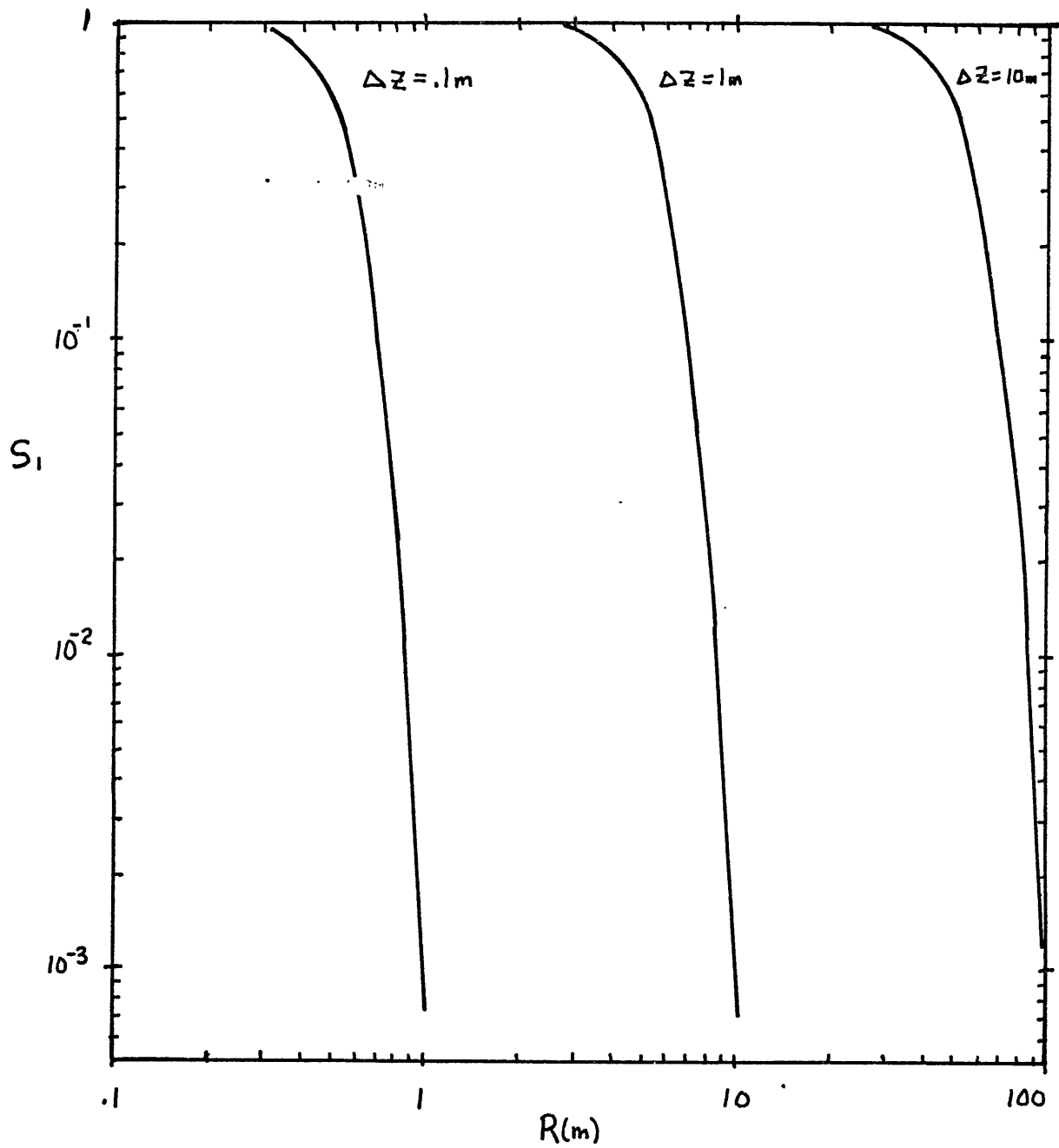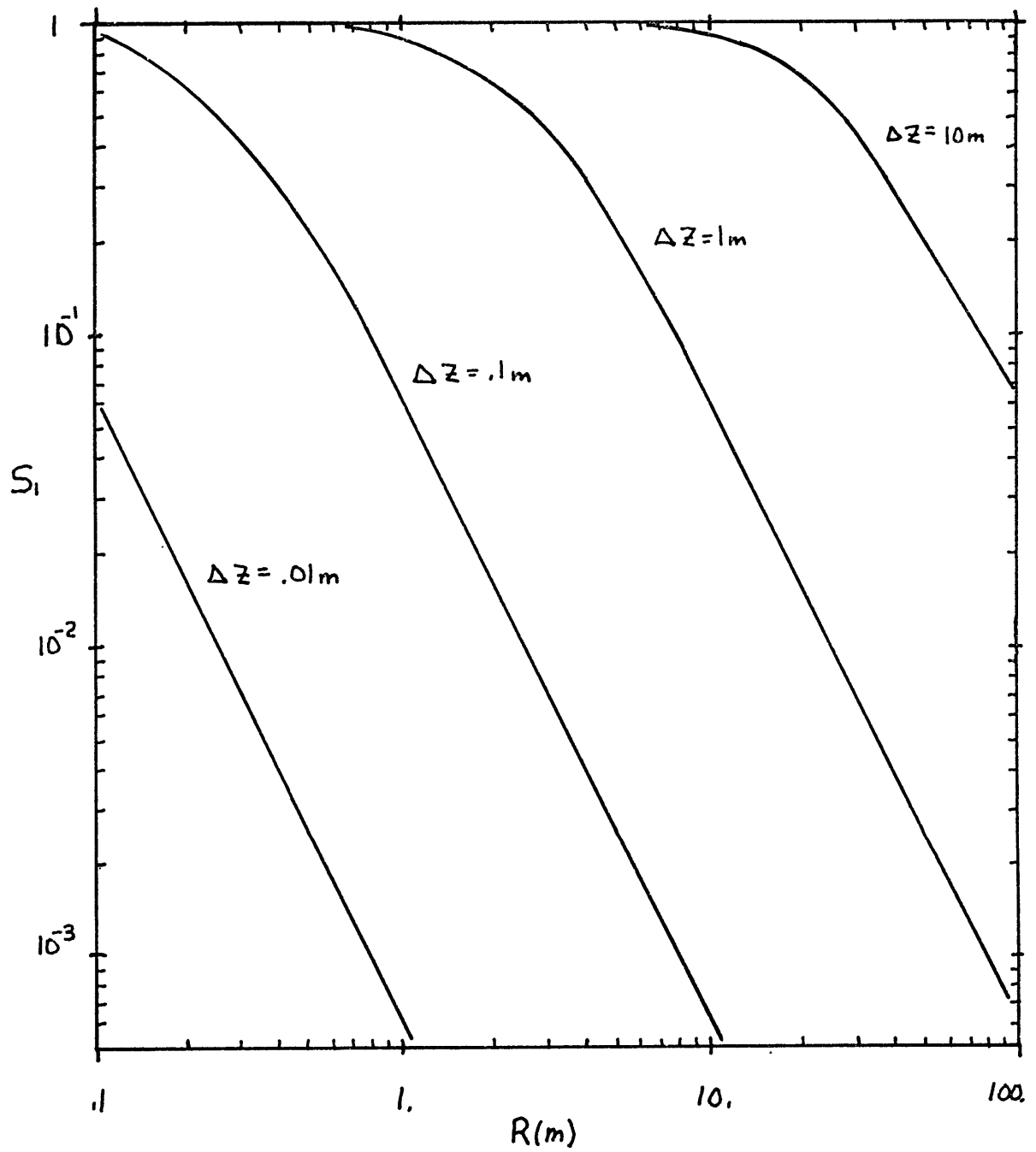by increasing the electrode spacing.

FIGURE 3-14 S_1 vs. R   FOR $\rho_1/\rho_2 = 100$

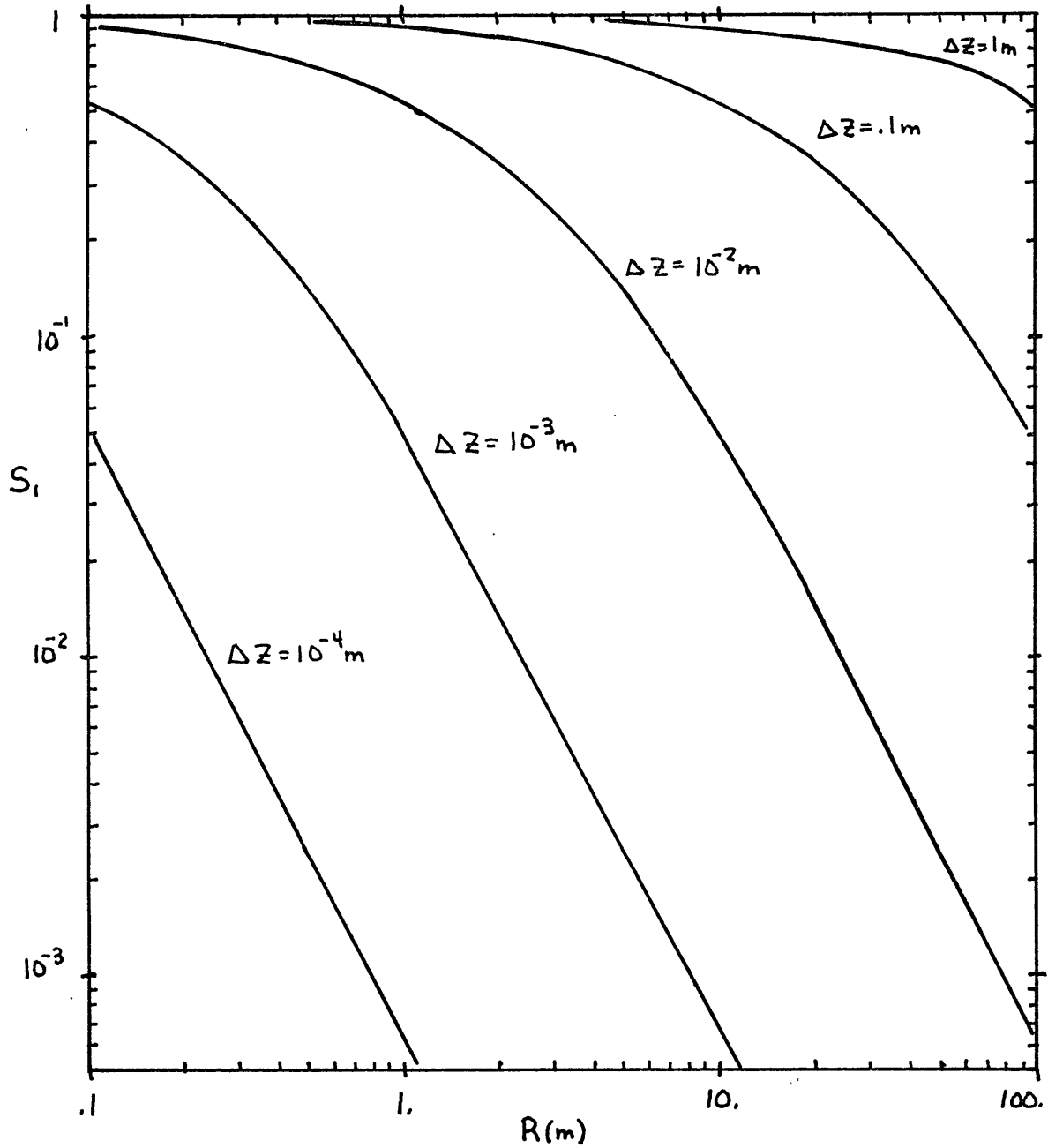FIGURE 3-15 S_1 vs. R   FOR $\rho_1/\rho_2 = 1$

FIGURE 3-16 S_1 vs. R   FOR $\rho_1/\rho_2 = 1/100$

Diurnal and annual temperature fluctuations are a possible source of resistivity variation whose magnitude is easy to estimate. Let us consider a case where the thermal diffusivity is 10^{-5} m^2/sec, and the surface diurnal and annual temperature variations are 8°C and 24°C respectively. This corresponds to a diurnal and seasonal skin-depth of 0.37 m and 7.1 m with respective average temperature variations of 5°C and 15°C. Changes in water viscosity due to temperature changes give rise to a -2.4%/°C change in resistivity. The corresponding average layer resistivity changes are 12% and 36% (Table 3-1). Assuming ΔZ = 1 m it would really be necessary to do a three layer sensitivity analysis to obtain the results for the cases of ρ_1/ρ_2 = 100 and 1/100. A two layer approximation to this can be made by obtaining the change of a layer ΔZ thick which is equivalent to changing a layer one skin-depth thick. This is done by using the fact that a thin resistive (conductive) layer is characterized by its resistivity (conductivity) thickness product (Madden, 1971). In the cases where $\rho_1/\rho_2 \geq 1$ the diurnal variations are not significant at R = 100 m (Table 3-1), while for the case of ρ_1/ρ_2 = 1/100 the diurnal variations are only cut down to 0.2% at R = 1 km. Seasonal variations are large enough to be observable for both the case of ρ_1/ρ_2 = 1 and 1/100 at separations of 100 m. In general, measurements will not be isolated from surface temperature variations until

$$\frac{R}{\Delta Z} \frac{\rho_1}{\rho_2} \gg 1.$$

Table 3-1

Resistivity Variations Due To

Surface Temperature Fluctuations

Thermal diffusivity $= 10^{-5} m^2/s$

Period	Skin Depth (m)	ΔT ($^\circ$C) Surface	$\overline{\Delta T}$ ($^\circ$C) Layer	$(\frac{\Delta\rho}{\rho})$ Layer
diurnal	.37	8	5	.12
annual	7.1	24	15	.36

$\Delta Z = 1$ m

ρ_1/ρ_2	R(m)	$(\frac{\Delta\rho}{\rho})$ diurnal	$(\frac{\Delta\rho}{\rho})$ annual
100	1	.044	.38
100	10	4.4×10^{-5}	3.8×10^{-4}
100	100	---	---
100	1000	---	---
1	1	.063	.36
1	10	1.2×10^{-3}	.27
1	100	1.2×10^{-5}	.01
1	1000	1.2×10^{-7}	10^{-4}
1/100	1	.044	.38
1/100	10	.040	.35
1/100	100	.023	.20
1/100	1000	.0021	.018

If Melendy Ranch is treated as a uniform half-space, one would expect annual resistivity variation of about 1%. This is rather close to the 1-2% annual change observed. In view of the fact that the temperature model neglects the effect of seasonal rain and wind variations which affect the surface temperature, the agreement is good.

3.6   Resistivity Variations Associated With Creep Events

The main purpose of the monitor was to determine if there are any resistivity variations associated with creep events which could possibly serve as predictors of, or at least give insights about, creep events. During the period 17 March 1972, when the monitor was installed, to 31 January 1974, there have been 18 distinct creep events during which the monitor was active. The list of these events is given in Table 3-2 (Burford, 1974). Four of the events were large with displacements over 2.0 mm, while over half had displacements of less than 0.4 mm. Also shown are the record sensitivity and the percentage change of resistivity. The sensitivity is taken to be 1/100 of full-scale on the chart recorders. In all cases no significant change was seen. The entry $\frac{\Delta\rho}{\rho}$ is really a measure of how stable the recording was.

An example from a small event (0.1 mm) which occurred on 9 September 1973 is given (Figures 3-17 and 3-18). The upper trace is equipment box temperature, the middle trace the deep

Table 3-2

List Of Melendy Ranch Creep Events And

Associated Resistivity Observation

Year	Date	Time* (GMT)	Slip (mm)	Record† Sens.(%)	$\frac{\Delta\rho}{\rho}$ (%)
1972	2 July	0735	2.32	.12	< .1
	15 Oct.	0907	0.18	.012	< .01
	26 Oct.	0937	2.68	.125	< .1
	31 Dec.	2011	0.16	.013	$< .1^{\infty}$
1973	11 Jan.	0312	2.8ь	.013	$< .1^{\infty}$
	11 Feb.	0200	1.1	.13	< .1
	12 Feb.	0730	0.70	.13	< .1
	3 July	1524	0.1	.044	< .04
	9 Sept.	2214	0.1	.002	< .006
	6 Oct.	2045	0.1	.044	< .04
	14 Oct.	1331	3.0	.002	< .005
	19 Nov.	1607	0.1	.002	< .002
	2 Dec.	0833	0.1	.002	< .002
	19 Dec.	2333	0.1	.14	< .14
1974	4 Jan.	2252	0.3	.14	< .14
	7 Jan.	1320	0.4	.14	< .14
	10 Jan.	1504	1.6	.14	< .14
	29 Jan.	0057	1.6	.14	< .14

*Subtract 8 h for Pacific Standard Time, 7 h for Pacific
 Daylight Time.
†Sensitivity taken as 1% of full scale.
∞Noisy record.

Event times and slips courtesy of R. O. Burford, USGS-NCER.

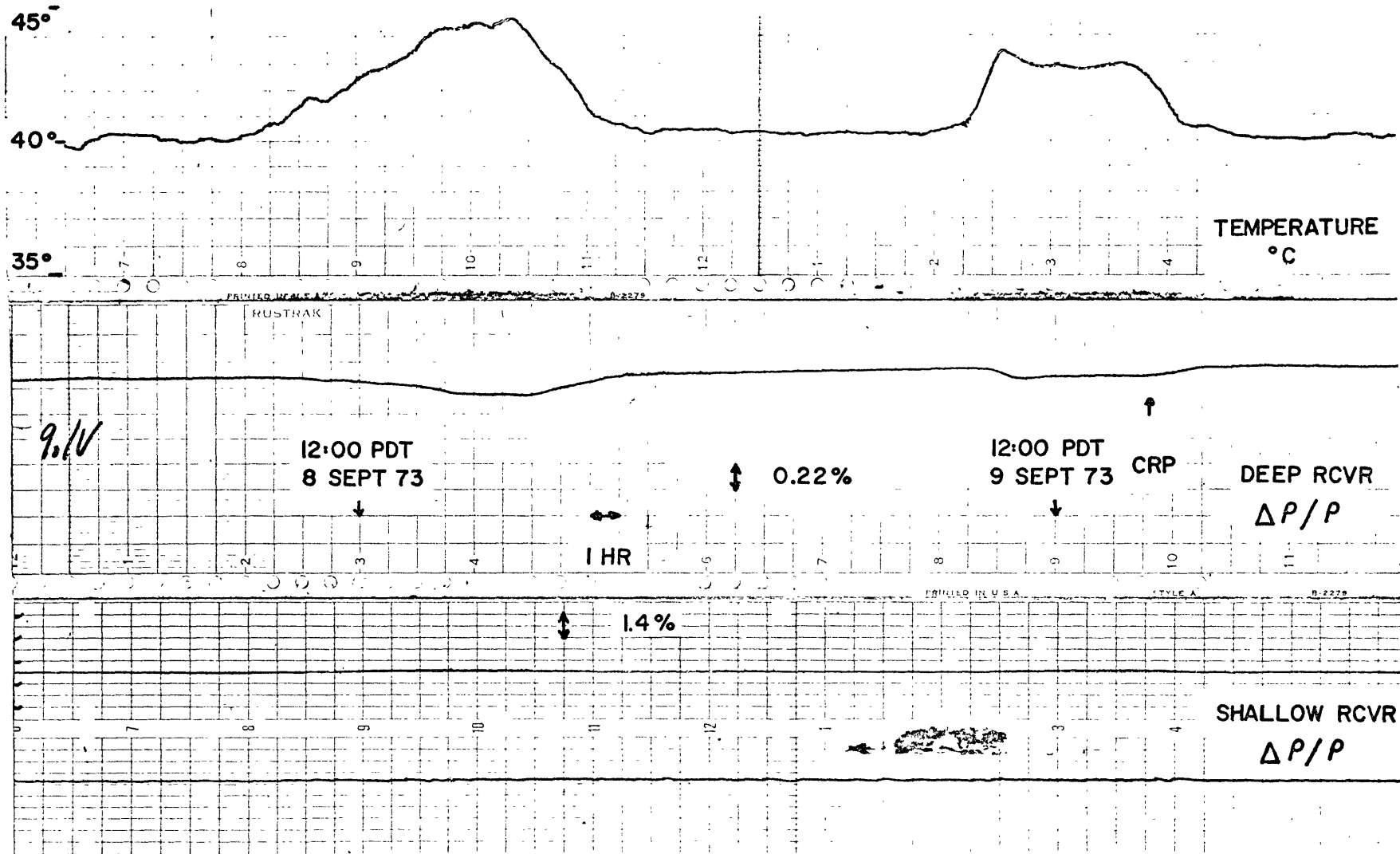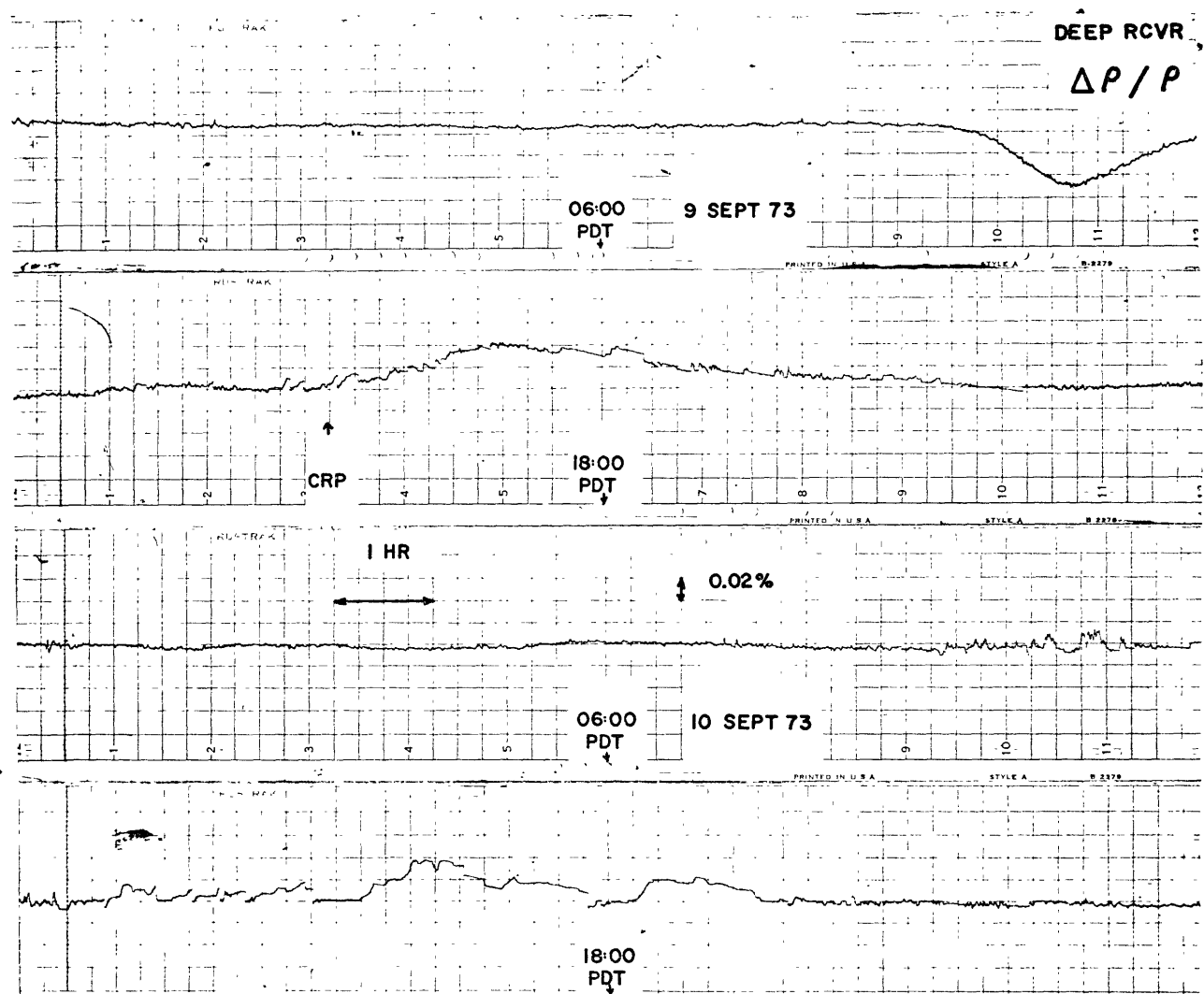FIGURE 3-17 MELENDY RANCH RESISTIVITY, SLIP=0.1mm, 15:14 PDT, 9 SEPT 73

DEEP RCVR

$\Delta P / P$

06:00 PDT   9 SEPT 73

CRP   18:00 PDT

1 HR   0.02%

06:00 PDT   10 SEPT 73

18:00 PDT

FIGURE 3-18 HI-PASS MELENDY RANCH RESISTIVITY, SLIP = 0.1mm, 15:14 PDT, 9 SEPT 73

receiver resistivity variations, and the lower two traces are from the surface receiver. (The upper of these two traces is the variation signal, and the lower is the total voltage measured.) The deep receiver is essentially constant for several hours either side of the time of the event. A decrease in resistivity occurs on the afternoons of Sept. 8 and 9 which is associated with a temperature rise. The surface receiver record is equally uneventful. The high sensitivity hi-pass records (Figure 3-18) was relatively quiet for several hours before the event. The noise level rose from 0.004% to 0.006-0.008% just before the event. The decrease of 0.05% at 10:45 PDT and the increase of 0.04% at 17:00 PDT are associated with the temperature fluctuations.

The records from the largest recorded slip (3.0 mm, 14 October 1973) are shown in Figures 3-19 and 3-20. The traces are the same as for the previous event. The creep event occurred at 06:31 local time. At this time there is no significant change in either trace which can be distinguished as being different from normal background behavior. About 12 hours after the event there was a resistivity decrease on the shallow receiver and an increase on the deep receiver which are associated with a change of box temperature. The opposite sense of temperature dependence of the two receivers has been noted frequently. It is fair to say that no significant resistivity changes associated with tectonic activity were observed at Melendy Ranch for the period
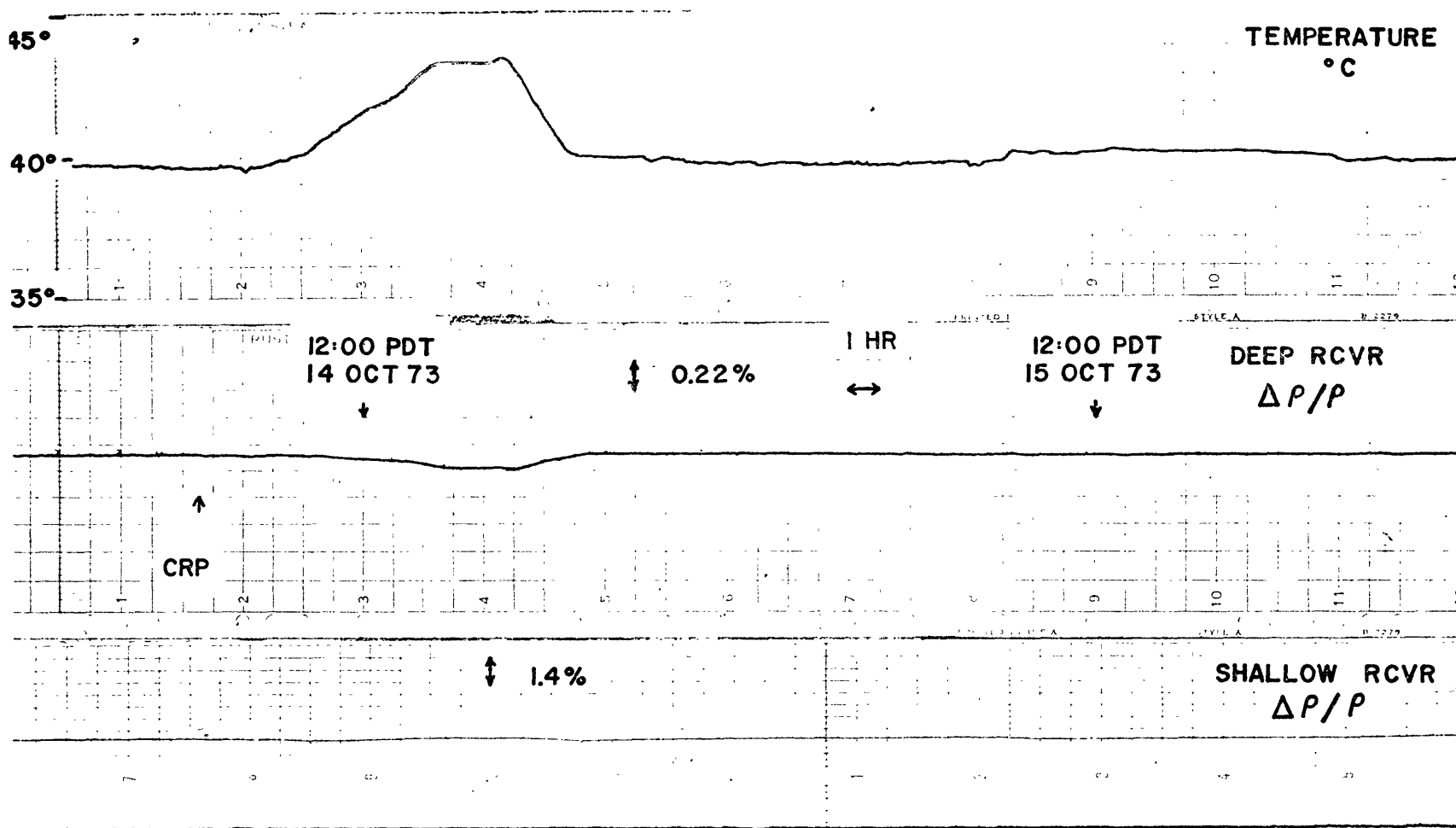
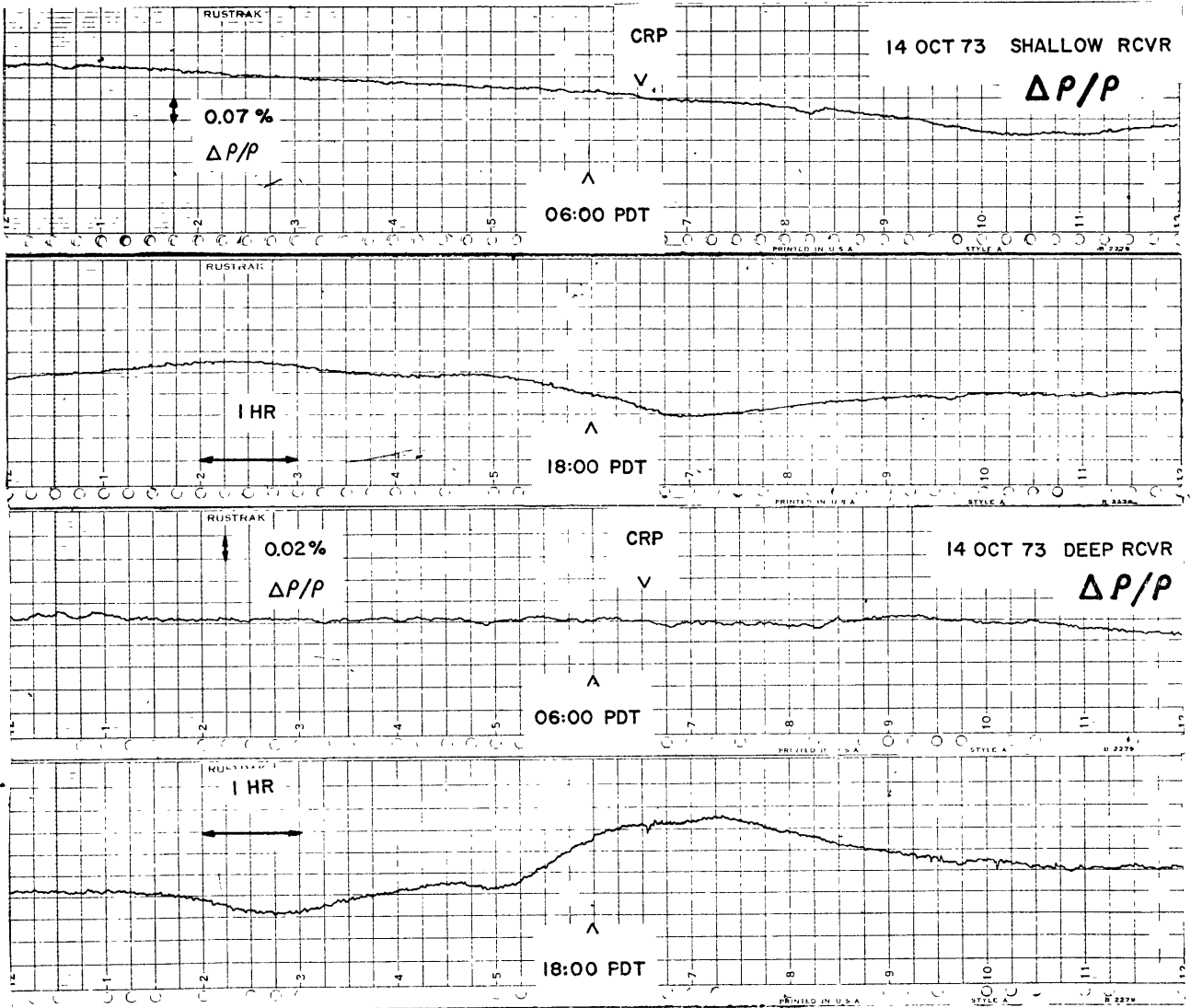FIGURE 3-19 MELENDY RANCH RESISTIVITY, SLIP=3.0 mm, 06:31 PDT, 14 OCT 73

FIGURE 3-20 HI-PASS MELENDY RANCH RESISTIVITY, SLIP = 3.0 mm, 06:31 PDT, 14 OCT 73

the resistometer has been in operation.

The sensitivity analysis of Section 3.5 can be used to estimate the thickness-resistivity variation product associated with a creep event. A uniform half-space with a vertical zone $2\Delta Z$ thick with the electrodes along the vertical zone is identical to the case presented in Figure 3-15. The important feature is that as R, the electrode spacing, becomes large compared to ΔZ, the sensitivity is inversely proportional to the square of the distance. This means the large array used (R = 100 m) was rather insensitive to variations associated with the fault plane, assuming $\Delta Z/R \ll 1$.

Using the information in Figure 3-15, it is possible to compute allowable combinations of ΔZ and $\Delta\rho_1/\rho_1$ for an observed $\Delta\rho/\rho$ and R. Figure 3-21 presents the results for R = 100 m. Based on the results of Chapter 2, the clay at the monitor site probably has a small resistivity change O(1%) associated with it during failure. This means if a change of <0.005% is associated with the 14 October 1973 creep event it could be attributed to a region $2\Delta Z$ = 6 m. wide or less having a resistivity change of 1%.

3.7 Explanation of Electrical Stability of Melendy Ranch Site

As pointed out before, the Melendy Ranch site is composed primarily of silty-clay material. X-ray diffraction analysis revealed the primary clay mineral was from the montmorillonite family. These minerals have particle shapes similar to

FIGURE 3-21 THICKNESS AND RESISTIVITY VARIATION OF GOUGE ZONE FOR DIFFERENT OBSERVED RESISTIVITY VARIATION
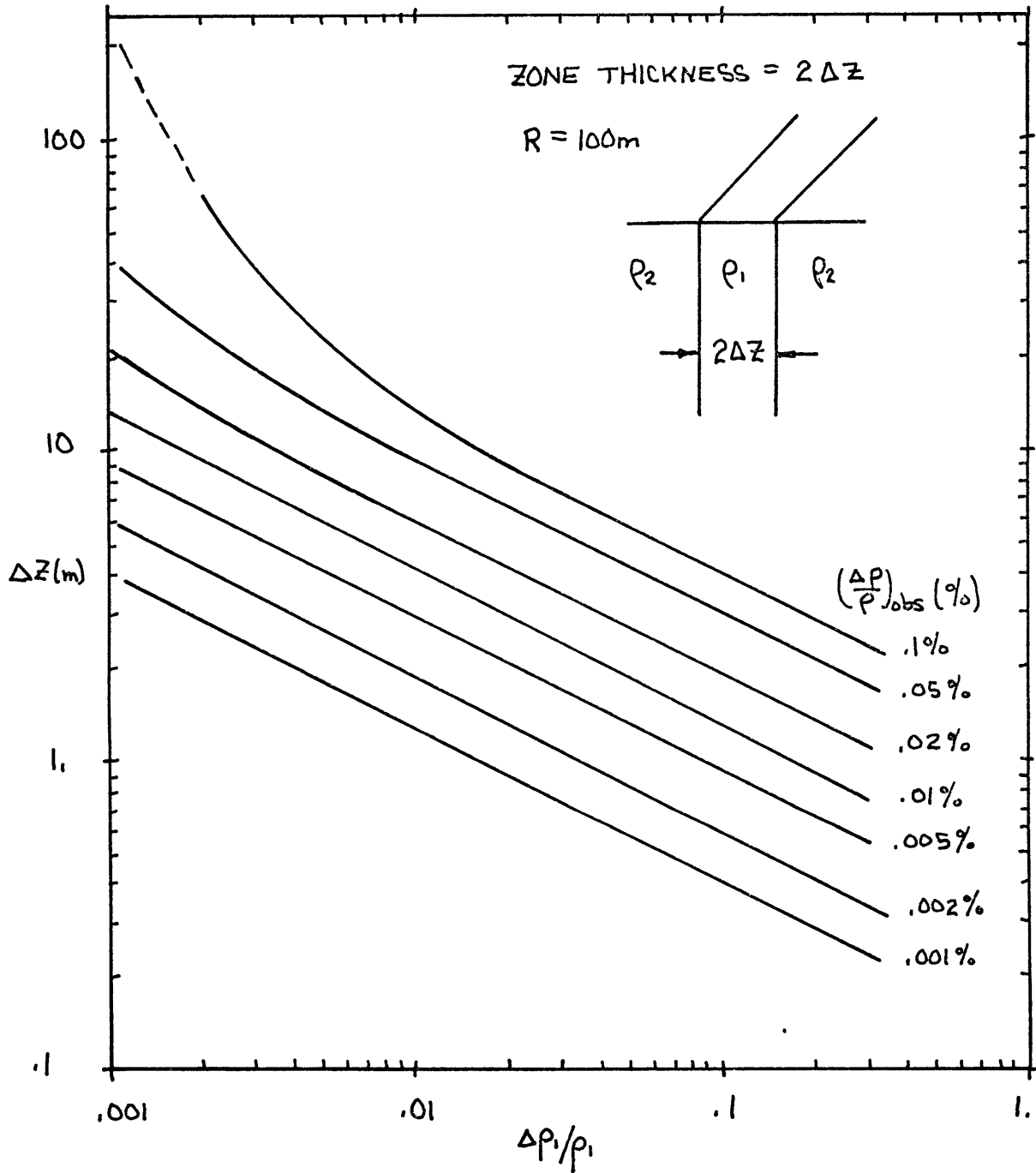
kaolinite. While laboratory experiments were not performed on field samples due to the poor quality of the samples, and the long times which would be required for fluid flow, it is felt that the electrical behavior of the field material during failure is similar to that presented in Chapter 2. This is said because fabric was the most important factor controlling resistivity during failure and the particle shapes are similar for the two clays. Similar resistivity behavior was observed for illite which also has platey grain shapes.

When a creep event takes place one side of the fault slips quietly past the other. Clay particles along the fault plane tend to be aligned parallel to the fault. This phenomenon was observed on laboratory samples which are allowed to slide along the failure surface. A very silky-greasy luster was noted due to orientation of the particles. This orientation was confined to the slide surface since no drastic change in resistivity was noted during sliding. It has been noted by McKeyes and Yong (1971) that the width of this zone of strong reorientation is very narrow, approximately 20-40 μm wide for kaolin. The creep events seem to be confined to the same, or at most a few distinct breaks. Once the clay particles are aligned by previous creep events there should be no further reorientation by future events, and no change in the electrical properties.

One might argue that there should be some fluid flow associated with the creep event which would change the clay resistivity. Well measurements at Cienega Winery found pore pressure fluctuations $O(10^{-2}$ bar) associated with creep events (Johnson et al., 1973). Assuming a bulk modulus of 10^4-10^5 bars for the material around the well, one expects volumetric strain variations of 10^{-6}-10^{-7}. Porosity changes this small would account for resistivity variations of about the same order of magnitude. In view of these data, it is not surprising that no detectable resistivity change can be associated with creep events.

3.8 Conclusions

While the Melendy Ranch resistivity monitor did not detect any resistivity variations attributable to creep events, it did provide some useful information. First, if resistivity changes $O(1\%)$ are taking place during creep events, they are confined to a very narrow zone only several meters wide. This suggests there is a preferred plane along which all slippage takes place. This is born out by alignment arrays across active creep zones (Nason, 1971). Second, the experiment provides estimates of the near surface electrical stability. The zone sampled by the monitor (~ 50m) is stable over long periods of time with seasonal variations $O(1\%)$ which are attributable to temperature fluctuations of the ground. This reduces the possibility of the surface layer acting as

a noise source for large-scale measurements in this area. In general, regions with resistive surface layers will be less sensitive to surface variations than regions with conductive surface layers. Surface layer sensitivity can be reduced by increasing the array spacing.

CHAPTER 4: ELECTRICAL RESISTIVITY OF ROCKS

4.1 Introduction

The purpose of this chapter is to review what is known about the electrical properties of rocks and to estimate the effect on resistivity of stress systems which have not been tested in the laboratory. The effect of non-mechanical factors, as well as isotropic and anisotropic stress systems will be considered. In addition estimates of the effect of pure shear on resistivity will be made. This information is essential in computing the effect of tectonic loading on simple strike-slip fault models to estimate the resistivity variations produced. This chapter will also serve as a basis for comparison of the electrical properties of clays discussed in Chapter 2.

4.2 Non-Mechanical Factors

Conduction through rocks at temperatures below $300^\circ C$ is controlled by five factors: 1) the conductivity of the pore fluid, 2) the rock porosity, 3) the degree of saturation, 4) the size of saturated pores, and 5) the interconnectivity of the pores. For sufficiently high pore fluid conductivity Archie's law adequately describes the rock conductivity.

$$\sigma = \sigma_0 \, (n \, s)^m \qquad\qquad 4\text{-}1$$

where σ_0 is the pore fluid conductivity, n the porosity, s the degree of saturation, and m a constant, typically 2 for crystalline rocks (Brace, Orange and Madden, 1965). The relationship appears to hold for values of porosity spanning almost three orders of magnitude.

When the product of pore diameter and pore fluid conductivity becomes small, another type of conductivity becomes important. The silicate framework of rocks has a net negative surface charge which is equalized by an excess of positive ions in the vicinity of the surface (Figure 4-1). This region is called the diffuse layer. Moving towards the center of the pore the number of positive and negative ions becomes equal. The amount of conduction contributed by the excess ion population is given by

$$\sigma_S = \sqrt{\frac{2\epsilon RT}{\pi F^2}} \, c \left(\cosh \frac{e\zeta}{2kT} - 1 \right) \qquad 4\text{-}2$$

where c is the pore fluid concentration, and ζ the zeta potential (Overbeck, 1952). The conductance of a cylindrical pore is the parallel combination of the surface and volume conductance parts

$$Y_p = 2\pi r \, \sigma_S + \pi r^2 \sigma_0 = \pi r^2 \sigma_{0_{eff}} \qquad 4\text{-}3$$

where r is the mean pore radius, σ_s the surface conductivity and σ_0 the pore fluid conductivity. The pore radius where the surface and volume conduction are equal is given by
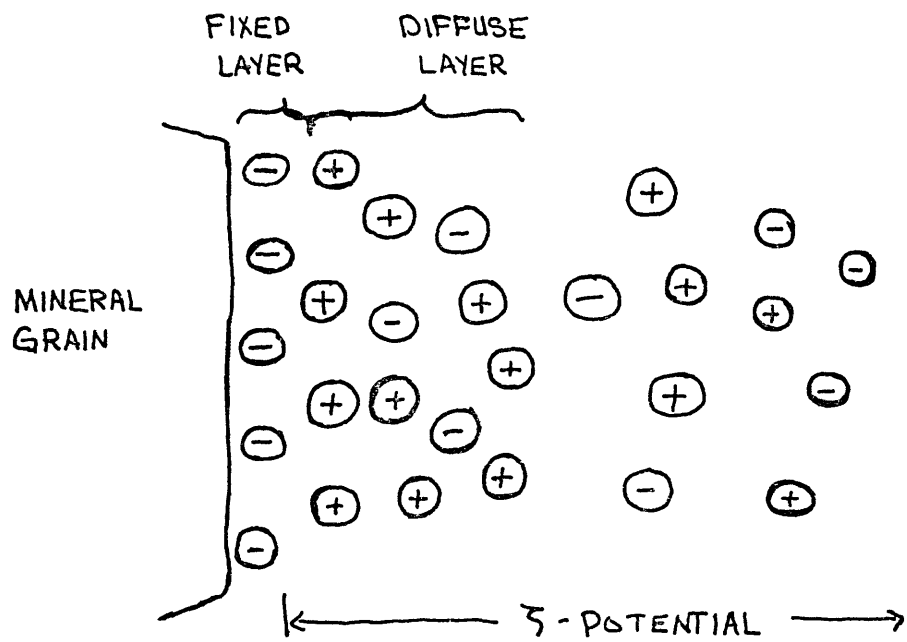
FIGURE 4-1   SURFACE CONDUCTION MECHANISM

$$r' = \frac{2\sigma_s}{\sigma_o} \qquad\qquad 4\text{-}4$$

For a fluid resistivity of 100 Ωm, r' is typically 4×10^{-5} to 4×10^{-7} centimeters depending on the magnitude of the zeta potential.

4.3 The Effect of Confining Stress

When the volumetric strain of a rock is measured as a function of confining stress, a curve similar to Figure 4-2 is obtained. The overbar denotes effective stress, $\bar{\sigma} = \sigma\text{-}P$, where P is the pore pressure. The curve bends rapidly at first, and then becomes linear. The "knee" in the curve is attributed to the closing of crack porosity (Brace, 1965). Since closing of cracks represents a loss of porosity one would anticipate a rather large change in resistivity due to confining stress (Brace et al., 1965). Figure 4-3 shows that this is indeed the case. Typically resistivity increases by an order of magnitude or more due to the closing of crack porosity. After all cracks are closed, ($\bar{\sigma}_c \sim 4$ kb) resistivity for brine saturated rocks is found to increase according to the equation (Brace and Orange, 1968b)

$$\frac{1}{\rho} \frac{\partial\rho}{\partial P} \simeq 0.1 \text{ kb}^{-1} \qquad\qquad 4\text{-}5$$

Assuming s = 1, and m = 2, and differentiating the resistivity form of Equation 4-1 ($\rho = \rho_o n^{-m}$) with respect to pressure
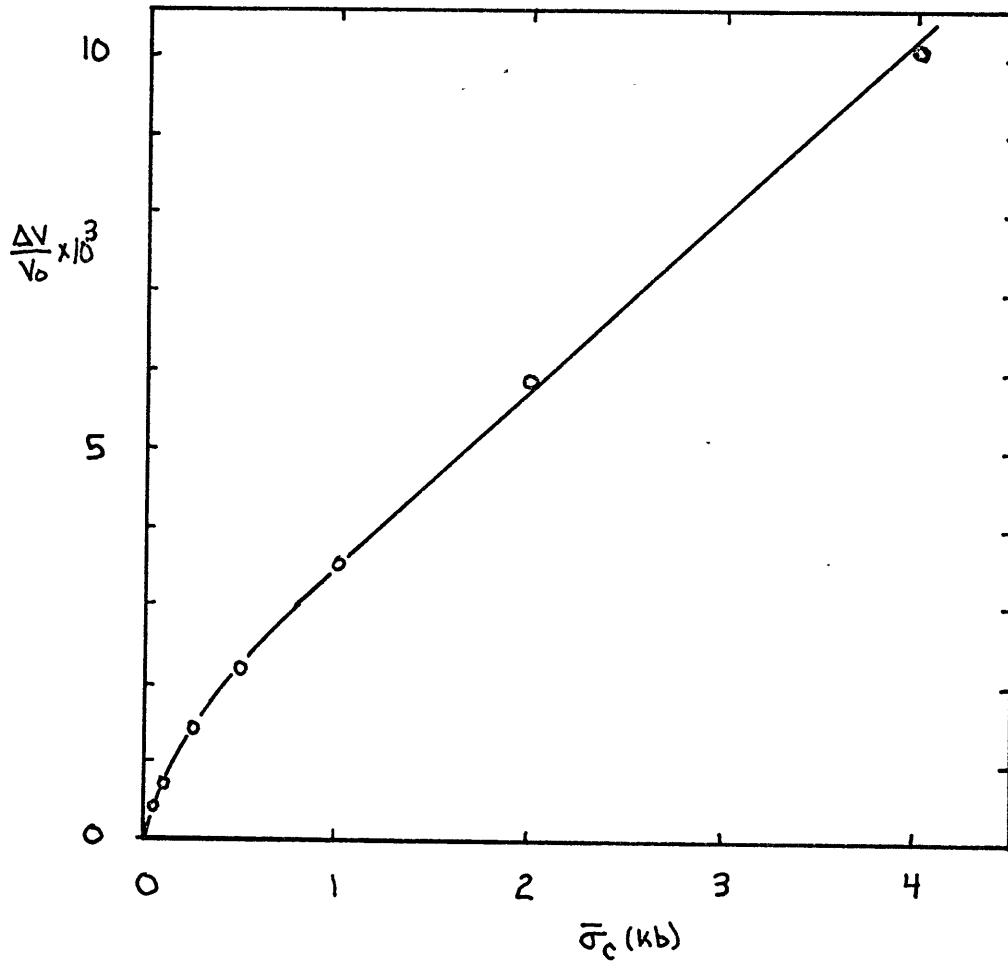
FIGURE 4-2 VOLUME COMPRESSIBILITY OF WESTERLY

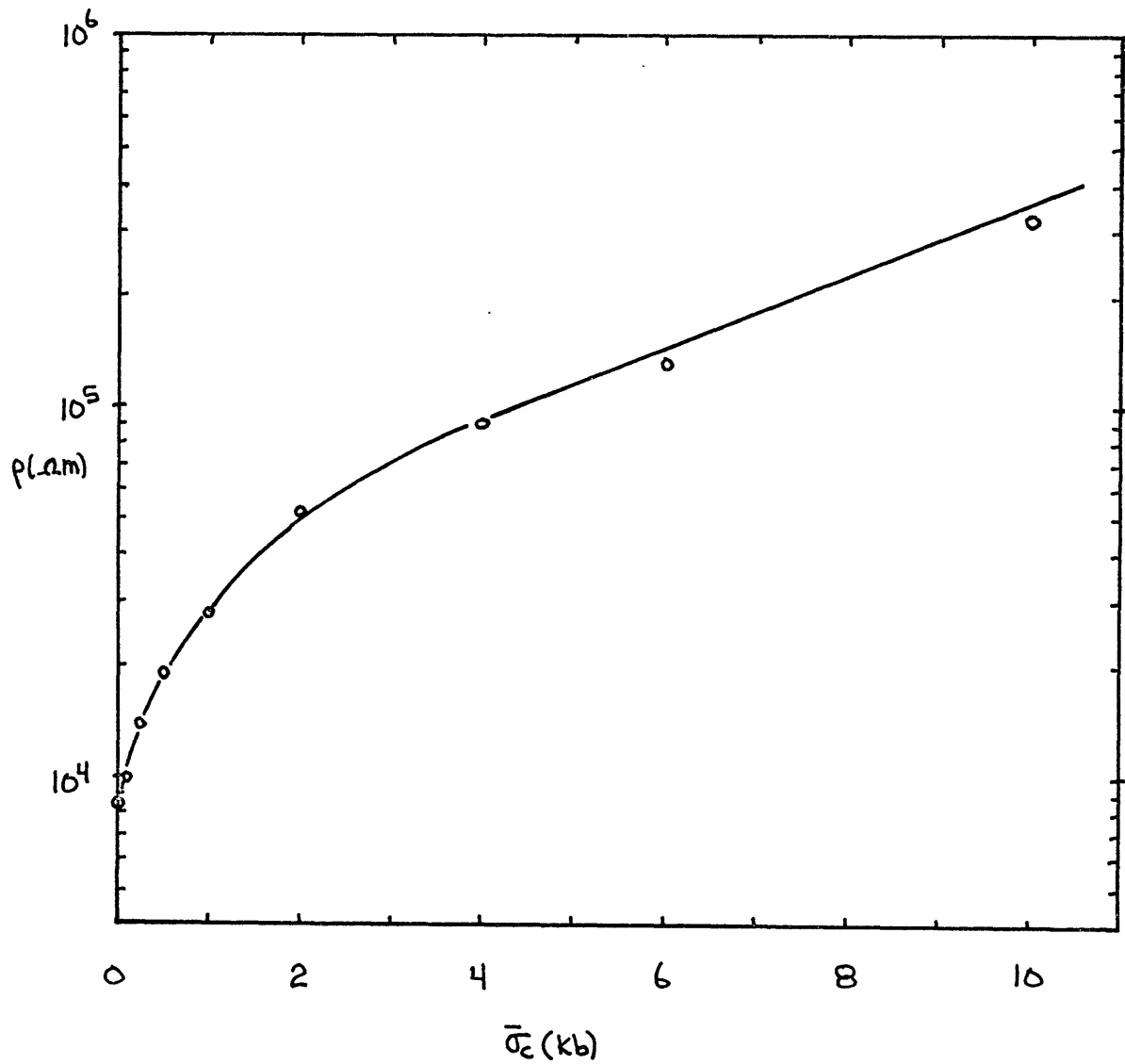GRANITE (BRACE ET. AL. ,1965)

FIGURE 4-3 RESISTIVITY OF WESTERLY GRANITE AS

A FUNCTION OF $\bar{\sigma}_c$ (BRACE ET AL., 1965)

gives

$$\frac{1}{\rho}\frac{\partial \rho}{\partial P} = \frac{1}{\rho}\frac{\partial \rho}{\partial n}\frac{\partial n}{\partial P} = \frac{2}{nK_b} \simeq \frac{2}{(.01)(.5mb)} = .4 \ K_b^{-1}$$

which is reasonably close to the experimental result.

The pressure dependence of resistivity was used by Yamazaki (1967) to measure changes in earth strain due to tidal loading. Measurements were made close to the ocean in a cave in a lapilli tuff. Strain changes of 10^{-6} were found to produce resistivity variations of 10^{-3}. This result is rather surprising for such a high porosity rock where crack closure would not be thought to be significant. For Westerly granite $\frac{\Delta \rho}{\rho}/\varepsilon$ is only about 500.

4.4   Effect of Triaxial Loading

To understand the behavior or resistivity during triaxial loading we again start with the volumetric strain-stress $(\sigma_1 - \sigma_2)$ diagram (Figure 4-4). In region 1 the rock is contracting elastically due to the increased stress. The second region is characterized by more elastic compression as well as slight sliding between grains. Removal of the stresses anywhere in region 1 or 2 results in complete recovery of strain. At C' (roughly equal to half the fracture stress, C) the rock starts to dilate. The dilation is caused by increased sliding of grains and formation of cracks. The rock becomes stronger as cracks form due to dilatancy hardening. The new pore volume is not completely recoverable.
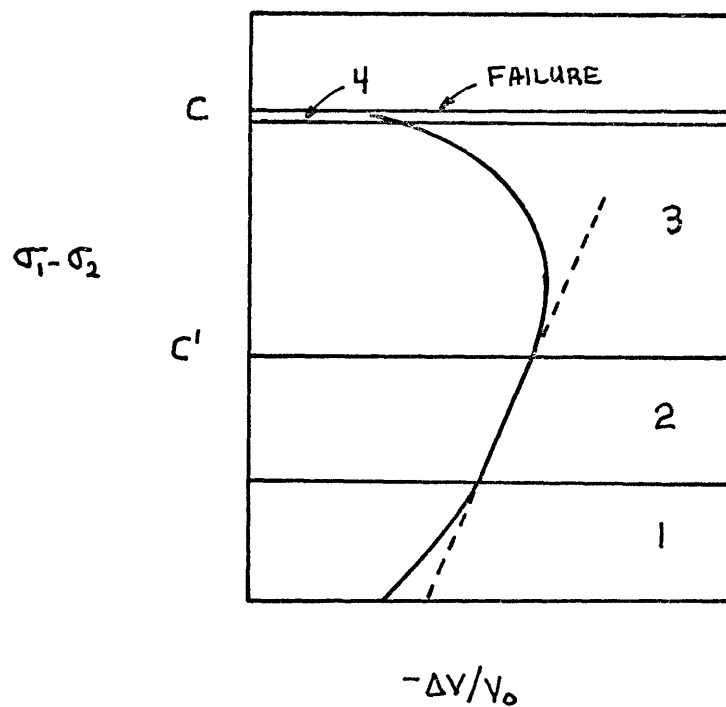
FIGURE 4-4 $\Delta V / V_0$ VS. $\sigma_1 - \sigma_2$ FOR CRYSTALLINE
ROCK (BRACE ET AL. ,1966)

With increased stress the cracks lengthen and intersect one
another until a crack (fault) extends all the way across
the sample (region 4).

Based upon the effect of confining stress one would
expect the resistivity to initially increase as cracks are
closed, and then decrease as new cracks form. Typical data
for Westerly granite (Brace and Orange, 1968a) at several
confining stresses are given in Figure 4-5. The resistivity
is seen to increase until the stress difference becomes
about half the failure value. At this point the resistivity
drops sharply. Increasing the confining stress increases
the initial resistivity and failure stress, but not the rela-
tive shape of the curve. Figure 4-6 shows the same data
normalized to the resistivity at $(\sigma_1-\sigma_2) = 0.0$ as a function
of percentage of failure stress (shear failure index, SFI).
The resistivity rises by about 50% at a point corresponding
to C'. A large drop of a factor of four accompanies the onset
of failure.

4.5 Estimates of the Effect of Pure Shear

The laboratory results cited in the last section represent
the combined effects of two loading systems on resistivity.
The experiments were conducted by increasing the maximum prin-
cipal stress σ_1 while keeping σ_2 and σ_3 $(\sigma_2=\sigma_3)$ constant.
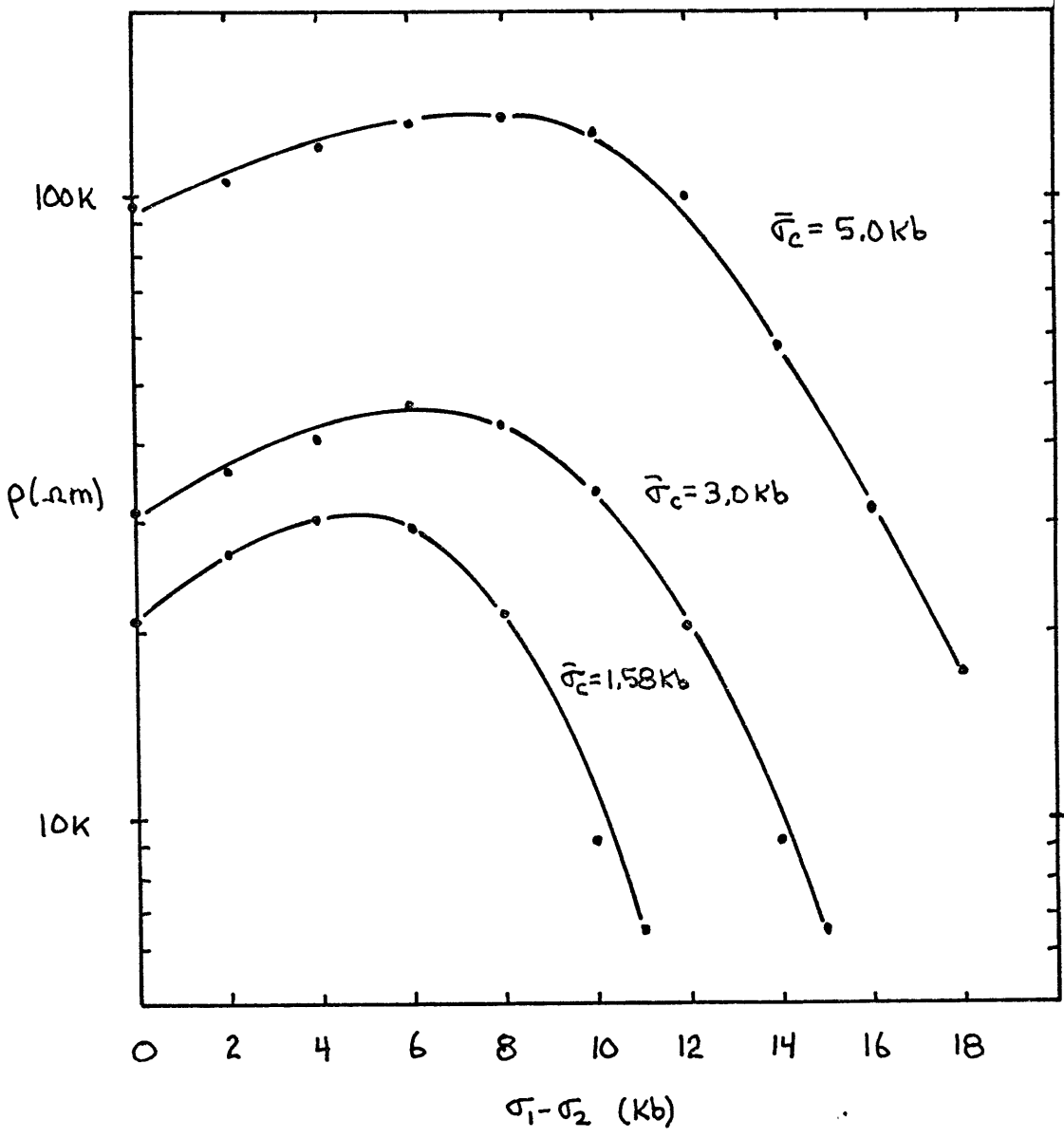This results in the maximum shear stress

FIGURE 4-5   RESISTIVITY OF WESTERLY GRANITE
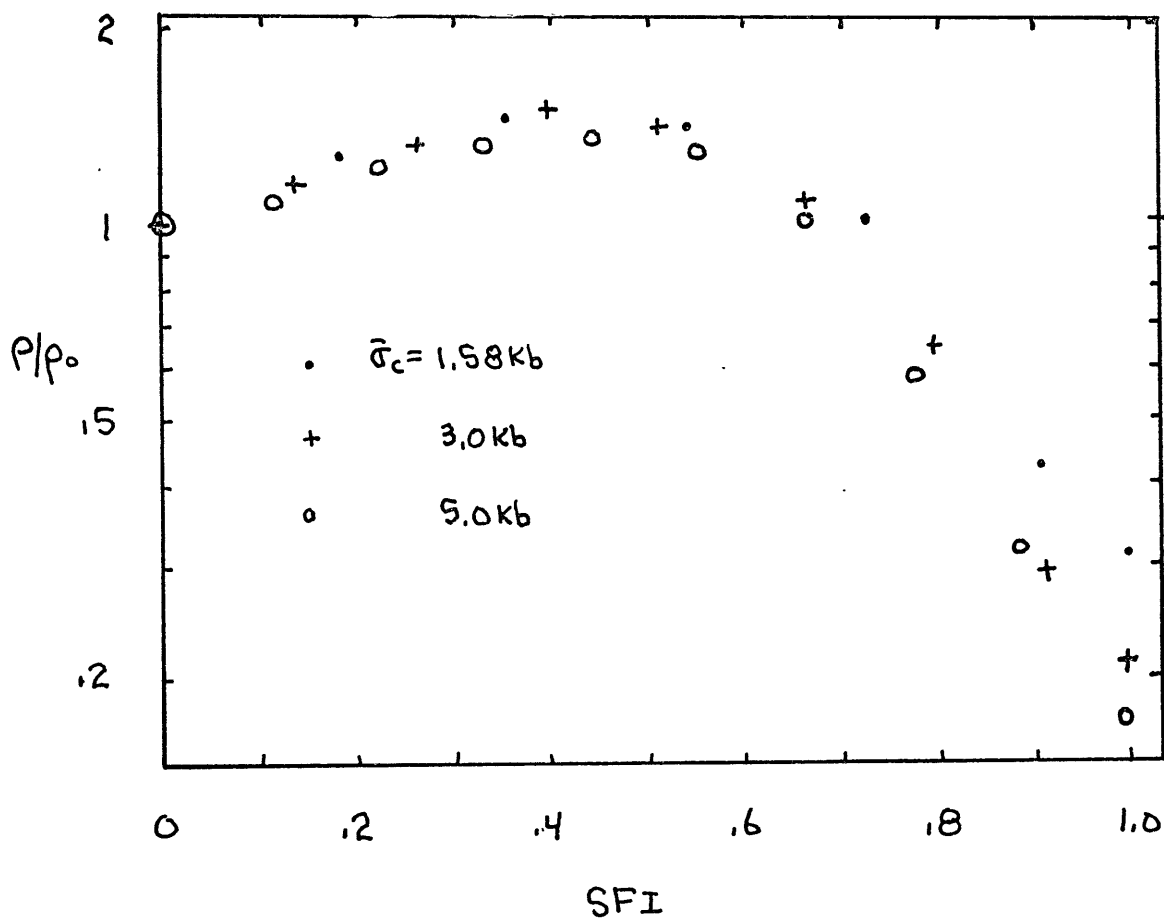DURING TRIAXIAL COMPRESSION
(BRACE AND ORANGE, 1968a)

FIGURE 4-6 NORMALIZED RESISTIVITY OF WESTERLY
GRANITE VS. SFI

$$\tau = \frac{\sigma_1 - \sigma_2}{2} \qquad\qquad 4\text{-}6$$

as well as the average stress,

$$\langle\sigma\rangle = \frac{\sigma_1 + \sigma_2 + \sigma_3}{3} = \frac{\sigma_1 - \sigma_2}{3} + \sigma_2 \qquad\qquad 4\text{-}7$$

increasing. This combination of stress systems will not always exist in tectonic problems. For example, in the strike-slip system considered in Chapter 5 only the pure shear component of stress is increased during stress accumulation.

The effect of these two stress systems on resistivity must be separated. One way is to conduct the experiment so that the increase in σ_1 is equal to the decrease in σ_2. Experiments of this nature have not been made while measuring resistivity, or for that matter, any other rock property. Using existing data it is possible to estimate the effect of pure shear. To do this the resistivity-stress difference data (Figure 4-5) is replotted on the resistivity-confining stress plot (Figure 4-3) at the appropriate average stress. The data are renormalized so that the point $\sigma_1 - \sigma_2 = 0$ lies on the original resistivity-confining stress plot (Figure 4-7). The difference of the confining stress data, and the triaxial data represents the effect of pure shear. Figure 4-8 shows the expected normalized resistivity in the maximum principal stress direction for pure shear. Notice the difference in this plot from that of Figure 4-6. The resistivity is expected
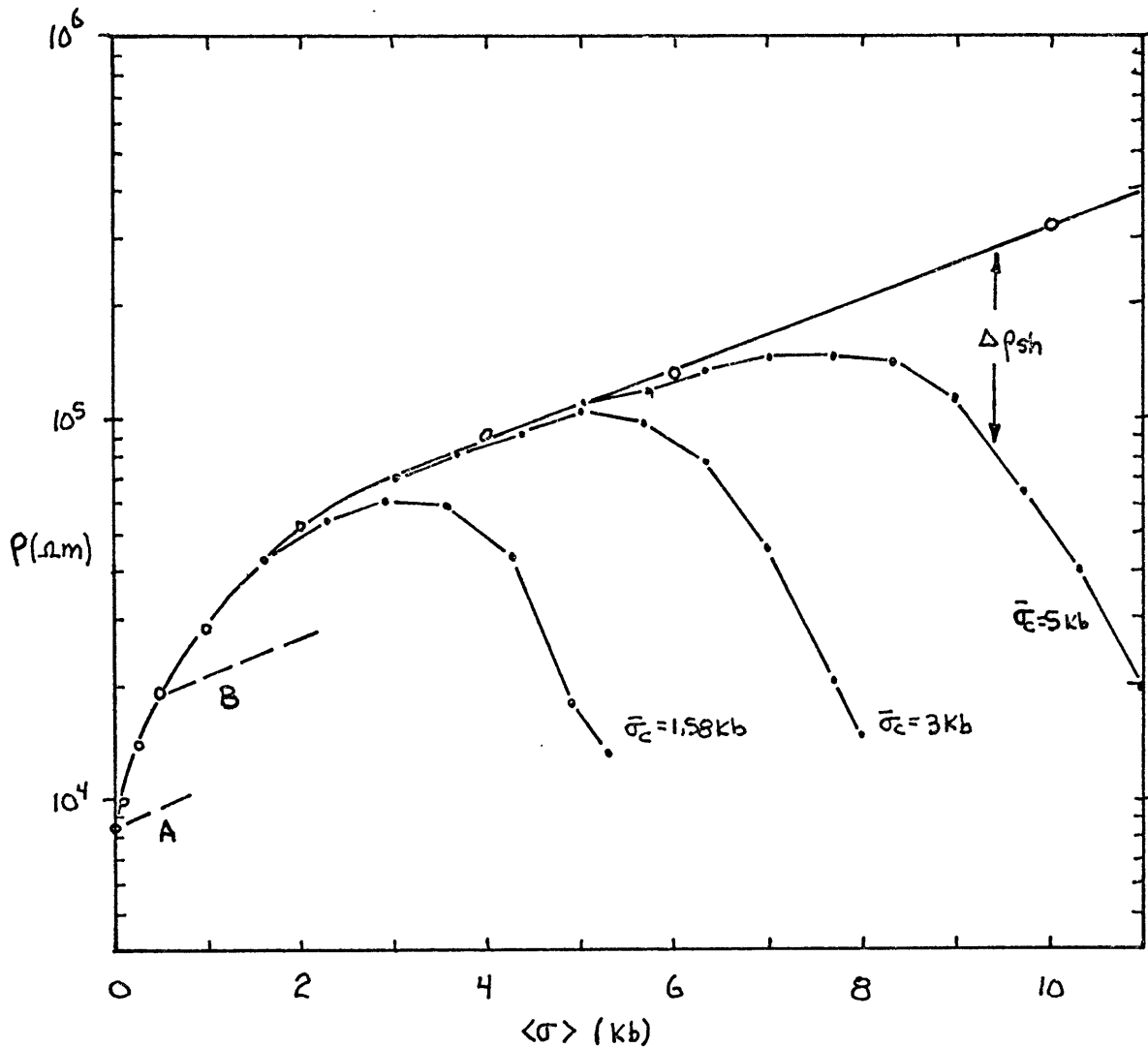
FIGURE 4-7   RESISTIVITY OF WESTERLY GRANITE IN MAXIMUM STRESS
DIRECTION AS A FUNCTION OF $\langle\sigma\rangle$ FOR
ISOTROPIC (o) AND TRIAXIAL LOADING

LINES A & B ARE EXPECTED BEHAVIOR AT LOW
CONFINING STRESS.
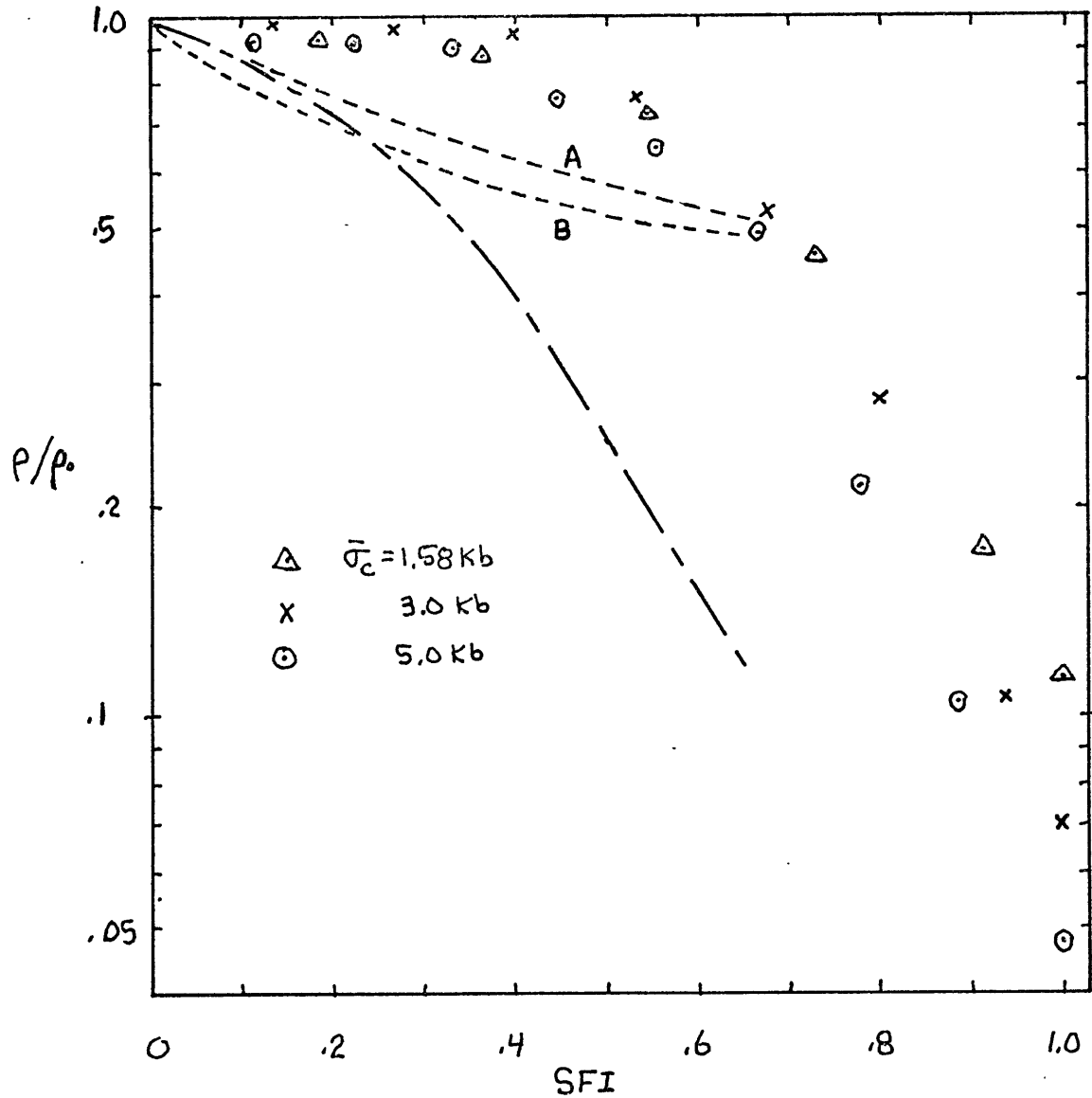
$\Delta\rho_{sh}$ EFFECT OF PURE SHEAR ON RESISTIVITY

FIGURE 4-8 NORMALIZED RESISTIVITY OF WESTERLY GRANITE
IN MAXIMUM STRESS DIRECTION FOR PURE SHEAR

--- EXPECTED BEHAVIOR AT LOW $\bar{\sigma_c}$

--- EXPECTED BEHAVIOR FOR CYCLED ROCK

to decrease under the influence of pure shear when measured parallel to the direction of maximum stress.

This expected resistivity behavior can be explained in terms of the effect of stress on cracks. The cracks in rock tend to be rather long and flat (Brace et al., 1972). Stresses oriented perpendicular to the cracks close them, while loading in the direction of the cracks will pop them open. Pure shear will open cracks oriented in the direction of maximum stress, while closing those parallel to the minimum stress direction. The result will be an increase of conductivity in the direction of maximum stress.

The experiments considered in this section were run at confining stresses equivalent to depths of 10 km or more. A resistivity monitor set up in an active tectonic region for the purpose of earthquake prediction would probably sample the electrical properties of material at lower effective confining stresses, i.e., the upper 5 km or less. Only speculations about how rock resistivity will behave under near surface conditions can be made.

It is known that most cracks will be open at effective stresses of less than 1 kb (Brace et al., 1965). Furthermore, the cracks are "soft" compared to the mineral grains and are greatly influenced by stress (Walsh, 1965). Referring to Figure 4-7 we see that for high confining stresses, the triaxial curves leave the confining stress curve at about the same angle. Due to the flexibility of the cracks at low $\bar{\sigma}_c$,

it is suggested that the resistivity for low confining stress triaxial tests will behave as shown by the dotted lines. This effect is not due to dilatancy. At higher shear levels the curves will begin to curve downward as dilatancy becomes important. The behavior of the low confining stress points on the normalized behavior plot (Figure 4-8) are shown as lines A and B. At a SFI $\sim$.65 they run into the normalized behavior of the higher confining stress results. This postulated normalized behavior for rocks under low confining stress and small SFI will be used in the next chapter.

4.6   Field Conditions

The data discussed above were for rather idealized laboratory experiments which might differ significantly from field conditions. In situ rock may dilate faster than water can flow into it leaving the material partially saturated. One might expect this would keep the newly formed porosity from contributing to conduction. However, rocks which are not completely saturated as they dilate tend to behave the same as the saturated rocks in Figure 4-6 do (Brace, 1974). The explanation is that the new cracks are smaller than most of the old ones making the surface conduction contribution significant. Tests by Madden et al. (1974) also showed that mechanical stressing increased the surface conductivity contribution meaning that the newly formed cracks are narrower on the average than existing cracks (Figure 4-9). On the
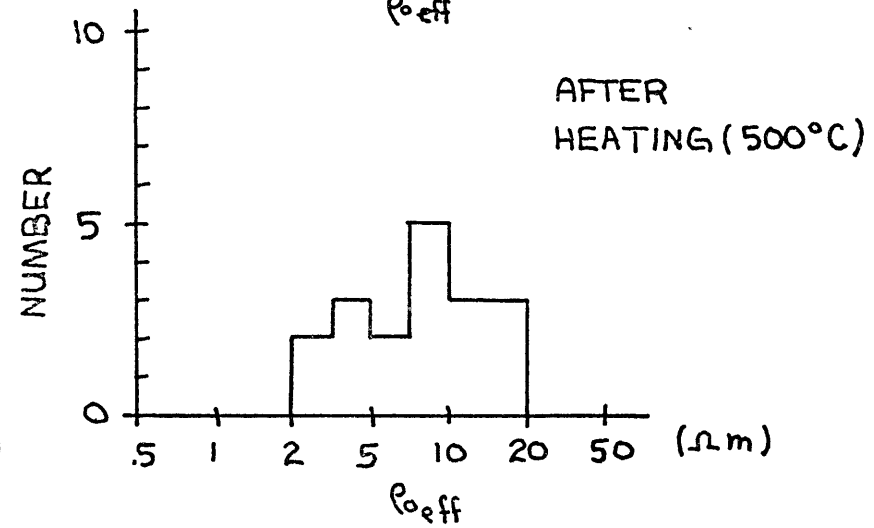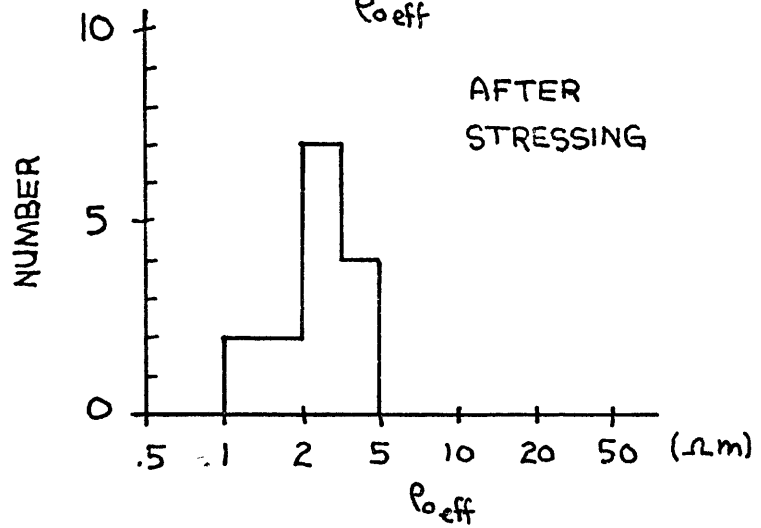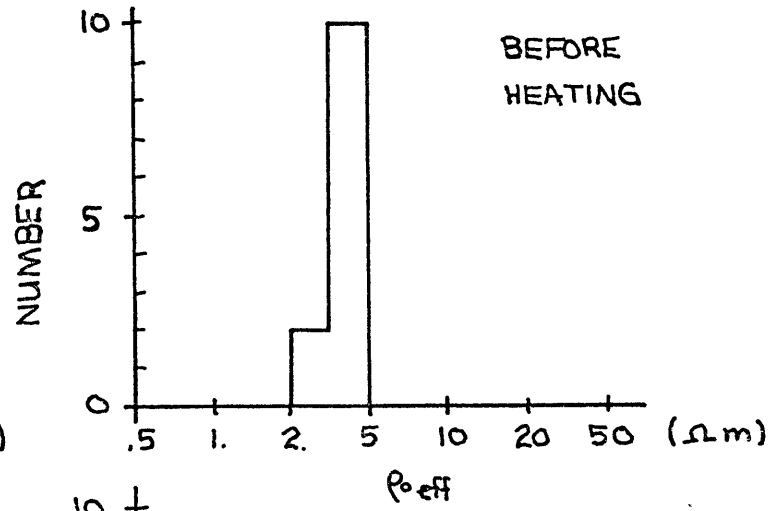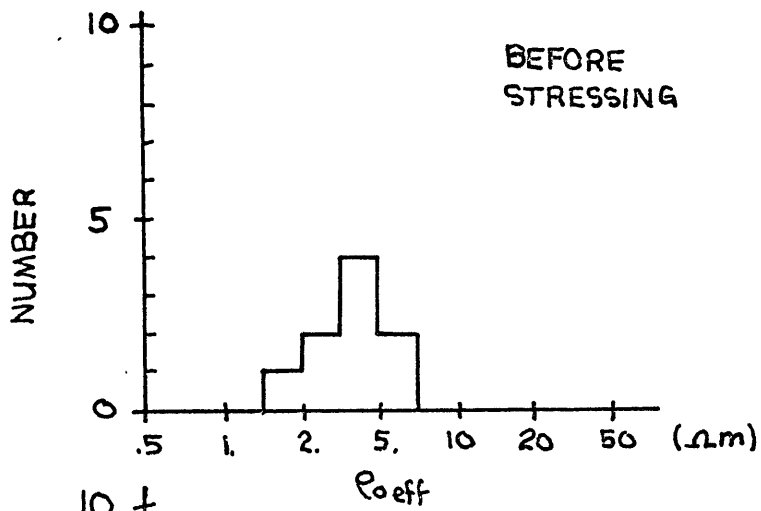
FIGURE 4-9 $\rho_{o\,eff}$ OF CHELMSFORD GRANITE BEFORE AND AFTER STRESSING AND HEATING PORE FLUID TAP WATER ($\sim$ 50 Ωm) (MADDEN ET AL. 1974)

$\rho_{o\,eff}$ = $1/\sigma_{o\,eff}$ DEFINED IN EQ. 4-3

other hand, cracks formed by thermal stressing tend to de-
crease the importance of surface conductivity suggesting the
new cracks are larger than most of the original ones.

The most significant difference between laboratory and
field measurements will be in the stress history of the rocks.
Repeated accumulation and release of stress will change the
dilatant behavior of the rock. Cyclical loading of rocks to
within 90% of failure stress resulted in volumetric strain-
stress diagrams like the one shown in Figure 4-10 (Scholz and
Kranz, 1974). Volumetric strain was found to increase with
each loading cycle, with some volumetric strain being non-
recoverable. More importantly, the point where dilatancy
started (C') was lowered to 15% of the failure stress. This
might provide a mechanism for rather large zones becoming
dilatant. It is anticipated that the resistivity of cycled
rock increases as the stress difference is increased to C'
because pore volume is decreasing. As the rock starts dila-
ting, the resistivity decreases due to the opening of previ-
ously formed cracks which draw in water by capillary action.
The anticipated normalized behavior is shown in Figure 4-11.
It is assumed to have the same shape as the virgin rock curve
after it becomes dilatant, but this behavior starts at a
lower stress level. Recent measurements by Brace (1974) con-
firm this type of behavior.

Just like the virgin rock triaxial tests the effect of
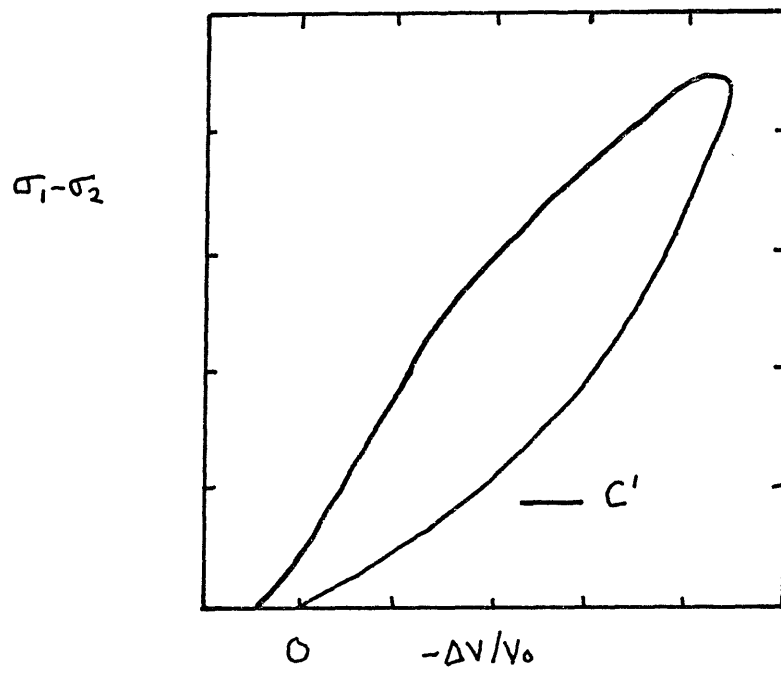increased confining stress must be separated from the effect

FIGURE 4-10 $\sigma_1-\sigma_2$ VS. $-\Delta V/V_0$ FOR CYCLED ROCK, SCHEMATIC DIAGRAM
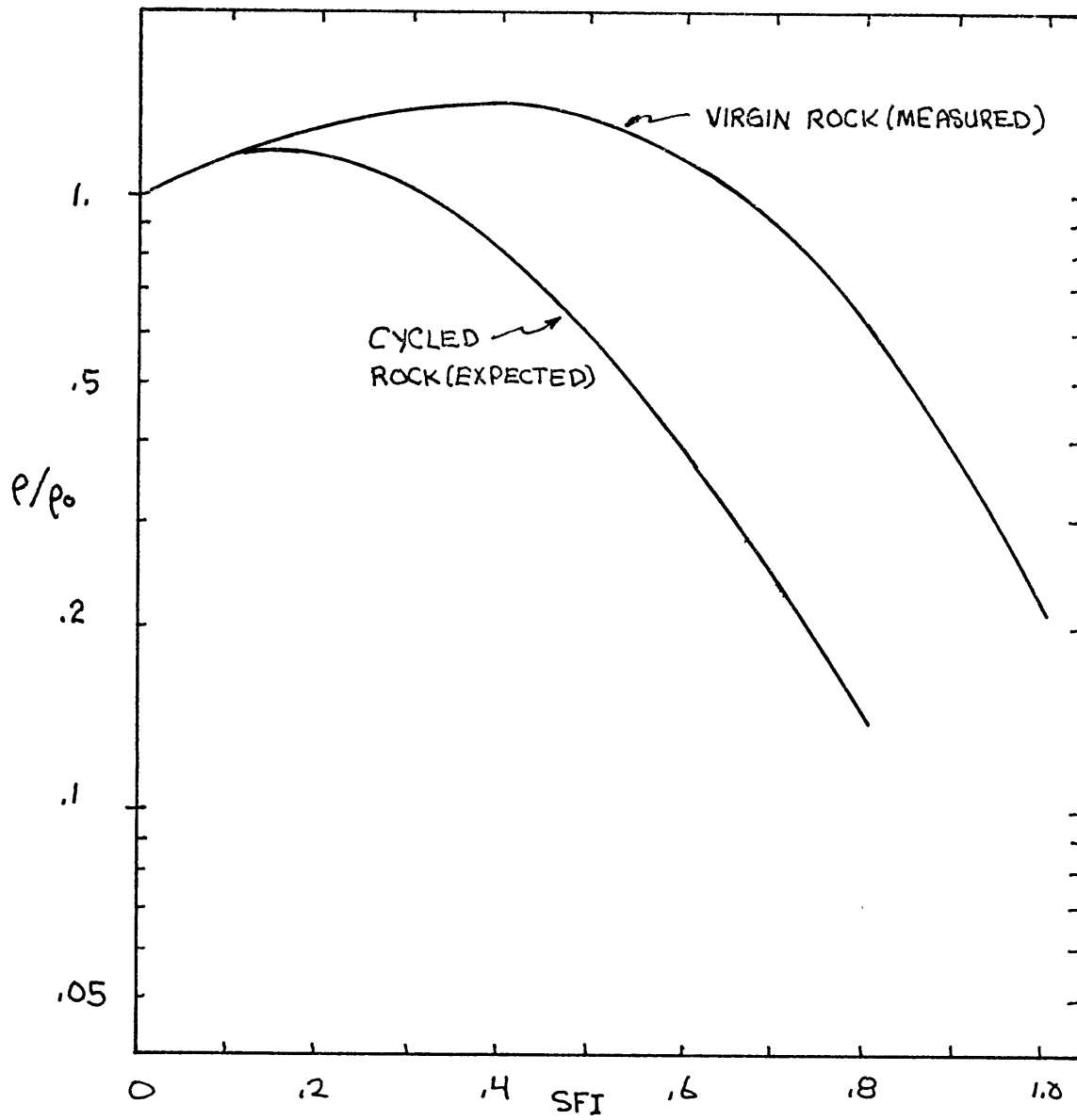
FIGURE 4-11 EXPECTED NORMALIZED RESISTIVITY

BEHAVIOR FOR CYCLED ROCK

of pure shear. This was estimated by taking the normalized
behavior for virgin rock in Figure 4-8 and moving it horizon-
tally so that the points at SFI = .50 are now at SFI = .15.
The curve was then moved vertically so that it went through
the point for no stress difference. Admittedly this approach
is very heuristic. In light of the fact that no experimental
data exists, it is the best that can be done. The idea is sup-
ported by the fact that the crack porosity of the cycled rock
is substantially greater than that of the original rock. This
will make the rock resistivity more susceptible to applied
stresses. As pointed out before, the curves in Figure 4-8
show the resistivity decrease expected in the maximum stress
direction. The resistivities in the perpendicular direction
are expected to increase in a similar fashion until most of
the crack porosity is closed. The effect of the increased
vertical conductivity will then take over and decrease the
horizontal conductivity.

4.7 Summary

The electrical properties of intact rock are rather well
known, and vastly different from those of clay. Rock resis-
tivity at near surface temperatures is controlled primarily
by crack distribution. The effect of a particular stress
system on resistivity can be explained in terms of the opening
and closing of cracks. Cracks oriented perpendicular to the
direction of maximum principal stress are closed while those

parallel to the maximum stress direction open. This causes
an enhancement of electical conductivity in the maximum stress
direction.

No measurements to date have been made which apply only
pure shear to the specimen. By combining the results of con-
fining stress and triaxial loading experiments estimates of
the effect of pure shear were obtained. Resistivity in the
maximum stress direction is seen to decrease before dilatan-
cy becomes important. This fact is obscured by the way past
experiments were run. It is suggested that future experiments
be run with pure shear loading of the rock, and that the
resistivity be measured in orthogonal directions.

Cyclically loaded rocks have been found to dilate at
15% of failure stress. These findings were used to estimate
the resistivity of rocks in tectonically stressed areas. Re-
sistivity at low confining stress is expected to decrease sub-
stantially in the maximum stress direction due to pure shear.
The resistivity in the minimum stress direction is expected
to increase at first, and later decrease as the rock becomes
dilatant.

CHAPTER 5:   THEORETICAL ANALYSIS OF RESISTIVITY VARIATIONS

AROUND A STRIKE-SLIP FAULT

5.1 Introduction

The possibility of using resistivity measurements to

detect stress build-up prior to an earthquake is suggested

by the dilatancy-diffusion earthquake model (Scholz et al.,

1973). Some investigators (Sadovsky et al., 1972; Mazzella

and Morrison, 1974) claim to have seen large variations in

resistivity prior to earthquakes. While the data are not

totally convincing, the likelihood of such a method working

should be explored.

The dilatancy-diffusion earthquake model predicts that

a dilatant zone forms in the hypocentral region prior to an

earthquake (Nur, 1972; Scholz et al., 1973). Since the

physical properties of rock are greatly altered by dilatancy,

it is hypothesized that measurable quantities such as seismic

travel times and electrical resistivity will be altered over

a large enough region that the change can be seen by surface

observations. Numerous investigators have tried to explain

pre-seismic travel time anomalies without determining if a

dilatant zone large enough to cause the anomaly could have

been formed by a reasonable stress system (Nur, 1972; Scholz

et al., 1973; Aggarwal et al., 1973; Whitcomb et al., 1973;

Wyss and Holcomb, 1973).

In this chapter a simple strike-slip fault model will

be used to examine the extent of the dilatant zone, and the

magnitude of resistivity variations it produces.   In
particular, the San Andreas fault of California will be
considered.

5.2   The Tectonic Model

Hypocenter locations in California give some interesting
information about the San Andreas fault.   Hypocenters of most
earthquakes are confined to the upper 15 km of crust with
peak activity around 7-10 km (Wesson et al., 1973; Bolt and
Miller, 1971).   Since earthquakes do not occur in the lower
portions of the crust, it means strain is not accumulating
there.   This is explained by allowing the lower portions of
the Pacific and North American plates to slide past each
other while keeping the upper portion locked.   A large
earthquake occurs when the upper portion of the fault moves.

This simple model can be approximated by a screw
dislocation in a half-space.   The displacement function for
a single screw dislocation is given by

$$U_y(x,z) = \frac{b}{2\pi} \tan^{-1} \frac{x}{z}$$

5-1

where z is the downward direction, x the distance from the
fault, and b the relative displacement of the two sides of
the fault (Weertman and Weertman, 1969).   The displacement
field produces two components of stress, namely

$$Y_x = \frac{Gb}{2\pi} \frac{-z}{x^2 + z^2} \qquad\qquad 5\text{-}2$$

and

$$Y_z = \frac{Gb}{2\pi} \frac{x}{x^2 + z^2} \qquad\qquad 5\text{-}3$$

where G is the shear modulus. The dislocation can be buried
at a depth d by replacing z by z-d. In order to satisfy the
boundary condition of no stress on a free surface and
$u_y(x=0) = 0$ it is necessary to put an image dislocation above
the half-space. The resulting displacement and stress fields
are

$$u_y = \frac{b}{2\pi}\left[\tan^{-1}\frac{x}{d-z} + \tan^{-1}\frac{x}{z+d}\right] \qquad 5\text{-}4$$

$$Y_x = \frac{Gb}{2\pi}\left[\frac{d-z}{(d-z)^2 + x^2} + \frac{z+d}{(z+d)^2 + x^2}\right] \qquad 5\text{-}5$$

$$Y_z = \frac{Gb}{2\pi}\left[\frac{x}{(d-z)^2 + x^2} - \frac{x}{(z+d)^2 + x^2}\right] \qquad 5\text{-}6$$

This solution has a stress singularity at z=d as will any
discrete dislocation. To treat the problem properly would
require a plastic solution in the vicinity of the crack tip.
The elastic solution is valid provided one ignores the

unrealizable high stresses around the singularity.

To see how large the dilatant zone is, we next calculate the shear failure index (SFI), the ratio of maximum shear stress to the shear stress at failure. In Figure 5-1 are shown the shear stress at failure as a function of confining stress for Westerly granite. The data are fitted quite well by a curve of the form

$$\tau_f = C_0 + C_1 \sqrt{\overline{\sigma}_c}$$

<div align="right">5-7</div>

where C_0 is the cohesion, C_1 a constant, and $\overline{\sigma}_c = \sigma_c - P$, the effective confining stress. For the data shown, $C_0 \approx 1$ kb, and C_1 is 3.6 kb . For weak rock, such as would be found in active tectonic regions, C_0 can be as low as 100 bars (Farmer, 1968). Assuming hydrostatic pore pressure, the effective confining stress is given by

$$\overline{\sigma}_c = (\rho_{rock} - \rho_{water}) g z$$

<div align="right">5-8</div>

where the ρ's are densities, g the gravitational acceleration, and z the depth.

For the loading system in Equations 5-5 and 5-6, the principal stresses are

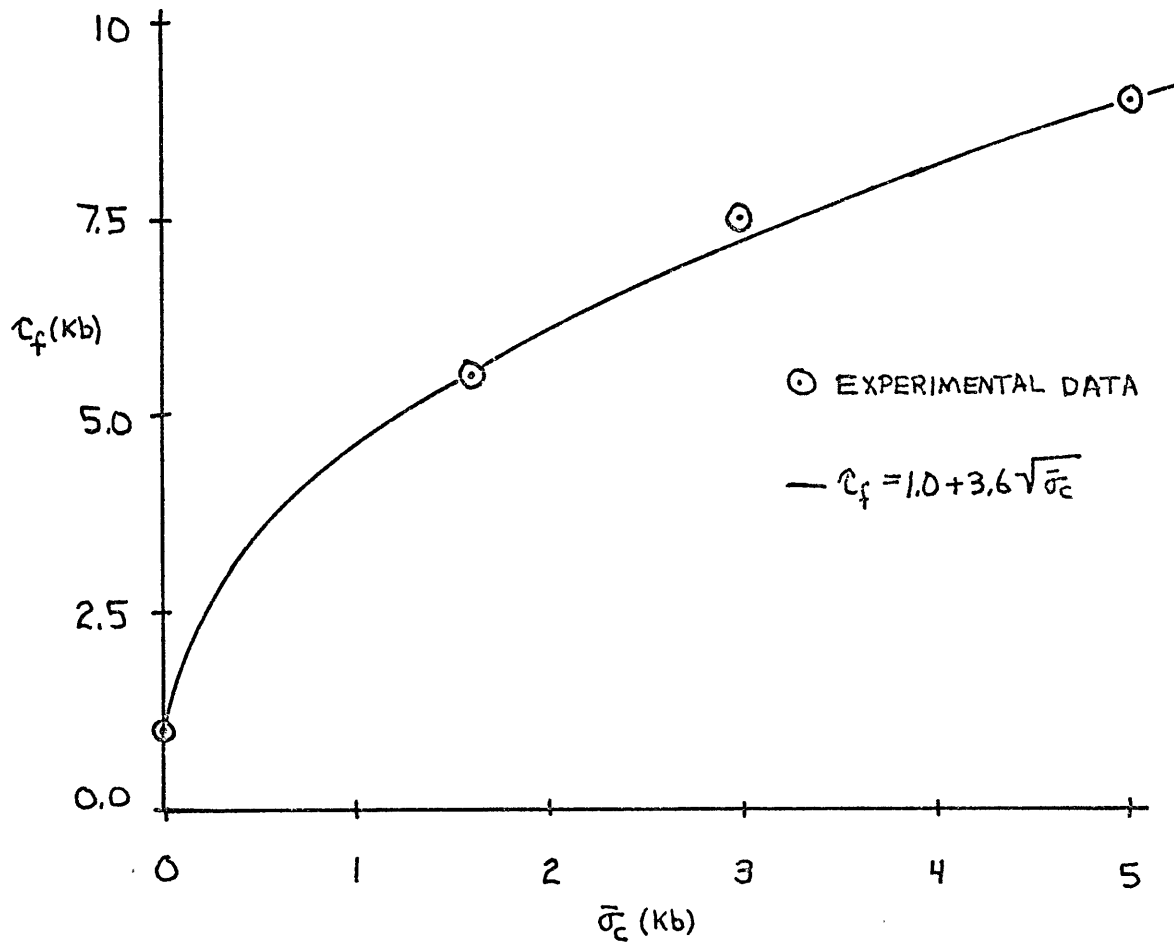$$X_{x'} = \sqrt{Y_x^2 + Y_z^2} = S$$

<div align="right">5-9a</div>

FIGURE 5-1 FAILURE ENVELOPE OF WESTERLY GRANITE
(BRACE AND ORANGE , 1968 A)

$$Y_{y'} = -\sqrt{Y_x^2 + Y_z^2} = -S \qquad\qquad \text{5-9b}$$

$$Z_{z'} = 0 \qquad\qquad \text{5-9c}$$

and the coordinates of the principal stresses in terms of the x, y, z system are

$$\hat{x}' = \frac{\sqrt{2}}{2}\frac{Y_x}{S}\hat{x} + \frac{\sqrt{2}}{2}\hat{y} + \frac{\sqrt{2}}{2}\frac{Y_z}{S}\hat{z} \qquad\qquad \text{5-10a}$$

$$\hat{y}' = \frac{\sqrt{2}}{2}\frac{Y_x}{S}\hat{x} - \frac{\sqrt{2}}{2}\hat{y} + \frac{\sqrt{2}}{2}\frac{Y_z}{S}\hat{z} \qquad\qquad \text{5-10b}$$

$$\hat{z}' = \frac{-Y_z}{S}\hat{x} \qquad\qquad + \frac{Y_x}{S}\hat{z} \qquad\qquad \text{5-10c}$$

or

$$x'_i = a_{ij}\,x_j \qquad\qquad \text{5-11}$$

Maps of the maximum shear stress, τ_{max}, and SFI in the plane perpendicular to strike (x-z) are shown in Figure 5-2

X

τmax (bars)

Z \ X	1	2	3	4	5
1	320	315	308	299	289
2	322	318	311	302	290
3	327	325	315	305	293
4	337	332	324	313	300
5	358	352	341	328	313

X

SFI

Z \ X	1	2	3	4	5
1	.280	.276	.270	.262	.253
2	.169	.167	.163	.158	.153
3	.139	.137	.134	.130	.125
4	.118	.116	.113	.110	.105
5	.106	.104	.101	.097	.092

$DISP = 7550 cm \qquad C_0 = 100b$

$G = 0.2 Mb$

FIGURE 5-2   MAXIMUM STRESS AND SFI PERPENDICULAR TO STRIKE
OF FAULT   FAULT LOCKED TO 15KM   DISTANCES IN KM

for a fault locked to a depth of 15 km with G = 0.2 mb, C_0 = 0.1 kb, and a displacement of 75 m. The maximum shear stress decreases as the distance from the tip of the crack increases. SFI decreases as the horizontal distance from the fault is increased. Points nearer the surface have a higher SFI than those farther away because τ_f decreases more rapidly than τ_{max} as the surface is approached. As the tip of the crack (z = 15 km) is approached (not shown in Figure 5-2) the SFI increases.

Since the stress system used is a linear function of displacement, it is easy to scale the results to other displacements. The actual starting displacement from which conductivity changes will be measured will depend on the state of stress in the ground. There are several ways of obtaining estimates of the state of stress around the San Andreas fault. The first estimate is based on heat flow measurements (Brune et al., 1969; Lachenbruch and Sass, 1973). The absence of a heat flow anomaly greater than $\sim$0.3 $\mu cal/cm^2/sec$ associated with the San Andreas gives estimates of shear stress from 100-400 bars depending what portion of the average shear stress on the fault goes into heat generation, and the slip rate assumed. Estimates based on laboratory friction experiments on rocks at elevated temperatures and pressures are much higher estimates in the range of 750-2000 bars (Stesky and Brace, 1973). These higher stress values should

produce a rather substantial heat flow anomaly, but it has

not been observed. The stress estimates of Stesky and Brace

could be lowered if pore pressures along the fault were higher

than hydrostatic. Also, if the fault zone is extensively

fractured fluid motion away from the fault would spread the

heat source making the magnitude of the heat flow anomaly

much smaller, but covering a much wider zone.

Due to the possible diversity of the state of stress

along the fault, calculations of two models were performed,

one with an average stress of about 300 bars and a second

model with a stress level twice as large. The first model

was shown in Figure 5-2. Assuming dilatancy to begin at

SFI = 0.15, a dilatant zone extending down to a depth of at

least 1.5 km is seen to exist. Doubling the displacement

extends the dilatant zone to more than 5 km. This is quite

a large dilatant zone, but one must remember that it took

about a hundred meters of fault displacement representing

several thousand years to form. What is of importance is

how much change of resistivity takes place during a small

length of time O(10 years) prior to a large earthquake and

whether or not it is detectable. The same holds true for

other earthquake prediction methods which depend on a change

of physical property produced by a stress change. The model

used here predicts that a large dilatant zone is always in

existence where dilatant means SFI $\geq$ 0.15. Dilatancy implies

only that the rock has more cracks in it than when it was formed.

5.3 The Effect on the Conductivity

As was discussed in Chapter 4, the conductivity of rock will depend on the state of stress in the rock. The resistivity of rock is expected to behave as shown in Figure 5-3 during pure shear loading. The resistivity in the maximum stress direction will decrease slowly at first due to opening of cracks parallel to the direction of minimum stress, while the resistivity in the orthogonal direction increases because of crack closure. As the rock becomes dilatant (SFI ∿15%) the resistivity starts to decrease more rapidly in the maximum stress direction as the cracks expand. The resistivity in the minimum stress direction also begins decreasing as less cracks are available to be closed and the increased conductivity in the maximum stress direction contributes to overall lowering of conductivity. This behavior will be used to compute changes in conductivity due to tectonic motion along the fault.

Let the conductivity at some initial stress state be given by the isotropic conductivity tensor σ_{ij}, and the conductivity of the stressed material be σ'_{ij}.

$$\sigma'_{ij} = \begin{bmatrix} \sigma'_{x'} & 0 & 0 \\ 0 & \sigma'_{y'} & 0 \\ 0 & 0 & \sigma'_{z'} \end{bmatrix} = \begin{bmatrix} \sigma_{x'} + \Delta\sigma_{x'} & 0 & 0 \\ 0 & \sigma_{y'} + \Delta\sigma_{y'} & 0 \\ 0 & 0 & \sigma_{z'} \end{bmatrix} \quad \text{5-12}$$
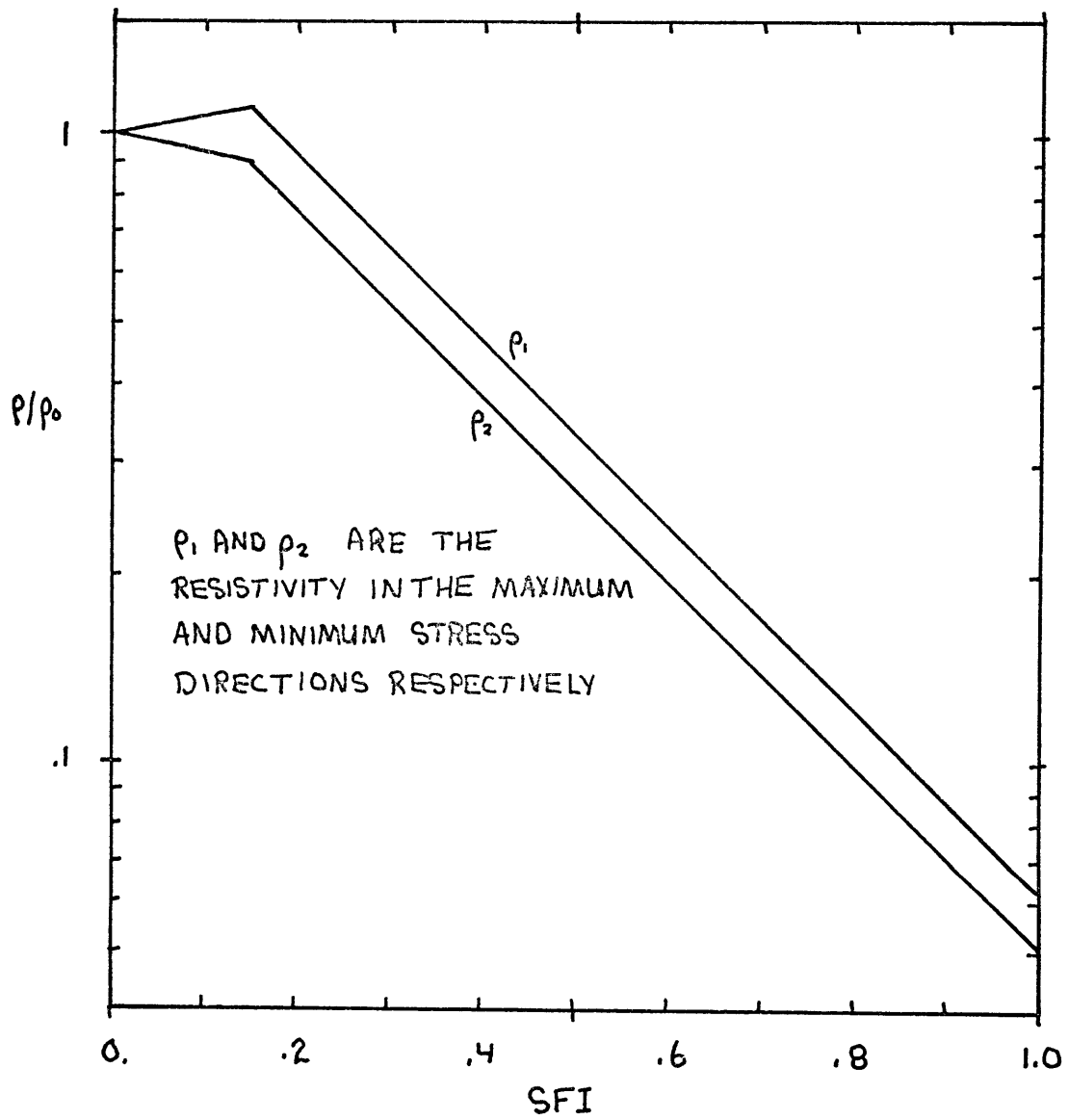
FIGURE 5-3   NORMALIZED RESISTIVITY BEHAVIOR
DURING PURE SHEAR LOADING

where $\Delta\sigma_x$, and $\Delta\sigma_y$, are the changes in conductivity produced by the stress field, and (x', y', z') are the principal directions of the stress field.

The tensor σ'_{ij} is rotated into the (x, y, z) coordinate system using the a_{ij} matrix in Equation 5-11 (Nye, 1969).

$$\sigma_{ij} = a_{ki} \, a_{\ell j} \, \sigma'_{k\ell}$$

5-13

Because the air boundary forces currents to be horizontal (J_z = 0) a simplification can be made. The currents produced by an electric field are given by

$$\begin{bmatrix} J_x \\ J_y \\ J_z \end{bmatrix} = \begin{bmatrix} \sigma_{xx} & \sigma_{xy} & \sigma_{xz} \\ \sigma_{xy} & \sigma_{yy} & \sigma_{yz} \\ \sigma_{xz} & \sigma_{yz} & \sigma_{zz} \end{bmatrix} \begin{bmatrix} E_x \\ E_y \\ E_z \end{bmatrix}$$

5-14

For J_z = 0 the vertical electric field can be expressed in terms of the horizontal fields

$$E_z = -\frac{\sigma_{xz}}{\sigma_{zz}} E_x - \frac{\sigma_{yz}}{\sigma_{zz}} E_y$$
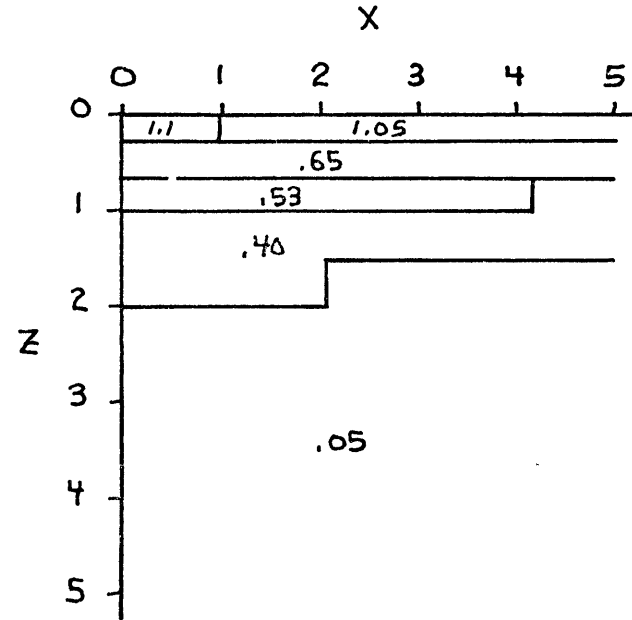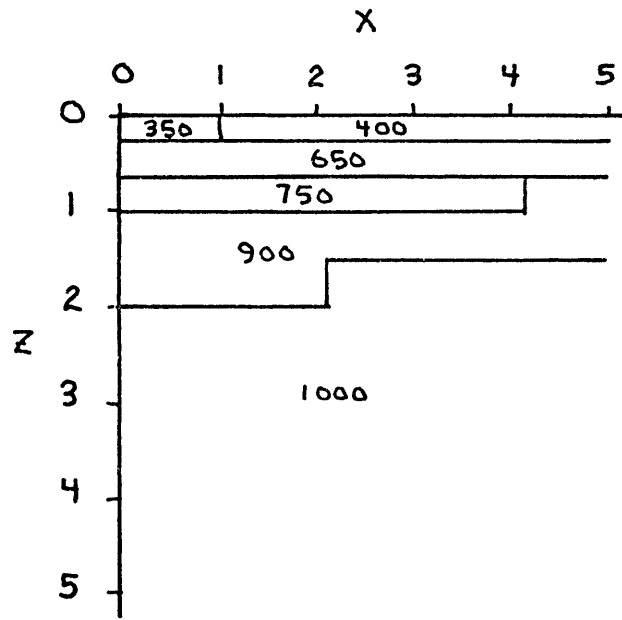
5-15

The new 2-D conductivity tensor, $\tilde{\sigma}_{ij}$, becomes

$$\tilde{\sigma}_{ij} = \begin{bmatrix} \sigma_{xx} - \dfrac{\sigma_{xz}^2}{\sigma_{zz}} & \sigma_{xy} - \dfrac{\sigma_{xz}\sigma_{yz}}{\sigma_{zz}} \\ \sigma_{xy} - \dfrac{\sigma_{xz}\sigma_{yz}}{\sigma_{zz}} & \sigma_{yy} - \dfrac{\sigma_{yz}^2}{\sigma_{zz}} \end{bmatrix}$$

5-16

which can be rotated into its horizontal principal coordinates $(\tilde{x}, \tilde{y})$ by using Mohr's circle (Nye, 1969).

When SFI $\geq$ 0.15, changes in the conductivity tensor are isotropic. For points where SFI < 0.15, the conductivity changes were anisotropic $(\Delta\tilde{\sigma}_{x'} = -\Delta\tilde{\sigma}_{y'})$ with the principal conductivity directions oriented at 45° to the fault coordinate system. For the case shown in Figure 5-2, the anisotropic changes were deeper than 2 km and at least an order of magnitude smaller than the isotropic changes nearer the surface. For these reasons the anisotropic changes were not considered in calculating surface variations. In the second case, where the stress level is twice as high, all conductivity changes were isotropic. In Figures 5-4 and 5-5 are shown the calculated conductivity changes for a 50 cm incremental fault displacement. Also shown are the resistivities based upon an average of the maximum and minimum stress direction resistivities (Figure 5-3). Unstressed resistivity (ρ_0) was taken as 1000 Ω m.

The conductivity variations for a 50 cm incremental displacement are rather small O(1%) and diminish to half that value at a depth of about 1 km. Variations decrease with increasing distance from the fault, but not as quickly as with depth. Because the maximum conductivity changes are in the near surface, they should be efficiently detected by surface resistivity measurements.

Left diagram axis labels: X (top), O 1 2 3 4 5; vertical axis Z: O 1 2 3 4 5; O at origin.

Values in left diagram: 350, 400, 650, 750, 900, 1000

Right diagram axis labels: X (top), O 1 2 3 4 5; vertical axis Z: O 1 2 3 4 5; O at origin.

Values in right diagram: 1.1, 1.05, .65, .53, .40, .05

RESISTIVITY (Ωm)

$\dfrac{\Delta \sigma}{\sigma}$ (%)

STARTING DISPLACEMENT = 7500 cm

CONDUCTIVITY CHANGES DUE TO 50 cm INCREMENTAL DISPLACEMENT

DISTANCES IN KM

FIGURE 5-4   RESISTIVITY AND VARIATION OF CONDUCTIVITY, $D_0 = 7500$ cm
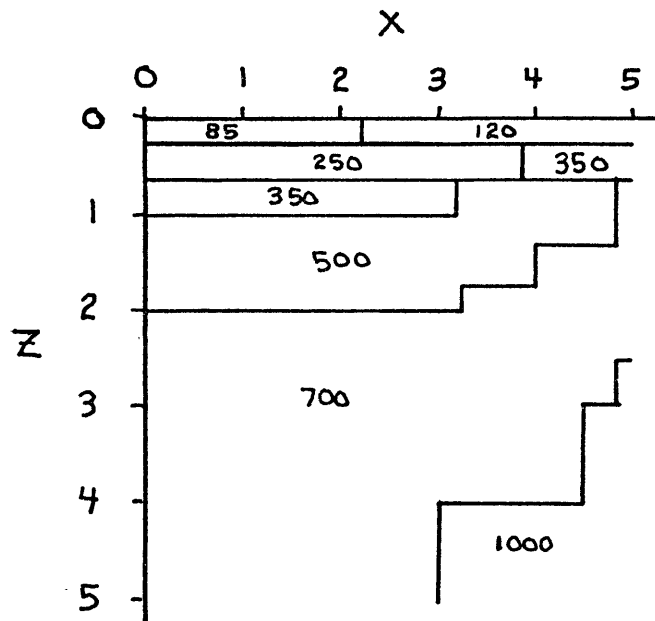
RESISTIVITY (Ωm) $\frac{\Delta\sigma}{\sigma}$ (%)
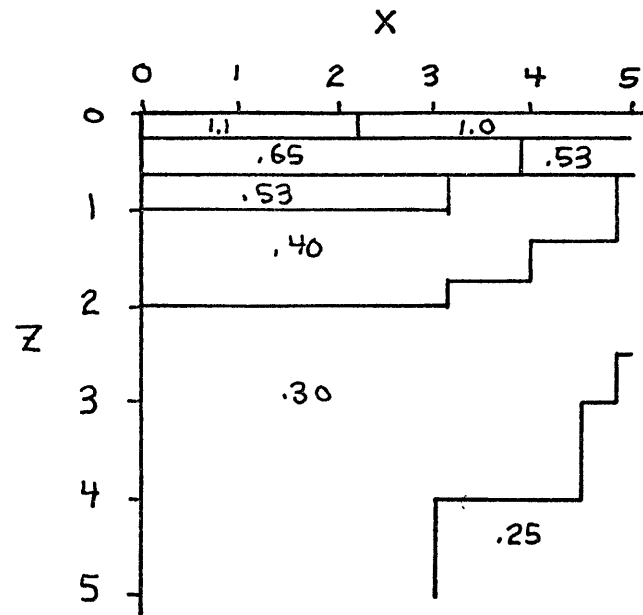
STARTING DISPLACEMENT = 15000cm
CONDUCTIVITY CHANGES DUE TO 50cm INCREMENTAL DISPLACEMENT
DISTANCES IN KM

FIGURE 5-5   RESISTIVITY AND VARIATION OF CONDUCTIVITY, D_0=15000cm

5.4 The Sensitivity of Surface Measurements

It is now necessary to compute the variations in apparent resistivity measured at the surface due to the stress induced resistivity variations at depth. The case of a dipole-dipole resistivity array with 1 km dipoles oriented perpendicular to the strike of the fault will be considered. The data shown in Figures 5-4 and 5-5 were used for the calculations of resistivity and conductivity variation (Figure 5-6 and 5-7). On the cross sections are plotted the apparent resistivity and apparent conductivity change for a particular receiver-transmitter pair. The data are plotted half way between the two locations on 45° sloping lines. Moving down a diagonal represents measurements associated with a particular receiver (transmitter) site as the transmitter (receiver) is moved farther away.

The largest variation is seen directly over the fault as would be expected. Shorter spacings are more sensitive due to the increased change in SFI near the surface. Detectability of these small changes would be difficult. Doubling the incremental displacement to 100 cm would more than double the resistivity variation because of the non-linear resistivity-SFI relationship used. This would put the variation above a practical threshold of several percent. Assuming a relative plate velocity of 2.5 cm/year it would take about 40 years for this variation to be produced. The long term stability of the monitor system would have to be very good to
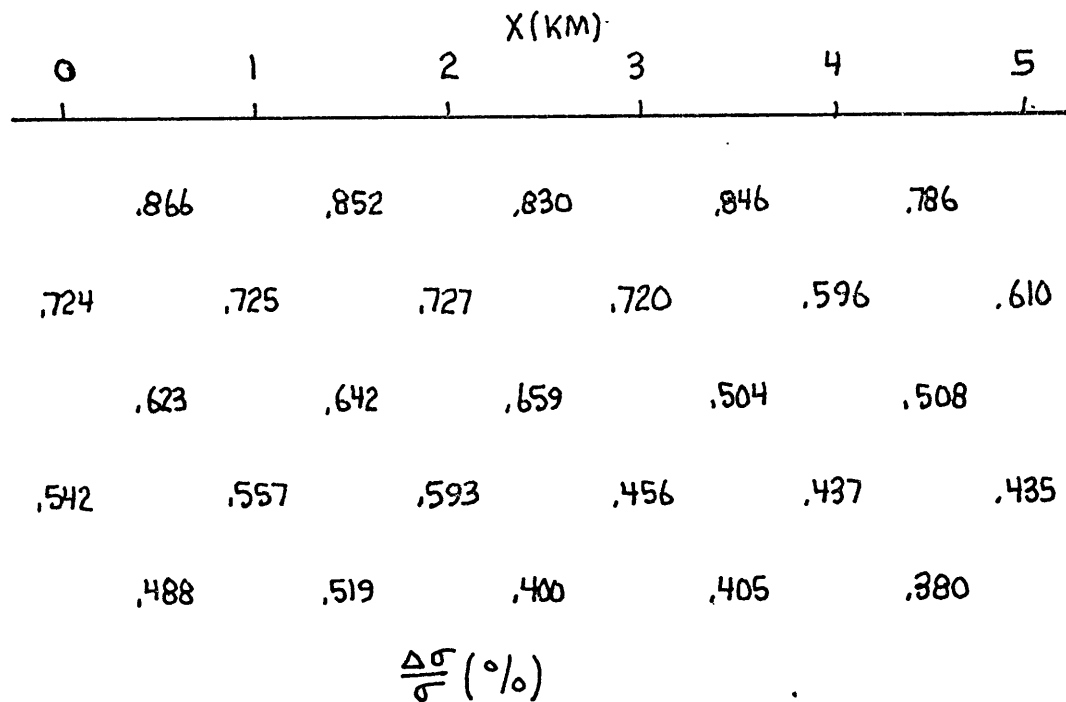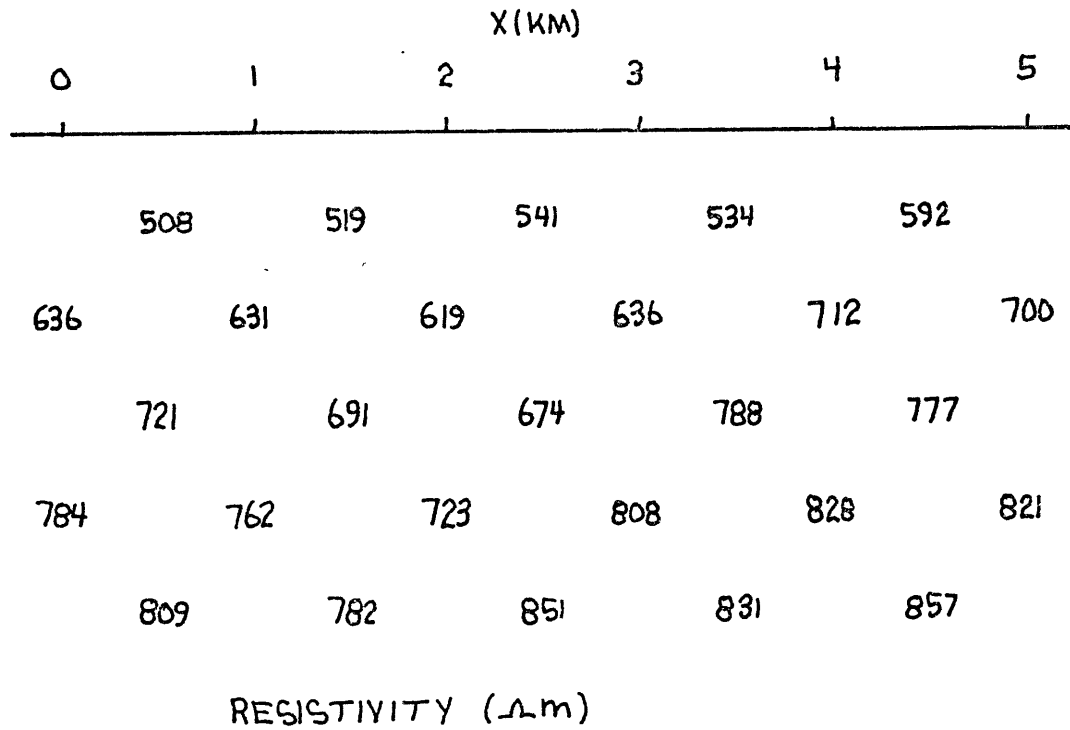
X(KM)

0	1	2	3	4	5

	508	519	541	534	592	
636	631	619	636	712	700
	721	691	674	788	777	
784	762	723	808	828	821
	809	782	851	831	857	

RESISTIVITY (Ωm)

X(KM)

0	1	2	3	4	5

	.866	.852	.830	.846	.786	
.724	.725	.727	.720	.596	.610
	.623	.642	.659	.504	.508	
.542	.557	.593	.456	.437	.435
	.488	.519	.400	.405	.380	

$\frac{\Delta\sigma}{\sigma}$ (%)

FIGURE 5-6 RESISTIVITY AND CONDUCTIVITY CHANGE CROSS-SECTIONS DUE TO 50cm INCREMENTAL DISPLACEMENT, D_0=7500cm, DIPOLE LENGTH = 1 KM

X (KM)

0	1	2	3	4	5
	148	156	165	200	213
199	216	230	234	276	298
	256	278	289	288	338
314	310	331	336	334	390
	370	357	372	377	374

RESISTIVITY (Ωm)

X (KM)

0	1	2	3	4	5
	.945	.921	.891	.826	.818
.874	.835	.803	.796	.782	.722
	.790	.750	.740	.737	.673
.710	.718	.702	.697	.695	.629
	.644	.679	.667	.662	.660

$\frac{\Delta\sigma}{\sigma}$ (%)
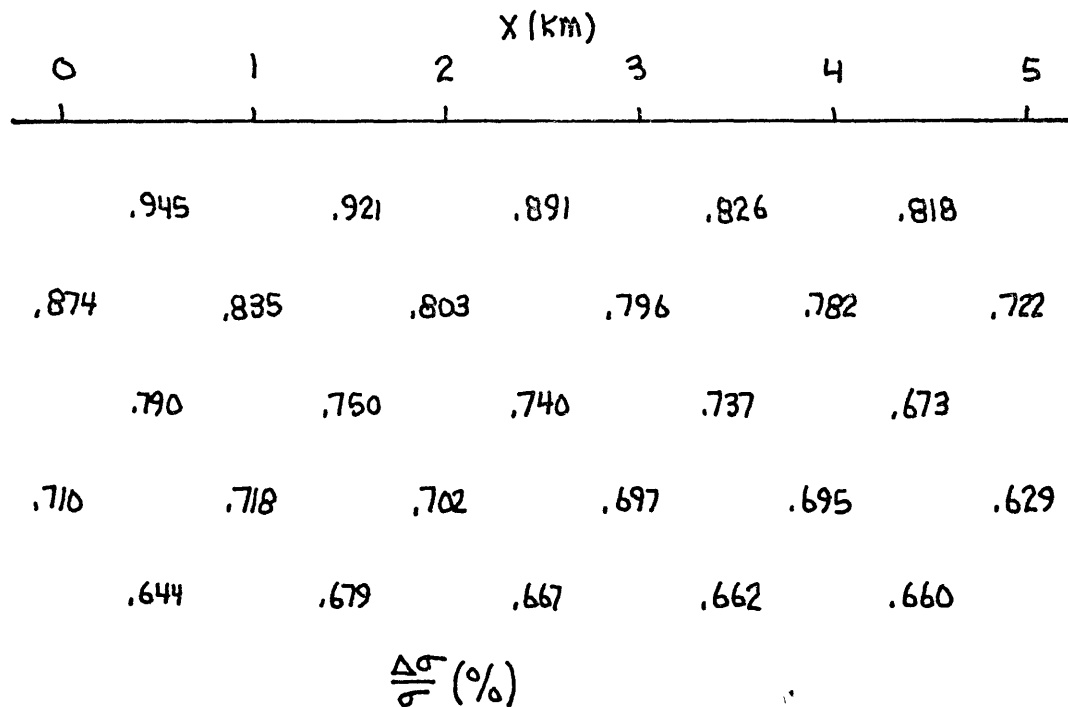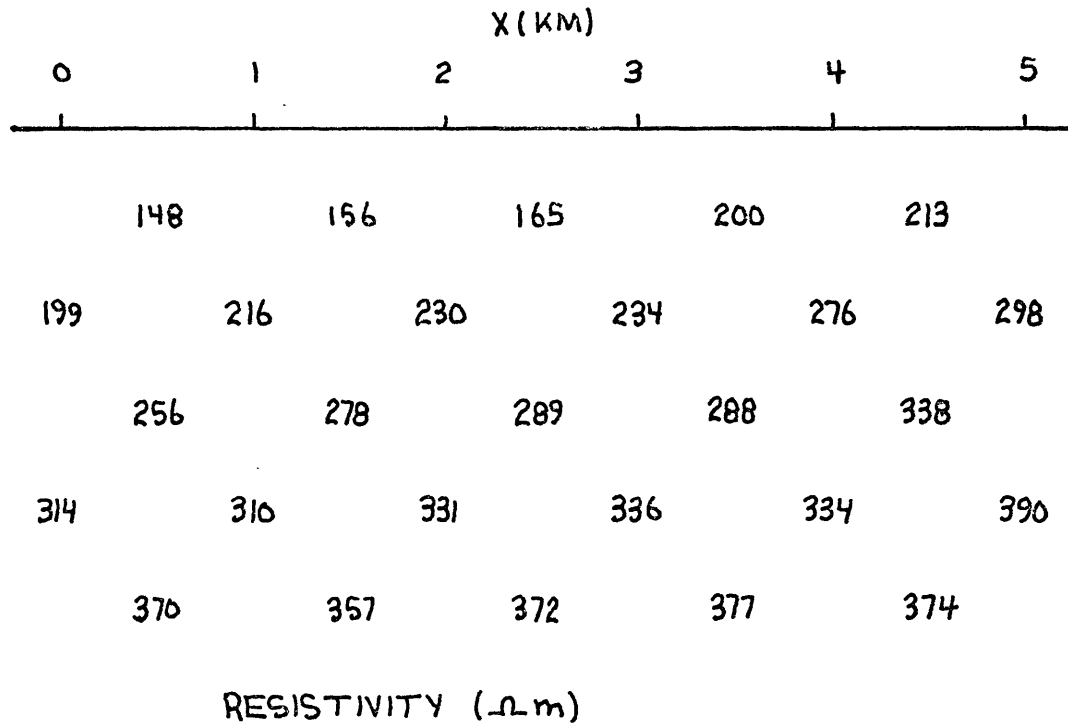
FIGURE 5-7   RESISTIVITY AND CONDUCTIVITY CHANGE CROSS SECTIONS DUE TO 50 cm INCREMENTAL DISPLACEMENT, $D_0 = 15000$ cm , DIPOLE LENGTH = 1 KM

detect a variation over this period of time.

The possibility of long term earth resistivity changes not associated with earth strain represents a drift which can not be calibrated out of the measurements. Such drifts might come about for a variety of reasons. Long term climatological variations could produce temperature changes which would penetrate to very great depths causing resistivity variations. On the large time scale necessary for strain accumulation, underground fluid flows could modify the water table level or change the pore fluid salinity. These effects could change the resistivity and the separation of these variations from tectonically induced ones would be quite difficult.

5.5 The Implications

The model presented here has some strong implications about the prediction of large strike-slip earthquakes by resistivity monitoring as well as any other methods which make use of changes in rock properties due to dilatancy. Taking a commonly used tectonic model and optimistic rock resistivity-SFI behavior, very small resistivity variations are found to be produced by 20 years of relative plate motion. These results cast a shadow on the hope of earthquake prediction.

The small resistivity changes come about because of the

small changes in SFI and shear stress associated with a
given fault displacement. Decreasing the depth to which the
fault is locked will in general result in larger changes in
SFI and shear stress per unit displacement. Hypocenter data
requires that the locked zone not be much shallower than
10 km which would not greatly alter the results. Additionally,
to get stresses up to the level suggested by heat flow and
laboratory data it would be necessary for SFI in the near
surface to exceed unity. The material would then fail and
some stress be relieved. The tendency of the near surface
region to fail before material which is between the surface
and the crack tip comes about because the shear stress decreases
less quickly than the failure shear stress as the surface is
approached. If creep events are a near surface phenomenon,
they could be caused by this instability and actually be
taking place while stress is accumulating at a greater depth.

Mazzella and Morrison (1974) have reported a 24% decrease
in resistivity prior to the Bear Valley earthquake (M=3.9) of
22 June 1973. Resistivity was observed to decrease for a
period of 60 days and return to normal before the earthquake.
This observation is in conflict with the model presented here.
The discrepancy can be explained by several possible arguments.
First the observations might not be reliable. Examples of
similar results for more strike-slip earthquakes would make
the observations more believable. If the variation is real
it is due either to a large zone undergoing a change on the

order of 25%, or a small zone with a much bigger variation.

Mazzella and Morrison estimate that a resistivity change of

80% over a 4 km wide zone extending from a depth of 2 to 6 km

would produce the observed variation. Such a large resistivity

change would require a stress change equivalent to 20% of the

breaking strength (See Figure 5-3). At a depth of 4 km this

represents a stress change of over 100 bars. Such a large

stress change in a 60 day period is not possible with this

model. Resistivity variations of 24% over a large region

(ten's of kilometers on a side) is also hard to obtain from

a dislocation model because the stress field dies off very

quickly (at least as fast as $1/r$, and often as $1/r^2$) as the

distance from the crack tip increases. If the observed

resistivity variation is real, this model can not explain it.

The simple model used is also not free from fault. The

stress system which would produce the assumed displacements

might not the be one found in the earth. If the zone between

the two fault blocks were in a state of uniform shear stress

a much larger zone would experience a change of resistivity.

Local variations of mechanical properties could cause peculiar

stress distributions which could modify the predicted resistivity

variation. For example, if there were a region along the fault

where the rock was weaker than in the neighboring regions, a

stress concentration would result around the ends of the weak

zone. This amplification of stress could cause large resistivity

changes. Interaction of several weak zones could produce an

instability which would allow stress levels to change quickly
with time.

A third possible way of explaining the discrepancy is
that the resistivity-SFI behavior used in the calculations is
not correct. Attempts were made in Chapter 4 to determine the
effect of pure shear loading on resistivity, but it would be
much better to have actual laboratory data measured under the
proper loading conditions. The estimates used in this model
are probably on the optimistic side with rather large changes
in resistivity for a given amount of loading.

Believing in this model one must live with the following
consequences:

1. The most significant changes in resistivity due
   to strain accumulation will be confined to a small
   region close to the surface several kilometers deep.
2. The magnitude of resistivity changes produced on
   the surface will be small and take a rather long time
   to develop. The resistivity changes produced by
   non-tectonic causes must be considered, and these
   variations will be hard to separate from the
   tectonically induced variations.

More field measurements are required to determine if pre-
earthquake resistivity variations really exist for strike-slip
earthquakes. In addition, laboratory measurements of resistivity
under conditions which realistically model the stress system of
interest are necessary.

CONCLUSIONS

Two different tectonic processes, fault creep motion and
strain accumulation, associated with strike-slip faults have
been considered to determine if stress changes associated with
these processes produce significant resistivity variations.
Observations during creep events found no significant resis-
tivity changes associated with fault motion, and calculations
on the effects of strike-slip faults predicted insignificant
time variations of resistivity.

The absence of detectable resistivity variations during
creep events is attributed to the small size of the stress
induced resistivity change and to the narrowness of the zone
undergoing the change during creep motion. The clay environ-
ment of the monitor site can account for the small resistivity
variations required. Triaxial loading of clay to failure was
found to produce small (5-25%) resistivity changes. These
changes are attributed to small reorientations of clay parti-
cles perpendicular to the direction of maximum stress. Meas-
urement of resistivity parallel to the maximum stress direc-
tion detected resistivity increases, while measurement perpen-
dicular to the maximum stress direction detected resistivity
decreases. A conductivity model, which takes into account
clay particle orientation, estimates an average angular re-
orientation of 1° to 10° for triaxial loading with failure
deviator stresses in the range of 1-10 kg/cm^2.

Assuming the clay along the fault trace has been brought

to a steady-state orientation by previous fault motion, very little alignment and small resistivity changes are expected to be produced by subsequent creep motion. If the gouge zone undergoes a 1% resistivity change during a creep event, the width of the zone must be less than 6 m wide. The estimated width is an upper bound set by the noise level of the field resistivity monitoring system.

Resistivity variations due to tectonic motion along a strike-slip fault were computed by combining a commonly used tectonic model and laboratory data on resistivity changes of stressed rock. Very small resistivity variations are predicted to occur with substantial fault displacements. A model of the San Andreas fault requires over 20 years to produce a surface observed resistivity change of 1%. The long time scale and small resistivity changes predicted by this model are in variance with reported resistivity variations prior to strike-slip earthquakes.

Resistivity measurements in clay or clay-like material is rather unlikely to detect variations due to tectonic stress changes. The matter of resistivity measurements in rock detecting stress changes prior to earthquakes is still an open question which can best be resolved by continued field observations. If field observations continue to detect precursory phenomena, then very different models must be used, and the validity of extrapolating laboratory-scale measurements to earth-scale problems must be questioned when trying to explain the observations.

REFERENCES

Abramowitz, M., and I. A. Stegun, Handbook of Mathematical Functions, p. 866, U.S. Department of Commerce, Applied Mathematics Series, 55, U.S. Government Printing Office Washington, D. C., 1968.

Aggarwal, Y. P., L. R. Sykes, J. Armbuster, and M. L. Sbar, Premonitory changes in seismic velocities and prediction of earthquakes, Nature, 241, 101-104, 1973.

Archie, G. E., The electrical resistivity log as an aid in determining some reservoir characteristics, Trans. AIME, 146, 54-61, 1942.

Bolt, B. A. and R. D. Miller, Seismicity of northern and central California 1965-1969, Bull. Seis. Soc. Am., 61, 1831-1847, 1971.

Brace, W. F., Some new measurements of linear compressibility of rocks, J. Geophys. Res., 70, 391-398, 1965.

Brace, W. F., Personal communication, 1974.

Brace, W. F., and A. S. Orange, Electrical resistivity changes in saturated rocks during fracture and frictional sliding, J. Geophys. Res., 73, 1433-1445, 1968a.

Brace, W. F., and A. S. Orange, Further studies of the effects of pressure on electrical resistivity of rocks, J. Geophys. Res., 73, 5407-5420, 1968b.

Brace, W. F., A. S. Orange, and T. R. Madden, The effect of pressure on the electrical resistivity of water-saturated crystalline rocks, J. Geophys. Res., 70, 5669-5678, 1965.

Brace, W. F., B. W. Paulding, and C. Scholz, Dilatancy in the fracture of crystalline rocks, J. Geophys. Res., 71, 3939-3953, 1966.

Brace, W. F., E. Silver, K. Hadley, and C. Goetze, Cracks and pores: a closer look, Science, 178, 162-164, 1972.

Brown, R. D., Jr., Map Showing Recently Active Breaks Along the San Andreas and Related Faults Between the Northern Gabilan Range and Cholame Valley, California, U.S.G.S. Misc. Geol. Investigations, Map I-575, 1970.

Brune, J. N., T. L. Henyey, and R. F. Roy, Heat flow, stress, and rate of slip along the San Andreas fault, California, J. Geophys. Res., 74, 3821-3827, 1969.

Burford, R. O., Personal communication, U.S.G.S.-NCER, Menlo Park, California, 1974.

Cotton, L. A., Earthquake frequency, with special reference to tidal stresses in the lithosphere, Bull. Seis. Soc. Am., 12, 49-53, 1923.

Diamond, Sidney, Pore size distributions in clays, Clays and Clay Minerals, 18, 7-23, 1970.

Diamond, Sidney, Microstructure and pore structure of impact-compacted clays, Clays and Clay Minerals, 19, 239-249, 1971.

Engelhardt, W. v., and K. H. Gaida, Concentration changes of pore solutions during the compaction of clay sediments, J. Sed. Petrol., 33, 919-930, 1963.

Farmer, I. W., The Engineering Properties of Rocks, E. & F. N. Spon Ltd., London, 1968.

Gilbert, G. K., Earthquake forecasts, Science (New Series), 29, 121-138, 1909.

Gold, B., and C. Rader, Digital Processing of Signals, p. 199, McGraw-Hill Book Co., New York, 1969.

Grant, F. S., and G. F. West, Interpretation Theory in Applied Geophysics, McGraw-Hill Co., New York, 1965.

Greenberg, R. J., and W. F. Brace, Archie's law for rocks modeled by simple networks, J. Geophys. Res., 74, 2099-2102, 1969.

Guertin, J. D., Stability and Settlement Analyses of an Embankment on Clay, p. 30, Masters Thesis, Dept. of Civil Engineering, M.I.T., Cambridge, MA, 1967.

Hashin, Z., and S. Shtrikman, A variational approach to the theory of the effective magnetic permeability of multiphase materials, J. Appl. Phys., 33, 3125-3131, 1962.

Hill, H. J., and J. D. Milburn, Effect of clay and water salinity on electrochemical behavior of reservoir rocks, Trans. AIME, 207, 65-72, 1956.

Hodgson, E. A., A proposed research into the possibilities of earthquake prediction, Bull. Seis. Soc. Am., 13, 100-104, 1924.

Johnson, A. G., R. L. Kovach, A. Nur, and J. R. Booker, Pore pressure changes during creep events on the San Andreas fault, J. Geophys. Res., 78, 851-857, 1973.

Lachenbruch, A. H., and J. H. Sass, Thermo-mechanical aspects of the San Andreas fault system, Proc. Conf. on Tectonic Problems of the San Andreas Fault System, eds. R. L. Kovach and Amos Nur, 192-205, 1973.

Ladd, C. C., Class notes, 1.321, Soil Behavior, Dept. of Civil Engineering, M.I.T., Cambridge, MA, Spring, 1973.

Lambe, T. W., and R. V. Whitman, Soil Mechanics, John Wiley & Sons, Inc., New York, 1969.

Madden, T. R., Electrode Polarization and Its Influence On the Electrical Properties of Rocks, Ph.D. Thesis, M.I.T., Cambridge, MA, 1961.

Madden, T. R., The resolving power of geoelectric measurements for delineating resistive zones within the crust, in The Structure and Physical Properties of the Earth's Crust, ed. J. G. Heacock, Geophysical Monograph Series, 14, 95-105, Am. Geophys. Un., Washington, D. C., 1971.

Madden, T. R., Near Surface Electrical Properties of Rocks as a Guide to Mechanical Properties, Quarterly Report, 7 July-30 Sept. 1972, M.I.T., Cambridge, MA, 1972.

Madden, T. R., Class notes, 12.52, Geoelectricity and Geomagnetism, Dept. of Earth and Planetary Sciences, M.I.T., Cambridge, MA, Spring, 1974.

Madden, T. R., Y. E. Angoran, and K. Anderson, Near Surface Electrical Properties of Rocks as a Guide to Mechanical Properties, Quarterly Report, 9, 1 Jan.-31 March, 1974, M.I.T., Cambridge, MA, 1974.

Martin, R. T., Quantitative fabric of wet Kaolinite, Proc. 14th Conf., Clays and Clay Minerals, 271-287, 1966.

Martin, R. T., and C. C. Ladd, Fabric of Consolidated Kaolinite, Research Report R70-15, Soils Publication 254, Dept. of Civil Engineering, M.I.T., Cambridge, MA, 1970.

Mazzella, Aldo, and H. F. Morrison, Electrical resistivity variations associated with earthquakes on the San Andreas fault, Science, 185, 855-857, 1974.

McKyes, E., and R. N. Yong, Three techniques for fabric viewing as applied to shear distortion of a clay, Clays and Clay Minerals, 19, 289-293, 1971.

Nason, R. D., Investigation of Creep Slippage in Northern Central California, Ph.D. Thesis, University of California, San Diego, 1971.

Nersesov, I. L., A. N. Semenov, and I. G. Simbireva, Space-time distribution of the travel time ratios of transverse and longitudinal waves in the Garm area, in Experimental Seismology, 334-345, Akad. Nauk. USSR Publication, 1971.

Nur, Amos, Effects of Stress and Fluid Inclusions on Wave Propagation in Rock, Ph.D. Thesis, M.I.T., Cambridge, MA, 1969.

Nur, Amos, Dilatancy, pore fluids, and premonitory variations of t_s/t_p travel times, Bull. Seis. Soc. Am., 62, 1217-1222, 1972.

Nur, Amos, and G. Simmons, The effect of saturation on velocity in low porosity rocks, Earth Planet. Sci. Lett., 7, 183-193, 1969.

Nye, J. F., Physical Properties of Crystals, Oxford University Press, London, 1969.

Overbeek, J. Th. G., Electrokinetic phenomena, in Colloid Science, VI, Irreversible Systems, ed. H. R. Kruyt, 194-244, Elsevier Publishing Co., Amsterdam, 1952.

Sadovsky, M. A., I. L. Nersesov, S. K. Nigmatullaev, L. A. Latynina, A. A. Lukk, A. E. Semenov, I. G. Simbireva, and V. I. Ulomov, The processes preceding strong earthquakes in some regions of Middle Asia, Tectonophysics, 14, 295-307, 1972.

Scholz, C. H., and R. Kranz, Notes on Dilatancy Recovery, Lamont-Doherty Contribution No. 0000, Lamont-Doherty Geological Observatory, Columbia University, Palisades, New York, 1974.

Scholz, C. H., L. R. Sykes, and V. P. Aggarwal, Earthquake prediction: a physical basis, Science, 181, 803-810, 1973.

Semenov, A. N., Variations in travel time of transverse and longitudinal waves before violent earthquakes, Bull. Akad. Sci. USSR, Phys. Solid Earth, 3, 245-248, 1969.

Stesky, R. M., and W. F. Brace, Estimation of frictional stress on the San Andreas fault from laboratory measurements, Proc. Conf. on Tectonic Problems of the San Andreas Fault System, eds. R. L. Kovach and Amos Nur, 206-214, 1973.

Street, N., and A. S. Buchanan, The ζ-potential of Kaolinite particles, Australian J. Chem., 9, 450-466, 1956.

van Olphen, H., An Introduction to Clay Colloid Chemistry, Interscience Publishers, New York, 1963.

Walsh, J. B., The effect of cracks on the compressibility of rock, J. Geophys. Res., 70, 381-389, 1965.

Waxman, M. H., and L. J. M. Smits, Electrical conductivities in oil-bearing shaly sands, Trans. AIME, 243, 107-122, 1968.

Waxman, M. H., and E. C. Thomas, Electrical conductivity in shaly sands, J. Petrol. Tech., 26, 213-225, 1974.

Weertman, J., and J. R. Weertman, Elementary Dislocation Theory, The Macmillan Co., London, 1969

Wesson, R. L., R. O. Burford, and W. L. Ellsworth, Relationship between seismicity, fault creep and crustal loading along the central San Andreas fault, Proc. Conf. on Tectonic Problems of the San Andreas Fault System, eds. R. L. Kovach and Amos Nur, 303-321, Stanford University, Stanford, 1973.

Whitcomb, J. H., J. D. Garmany, and D. L. Anderson, Earthquake prediction: variation of seismic velocities before the San Francisco earthquake, Science, 180, 632-635, 1973.

Wilson, I. F., Geology of San Benito Quadrangle, California, Calif. J. Mines & Geology, 32, 183-270, 1943.

Winsauer, W. O., and W. M. McCardell, Ionic double-layer conductivity in reservoir rocks, Trans. AIME, 198, 129-134, 1953.

Worral, W. E., Clays, Their Nature, Origin and General Properties, Transatlantic Arts, New York, 1968.

Wyss, Max, and D. S. Holcomb, Earthquake prediction based on seismic residuals, Nature, 245, 139-140, 1973.

Yamazaki, Yoshio, Electrical conductivity of strained rocks, Bull. Earthq. Res. Inst., 45, 849-860, 1967.

APPENDIX A: OPTICAL METHOD FOR DETERMINING SAMPLE SILHOUETTE
             AND K_g

While the sample impedance is easy to measure during
triaxial tests, determination of the silhouette is a little
tricky. The sample is enclosed in a plastic cylinder which
is filled with water. The silhouette is greatly modified
by this system. To measure how much distortion there is, a
piece of graph paper was mounted inside the cell in the plane
of the silhouette and photographed. Figure A-1 shows the
optical transformation which takes place, and the experiment
geometry. Figure A-2 shows the grid system as viewed
with and without the fluid filled plastic enclosure, and
the apparent displacements of the grid points. Let the
original coordinates of the grid points be (ξ, η) and the
distorted, digitized points be (x, y). By photographing
the silhouette during the experiment we get points in the
(x, y) coordinate system which we transform to the (ξ, η) sys-
tem to get the actual silhouette. The transformation is
made by means of a table
look-up and interpolation.
For the table, points equally
spaced in (x,y) are needed, but
we only have equally spaced
(ξ, η) data, i.e., unequally
spaced (x, y) data. A quick
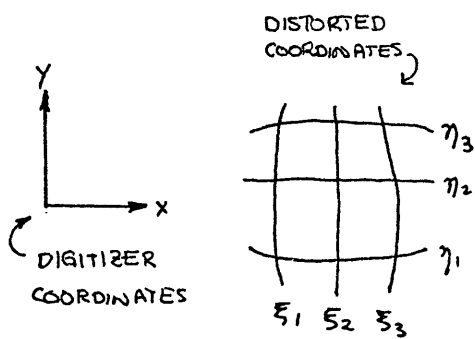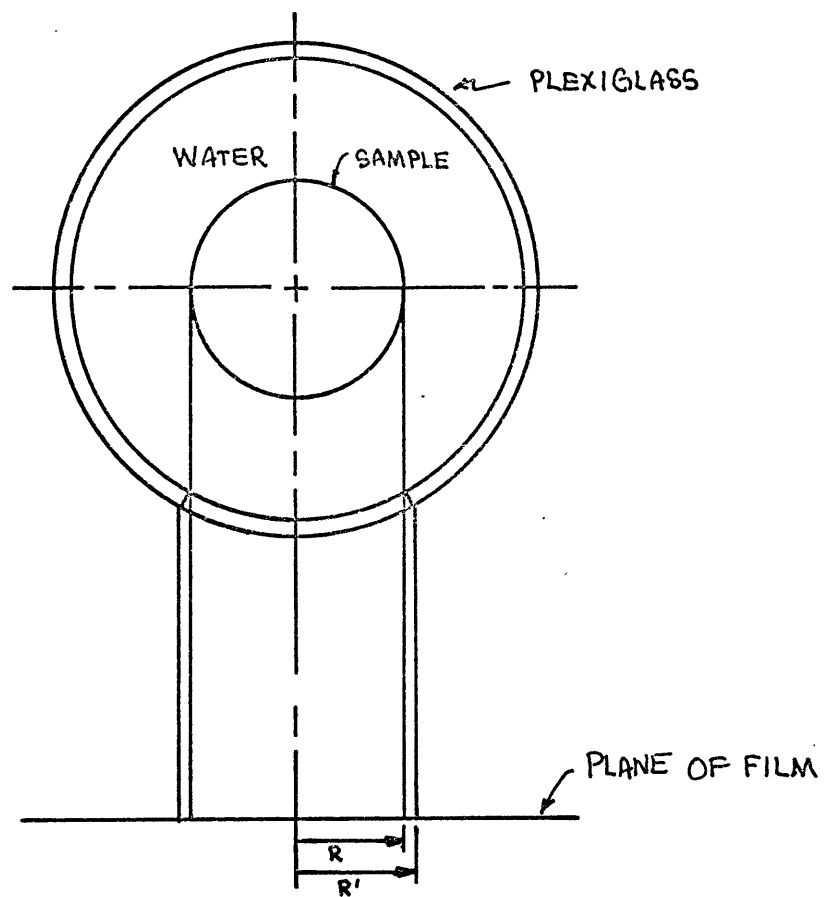
FIGURE A-I   GEOMETRY OF CELL AND DISTORTION

OF SILHOUETTE
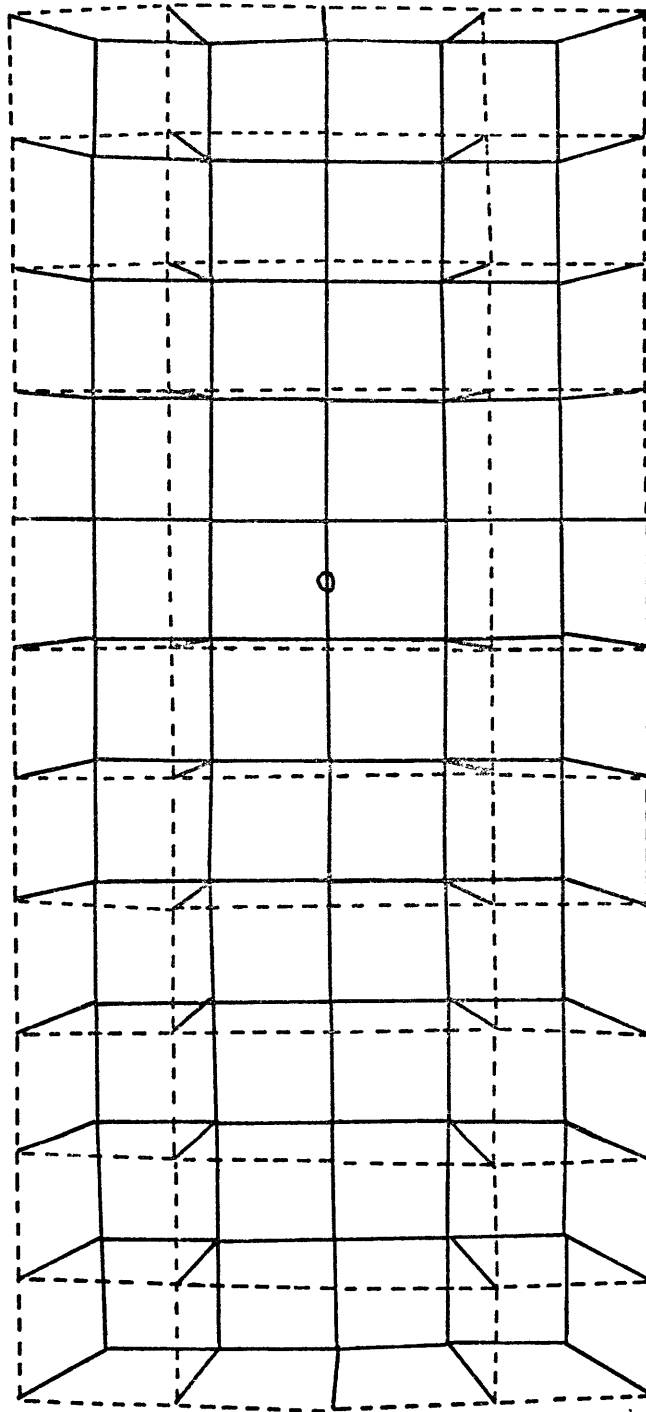
FIGURE A-2   DISTORTION OF GRID BY CELL

—— ORIGINAL GRID   ---DISTORTED GRID

look through some standard numerical analysis books un-
covered no method for two-dimensional interpolation of
unequally spaced data. The following method was used.

If we Fourier transform the ξ and η functions at a
set of equally spaced frequencies, add zeros to the spectrum
above the Nyquist frequency, and inverse transform we will
have a band-limited interpolation at equally spaced x and
y (Gold and Rader, 1969). The first Fourier transform must
be done brute force since the data is unevenly spaced.

$$\overrightarrow{\boldsymbol{\Xi}}(r,s) = \sum_{k=0}^{N-1} \sum_{\ell=0}^{M-1} \xi(x_{k,\ell}, y_{k,\ell}) \, e^{-j\left[\Delta\omega_1 r x_{k,\ell} + \Delta\omega_2 s y_{k,\ell}\right]}$$

$$= \sum_{k=0}^{N-1} \xi(x_k) \sum_{\ell=0}^{M-1} e^{-j\left[\Delta\omega_1 r x_{k,\ell} + \Delta\omega_2 s y_{k,\ell}\right]} \qquad \text{A-1}$$

$$\boldsymbol{H}(r,s) = \sum_{\ell=0}^{M-1} \sum_{k=0}^{N-1} \eta(x_{k,\ell}, y_{k,\ell}) \, e^{-j\left[\Delta\omega_1 r x_{k,\ell} + \Delta\omega_2 s y_{k,\ell}\right]}$$

$$= \sum_{\ell=0}^{M-1} \eta(y_\ell) \sum_{k=0}^{N-1} e^{-j\left[\Delta\omega_1 r x_{k,\ell} + \Delta\omega_2 s y_{k,\ell}\right]} \qquad \text{A-2}$$

Note that ξ is constant along "vertical" lines, and η is
constant along "horizontal" lines. The transforms are
computed for $0 \le \omega_1 \le (N-1)\Delta\omega_1$ and $-(M-1)\Delta\omega_2 \le \omega_2 \le (M-1)\Delta\omega_2$.
Then using the symmetry condition $F(-\omega_1, -\omega_2) = F^*(\omega_1, \omega_2)$ the
remainder of the transform is computed. (This is necessary
to insure a real inverse.) The functions $\xi(x)$ and $\eta(y)$ are
periodic requiring the fitting of a Fourier series to a

function with a very large jump. This is very hard to do, especially with a small number of terms. A much better Fourier representation can be obtained by subtracting a sawtooth from $\xi(x)$ and $\eta(y)$ before transforming, and adding it back after inverse transforming. This makes the function being transformed become one with small oscillations about zero.

The discrete Fourier transform (DFT) also assumes the spectrum is cyclical. The proper symmetry is shown in Figure A-3. The transform is stored in a $N' \times M'$ array where these numbers are the smallest power of two larger than N and M respectively. The frequencies above the Nyquist frequencies are given the value of zero (also shown in Figure A-3). A 2-D fast Fourier transform (FFT) routine is now used to get the equally spaced transfer function. The spacing in x and y are given by $\Delta x = \dfrac{2\pi}{\Delta \omega_1 N'}$ and $\Delta y = \dfrac{2\pi}{\Delta \omega_2 M'}$ respectively.

At various points during the experiment photographs of the silhouette are made. Points along the silhouette are digitized (x-y coordinates) and transformed (ξ-η coordinates). The silhouette is then used to calculate the integral in Equation 2-12 using Simpson's extended rule (Abramowitz and Stegun, 1968).

As a check on the accuracy of the method a known silhouette was constructed and photographed. The profile chosen was

$$R(z) = R_o - \frac{R_o - R_H}{H^2} z^2 \qquad \text{A-3}$$
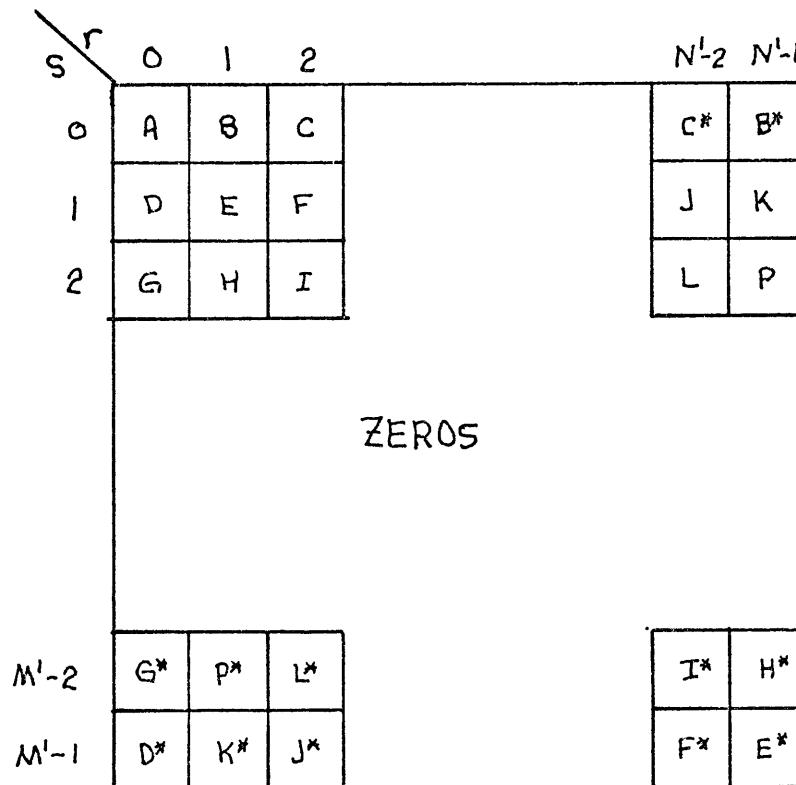
FIGURE A-3   SYMMETRY OF 2-D DISCRETE
FOURIER TRANSFORM
* DENOTES COMPLEX CONJUGATE
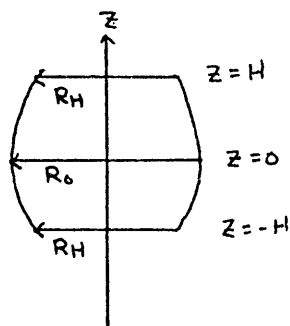
Typical values are R_H=1.5 cm, R_O=2.5 cm, and H=3.5 cm. From Equation 2-12

$$\frac{1}{K_g} = \frac{1}{\pi} \int_{-H}^{H} \frac{dz}{\left[\frac{R_H - R_O}{H^2} z^2 + R_O\right]^2} \qquad \text{A-4}$$

This is a standard integral of the form

$$\int \frac{dx}{(a+bx^2)^2} = \frac{x}{2a(a+bx^2)} + \frac{1}{4a\sqrt{-ab}} \log \frac{a + x\sqrt{-ab}}{a - x\sqrt{-ab}} \qquad \text{A-5}$$

Replacing a and b with R_O and $\frac{R_H - R_O}{H^2}$ respectively, Equation A-4 becomes

$$\frac{1}{K_g} = \frac{1}{\pi}\left[\frac{H}{R_O R_H} + \frac{H}{2R_O\sqrt{R_O(R_O - R_H)}} \log \frac{R_O + \sqrt{R_O(R_O - R_H)}}{R_O - \sqrt{R_O(R_O - R_H)}}\right] \qquad \text{A-6}$$

which for the above values give K_g^{-1}=0.5072. The result obtained from the photographic method gave 0.5217 which corresponds to an accuracy of 2.9%. This type of test gives the accuracy of the method assuming the sample remains cylindrically symmetric. Corrections for any variation from cylindrical symmetry can only be approximate. This might be done by photographing the sample from several directions, and then averaging the geometry factors from all the views.

APPENDIX B: TRIAXIAL RESULTS FOR CLAY EXPERIMENTS

Included in this appendix are the results from the resistivity measurements made on triaxially loaded clay. Plots of resistivity (ρ) and deviator stress ($\sigma_1 - \sigma_2$) as a function of axial strain (ε_z), are presented for all experiments. All resistivities are measured in the vertical direction. In addition, volume change as a function of ε_z and resistivity as a function of porosity (n) are presented for most of the drained experiments (CID). The units used are: resistivity (Ωm), volume change (cm^3), stress (kg/cm^3), strain (%), and pore fluid concentration (mole/ℓ).

The compressional loading tests (COMP) had resistivity measured in the principal stress direction (vertical), while for the extensional loading test (EXT) resistivity was measured perpendicular to the horizontally aligned principal stress. Initial volumes of the specimens were 80.0 cm^3 and 50.0 cm^3 for the compressional and extensional tests respectively. All samples were kaolinite except T318 and T324 which were Boston blue clay (BBC).

Symbols used in the ρ-n diagrams are: ($\cdot$) consolidation, (o) rebound, and ($\times$) triaxial loading or unloading.
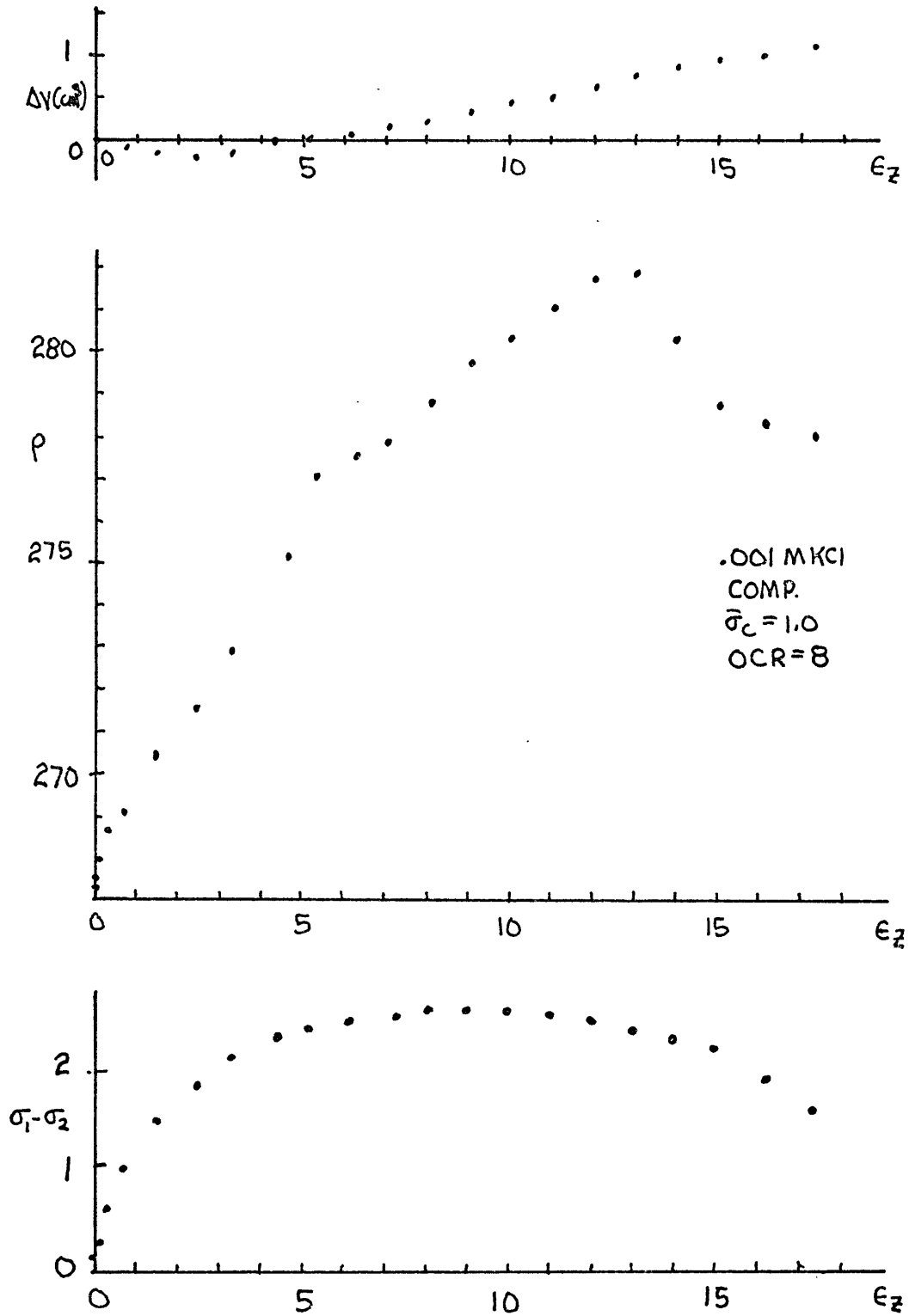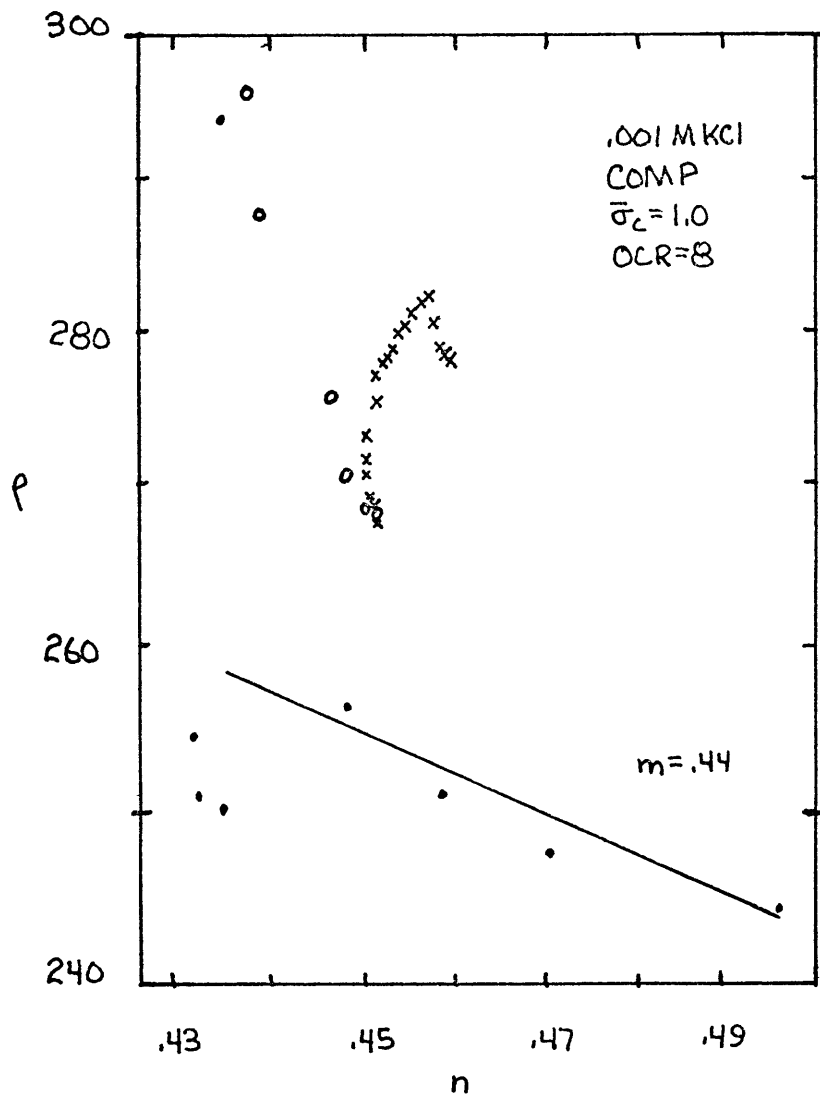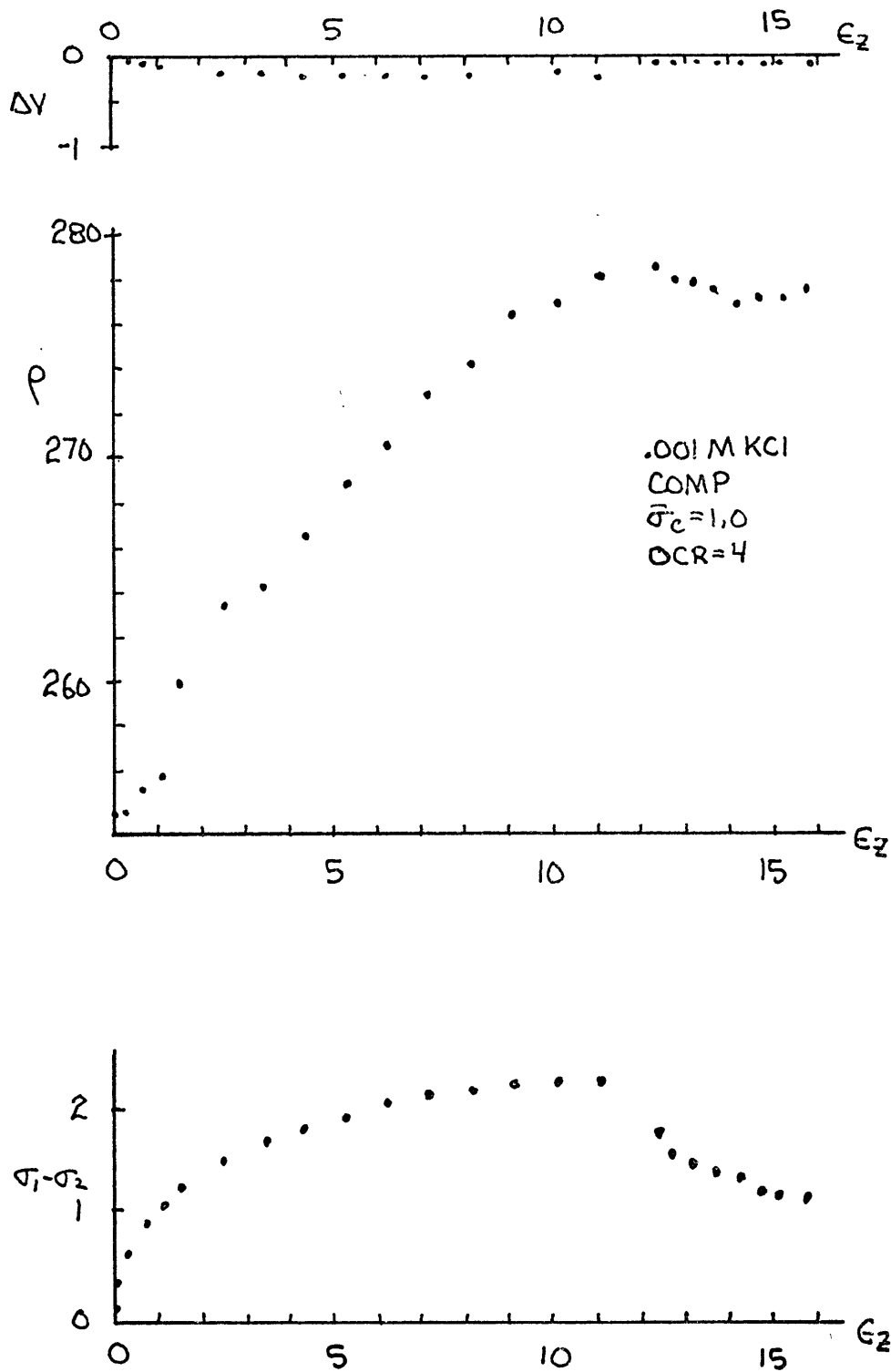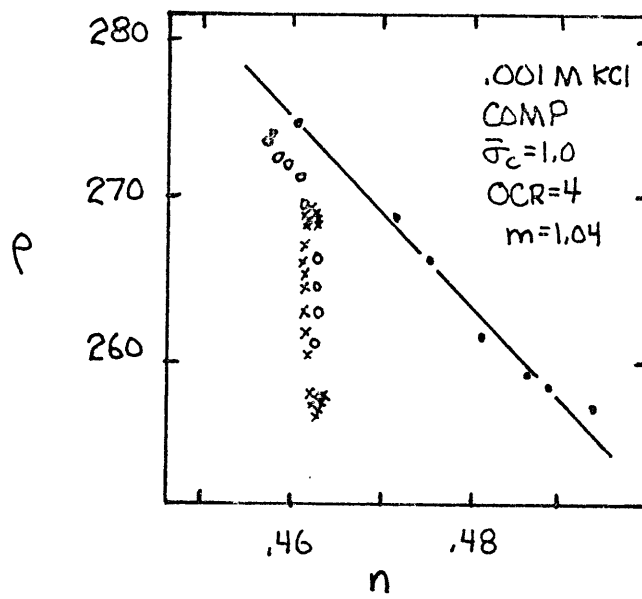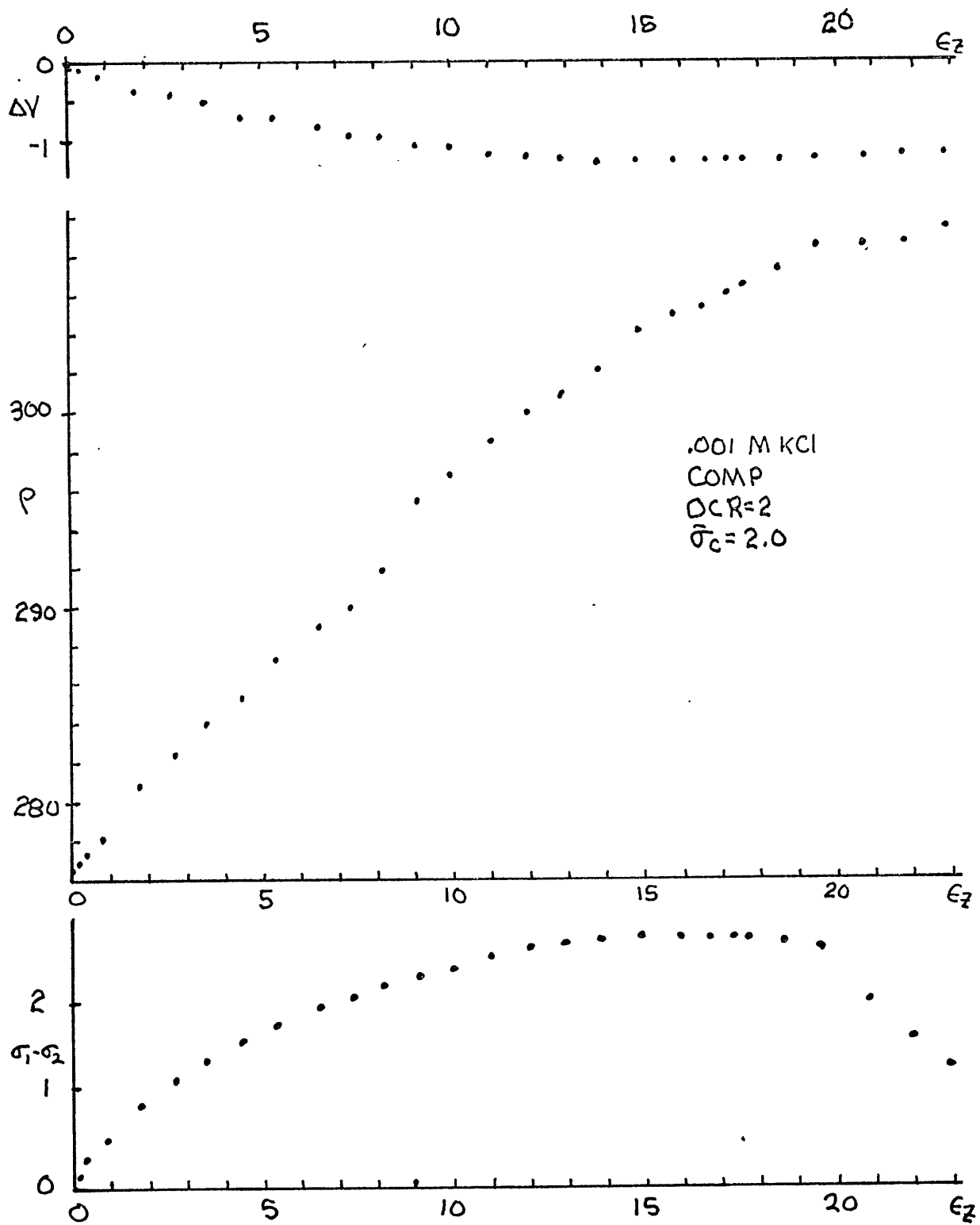
.OOI M KCl
COMP.
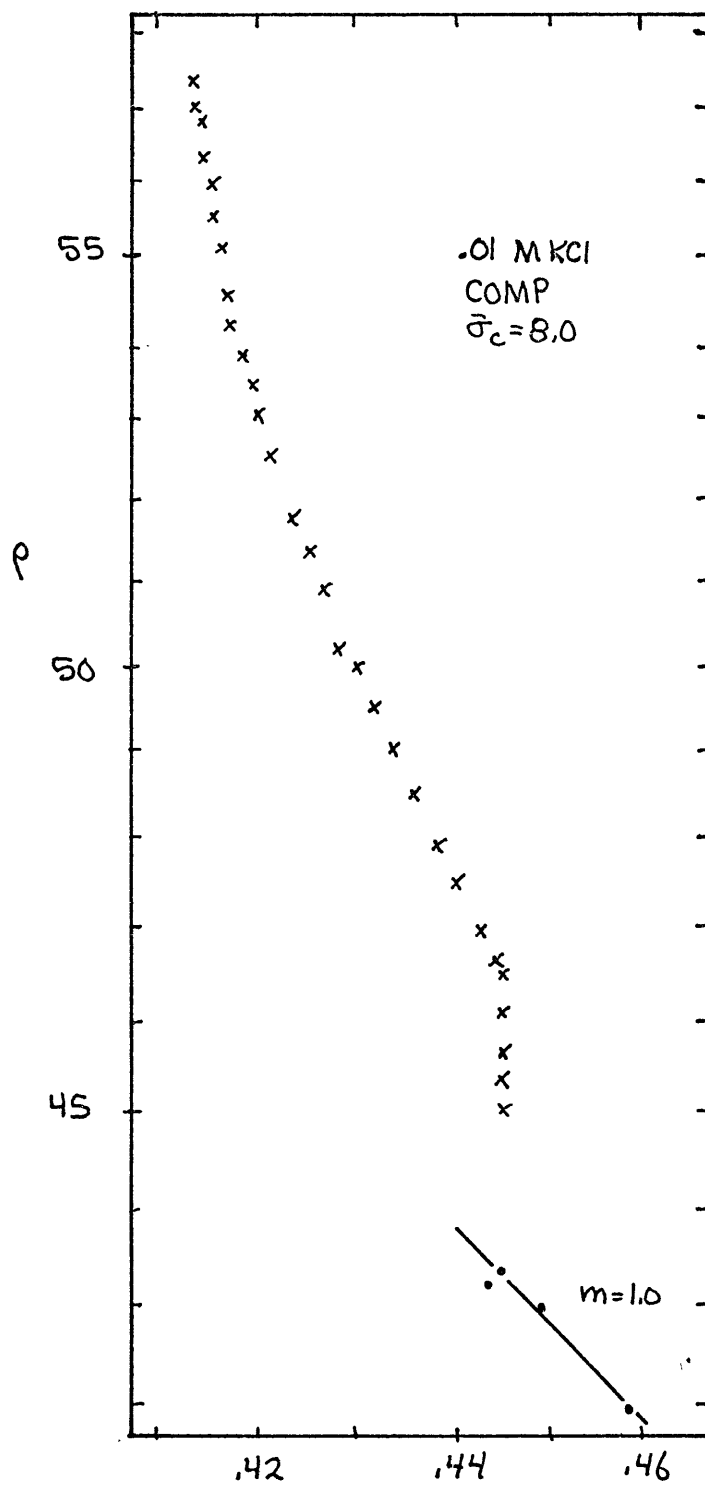$\bar{\sigma}_c = 1.0$
OCR=8

T302

FIGURE B-1 ρ, ΔV, $\sigma_1 - \sigma_2$ vs. ϵ_z

FIGURE 8-2   T302   ρ vs n

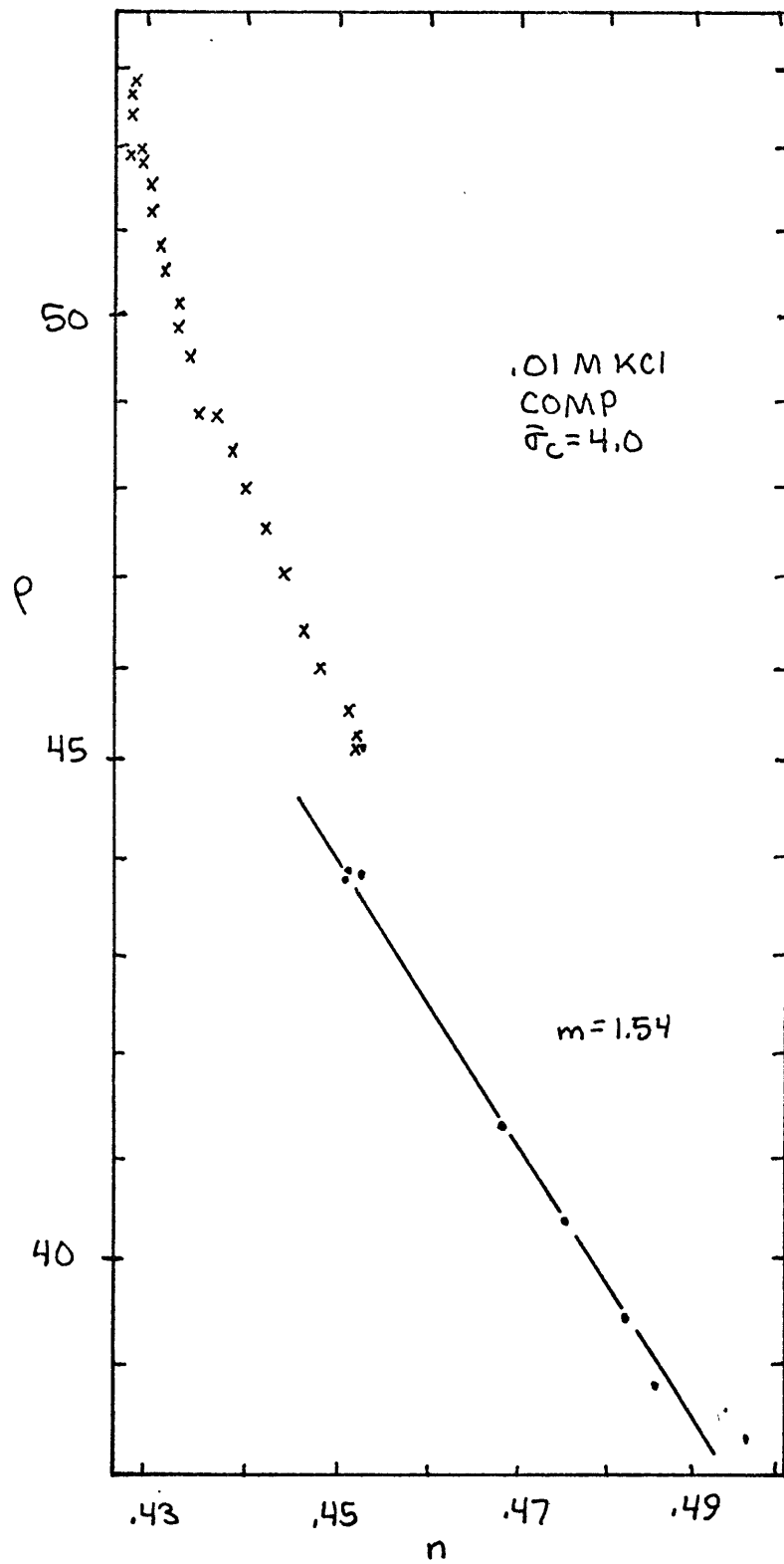FIGURE B-3 T304 ρ, ΔV, $\sigma_1 - \sigma_2$ vs ϵ_z

FIGURE B-4   T304 ρ vs. n

.OOI M KCl
COMP
OCR=2
$\bar{\sigma}_c = 2.0$

FIGURE B-5 T305ρ, ΔV, $\sigma_1 - \sigma_2$ vs. ϵ_z

176

FIGURE B-6 T305 ρ vs. n

FIGURE B-7   T307 $\rho, \Delta V, \sigma_1-\sigma_2$ vs. ϵ_z

FIGURE 8-8   T307 ρ vs. n

FIGURE B-9 T310 ρ ,ΔY,σ_1-σ_2 vs ϵ_z

.001 M KCl
COMP
$\bar{\sigma}_c = 2.0$

$m = 1.14$
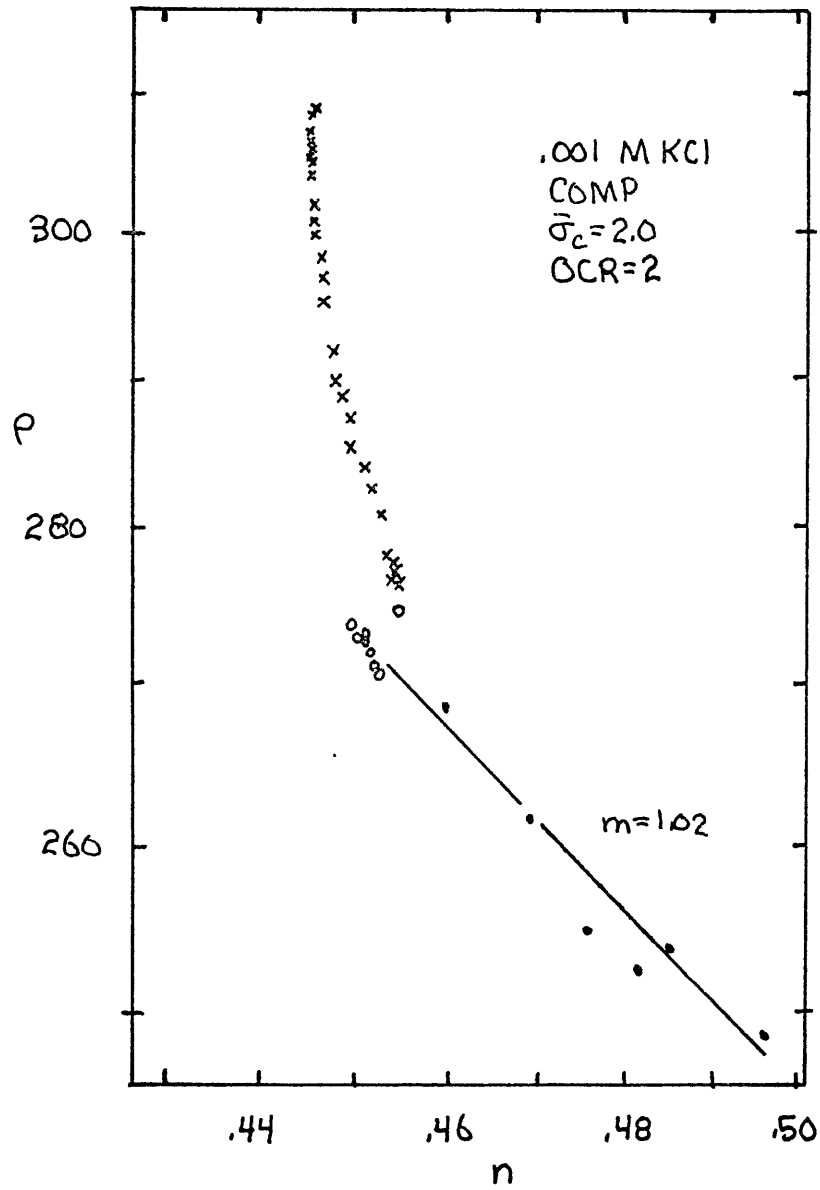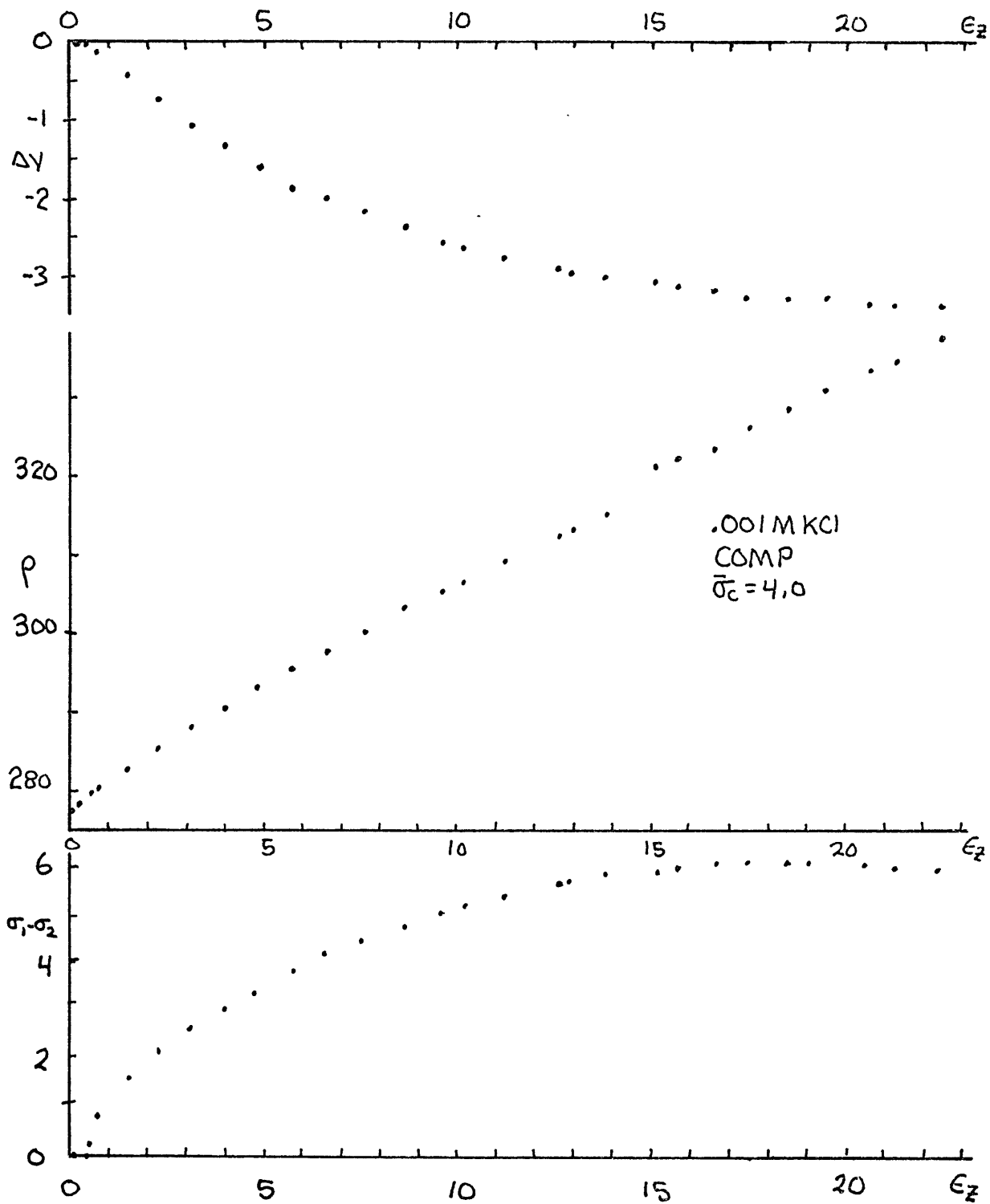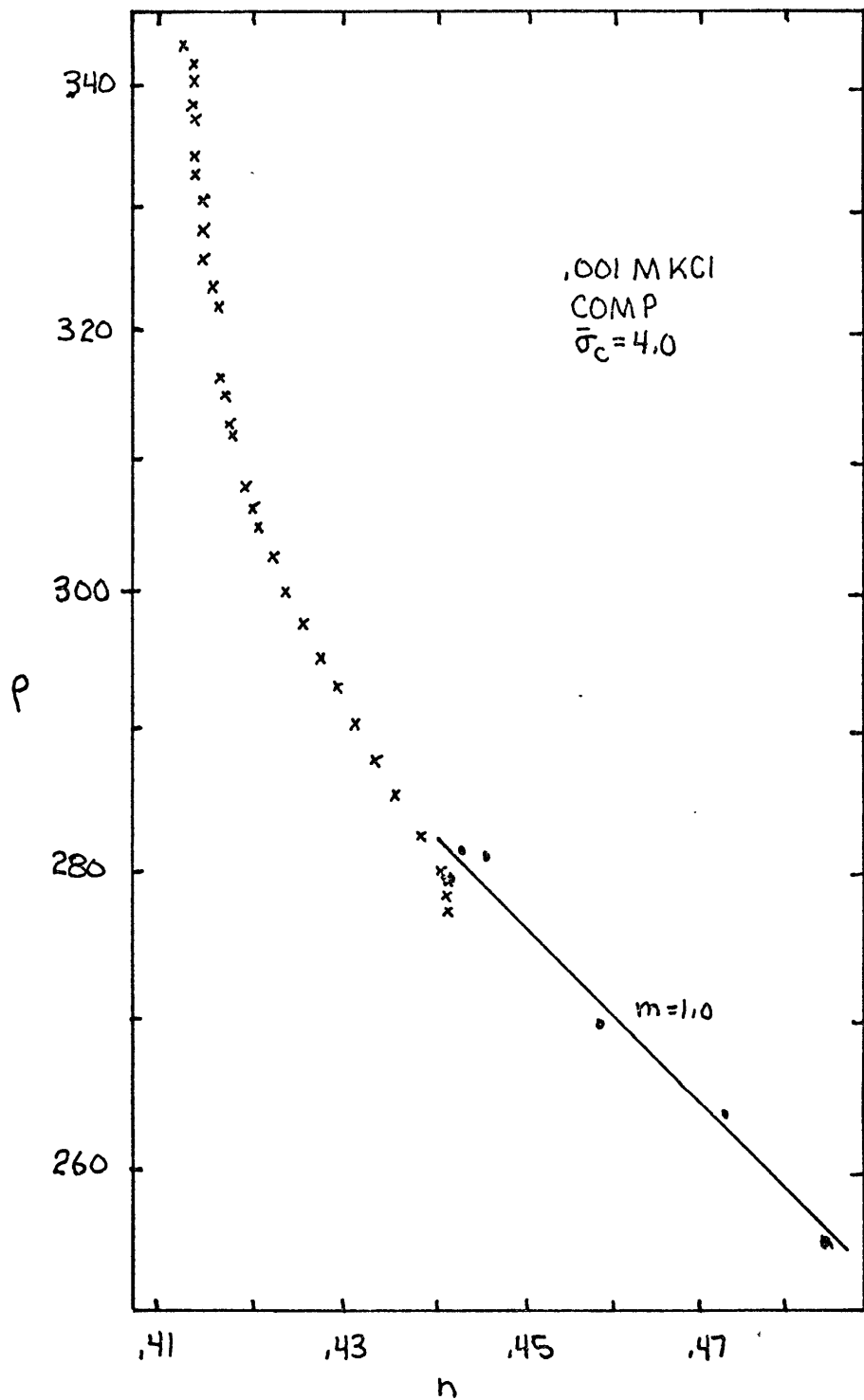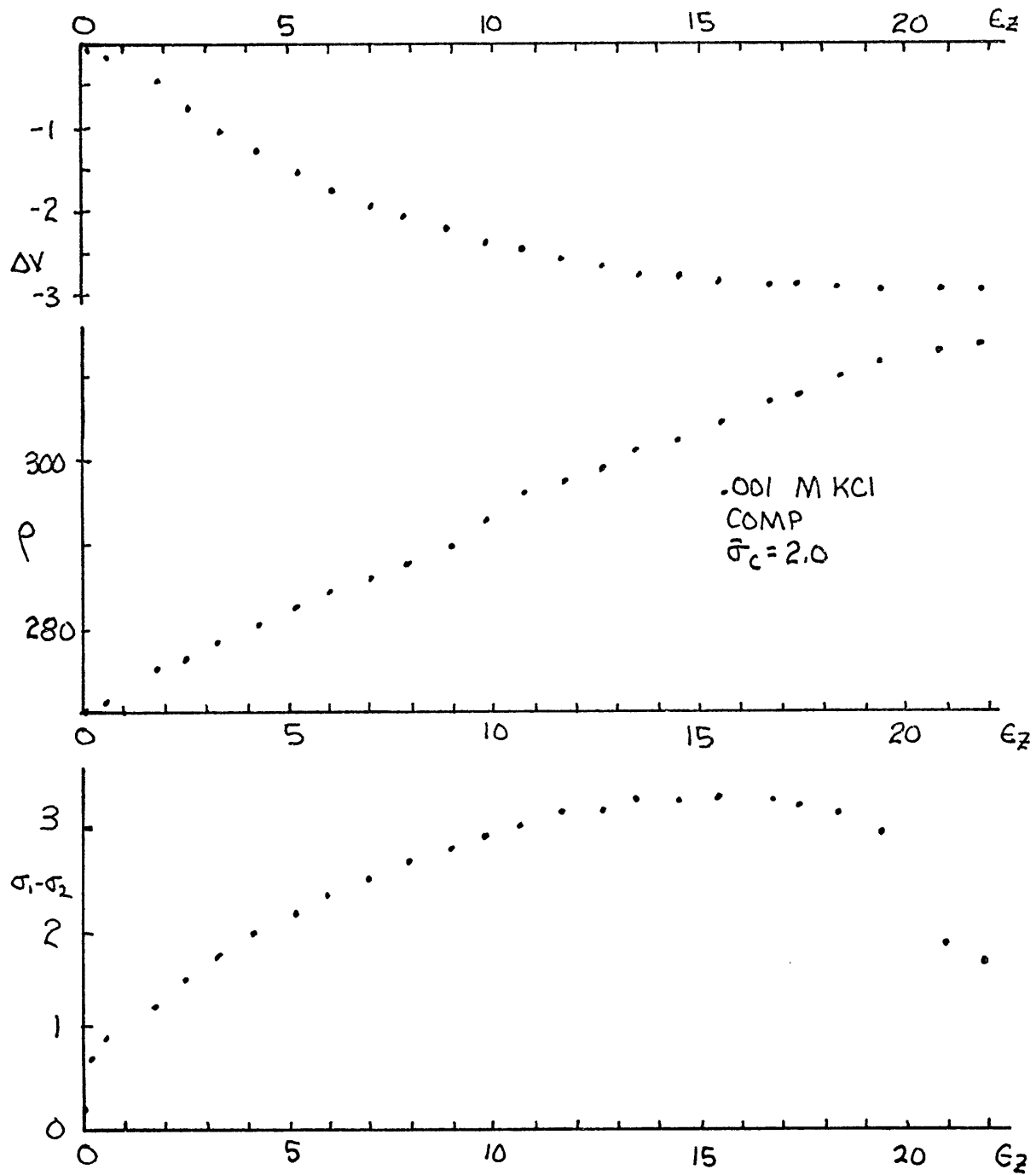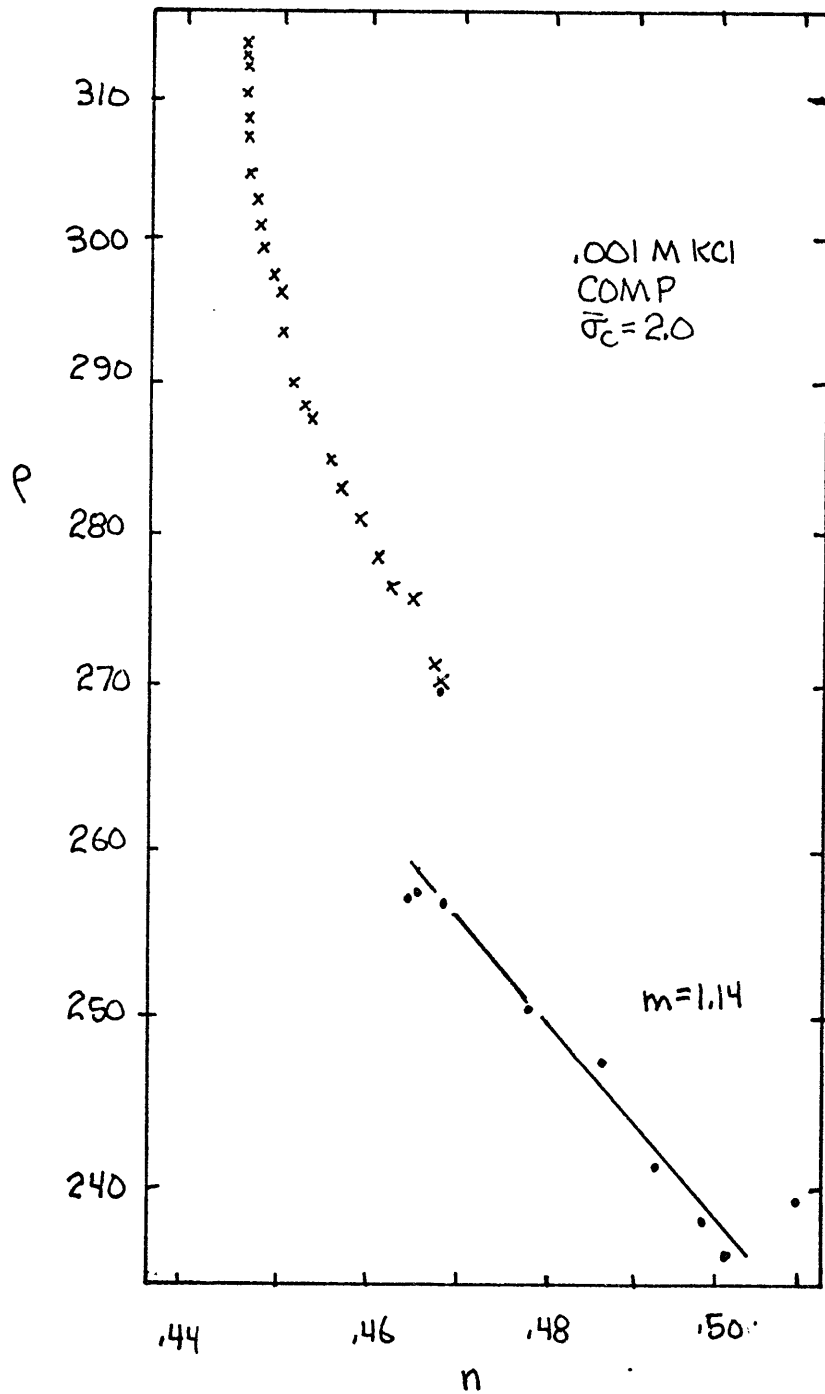
FIGURE B-10 T310 ρ vs. n
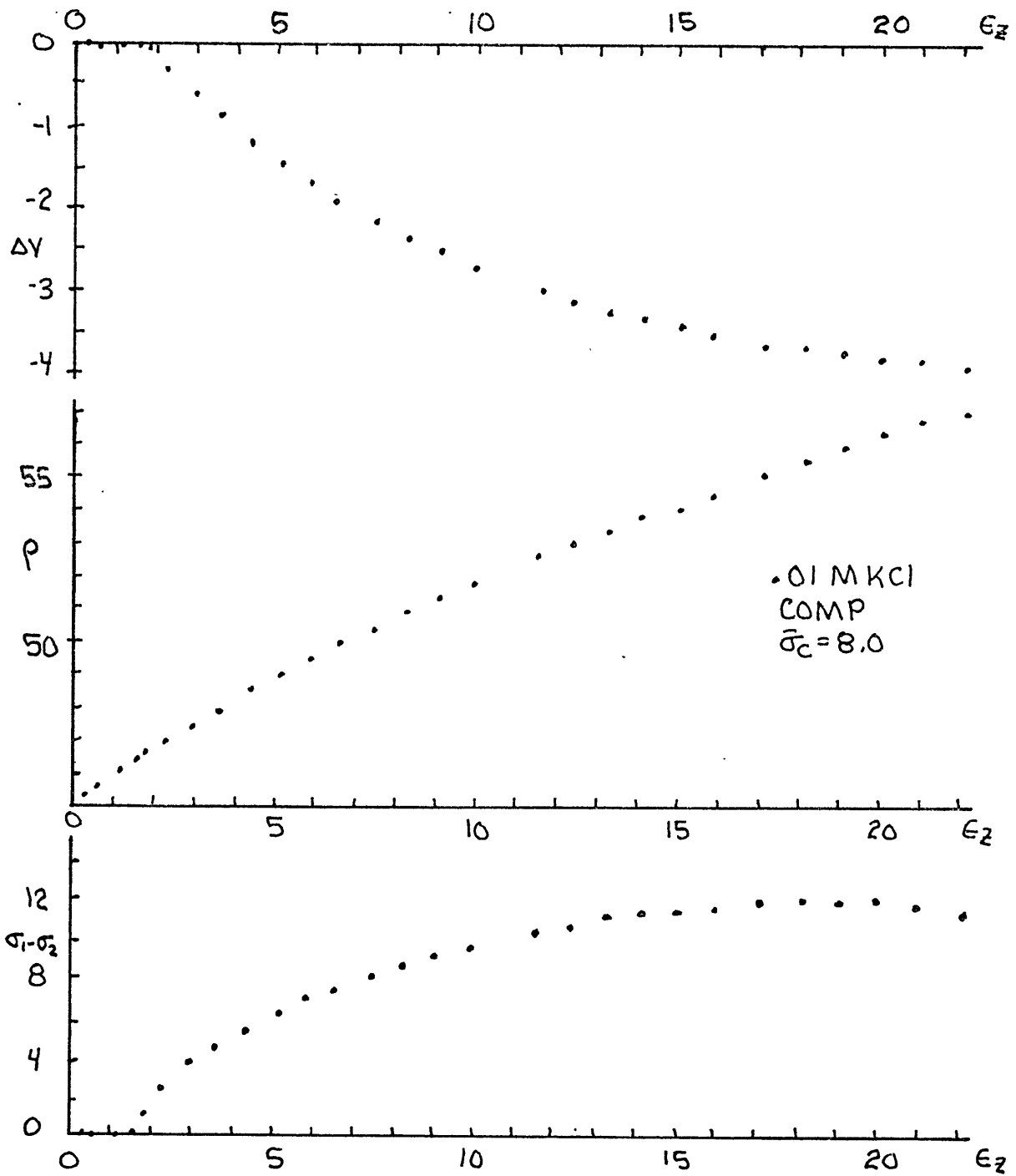
FIGURE B-11   T312 $\rho, \Delta V, \sigma_1 - \sigma_2$ vs. n

FIGURE 8-12 T312 ρ vs. n
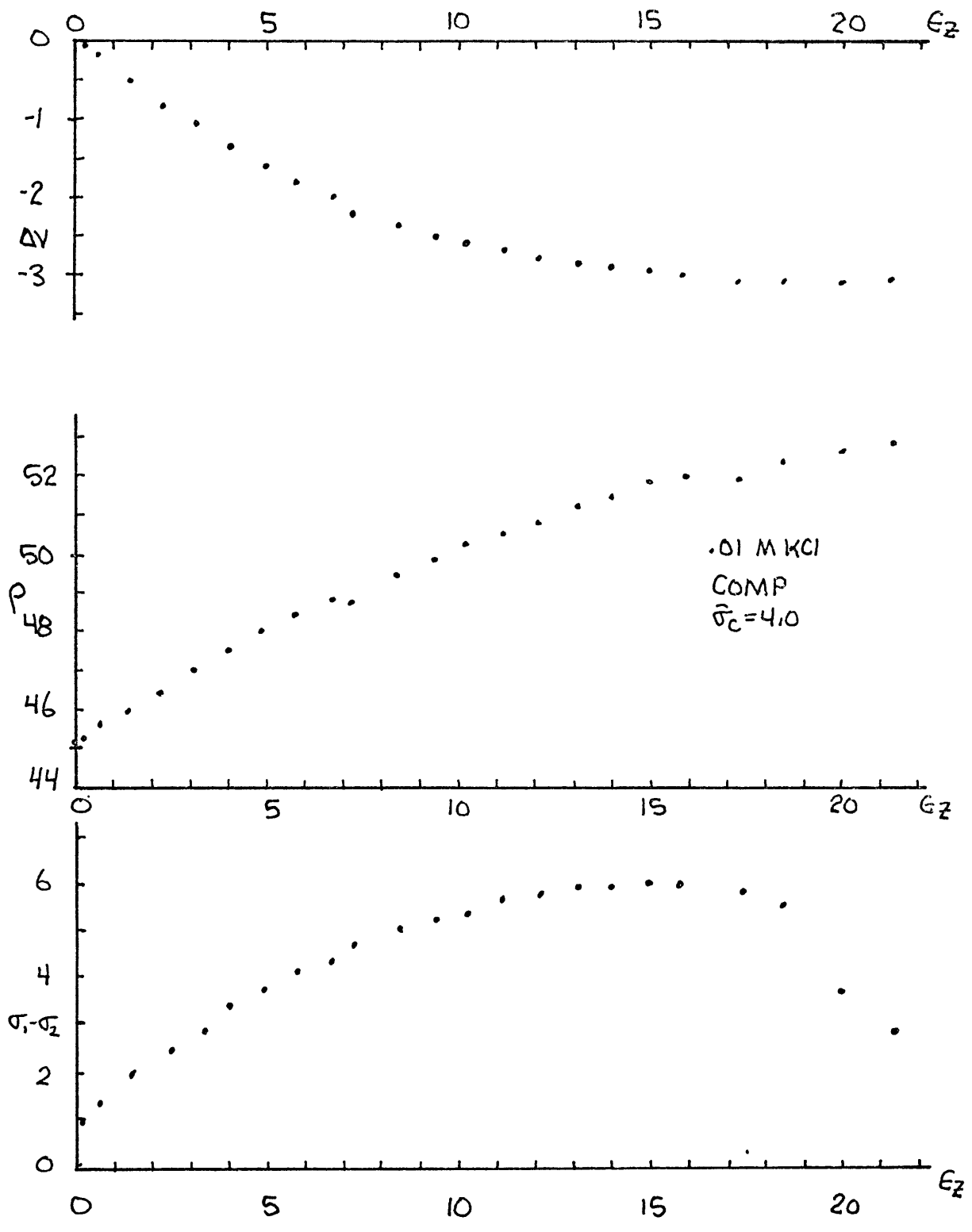
FIGURE B-13 T314 $\rho, \Delta V, \sigma_1 - \sigma_2$ VS. ϵ_z

FIGURE B-14 T314 ρ vs. n

FIGURE B-15 T315 ρ, ΔV, $\sigma_1 - \sigma_2$ vs. ϵ_z

FIGURE B-16 T315 ρ vs n

.OI M KCI
COMP
$\bar{\sigma}_c = 4.0$
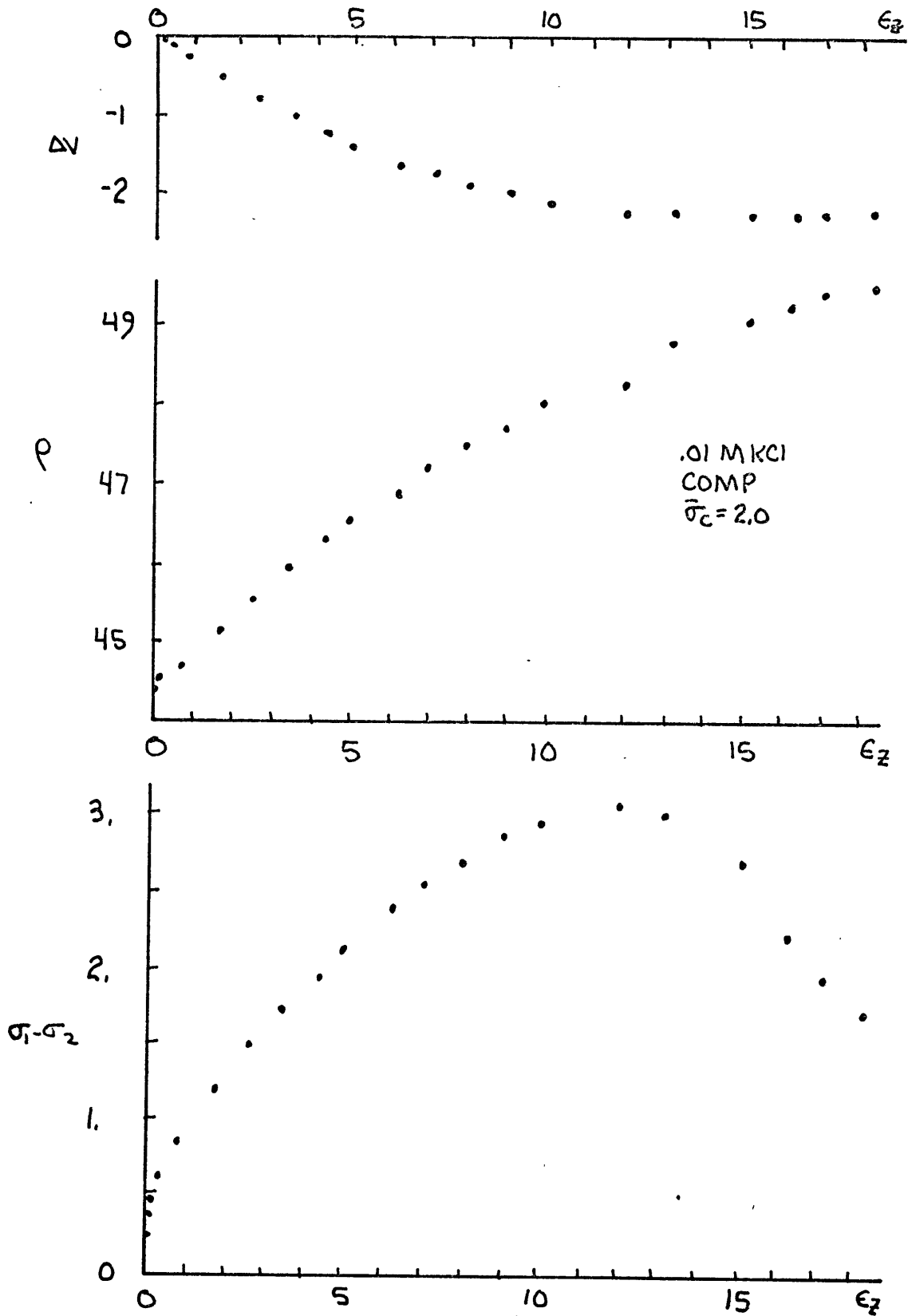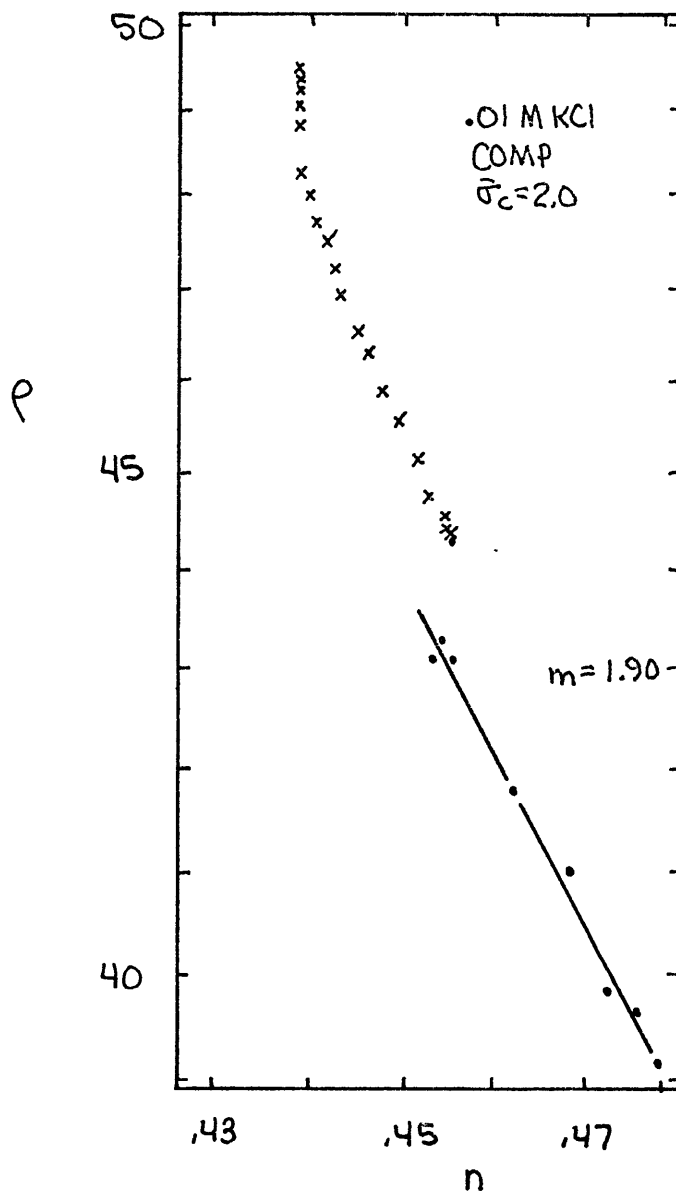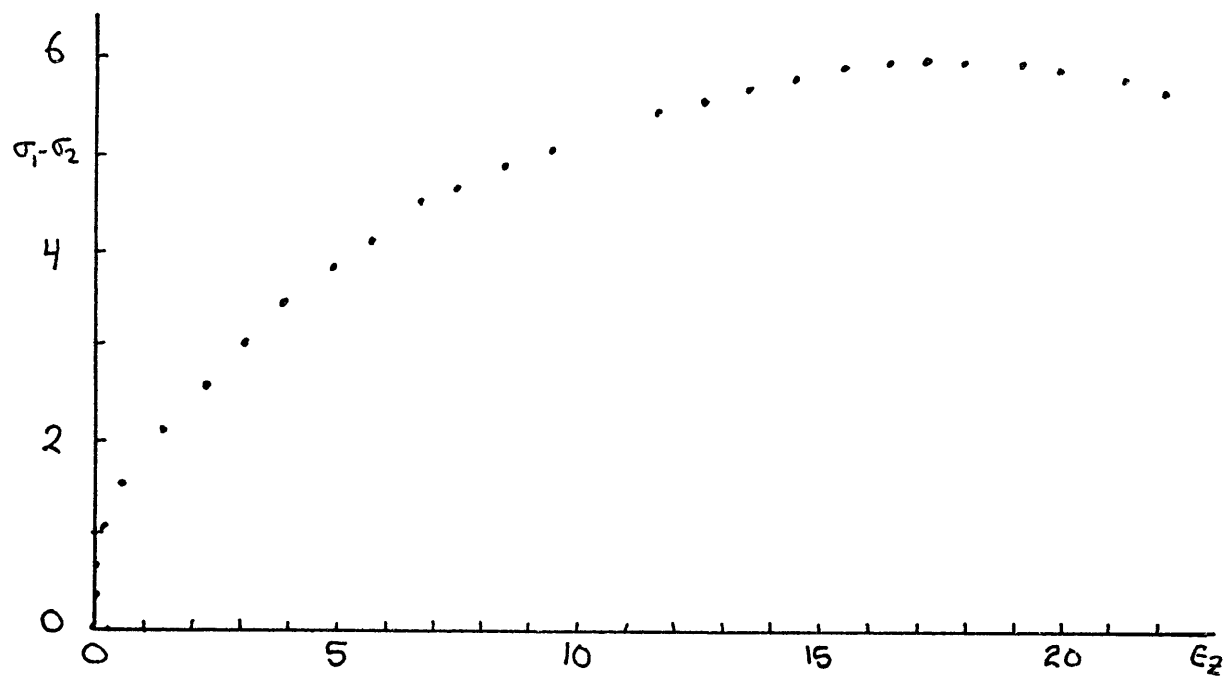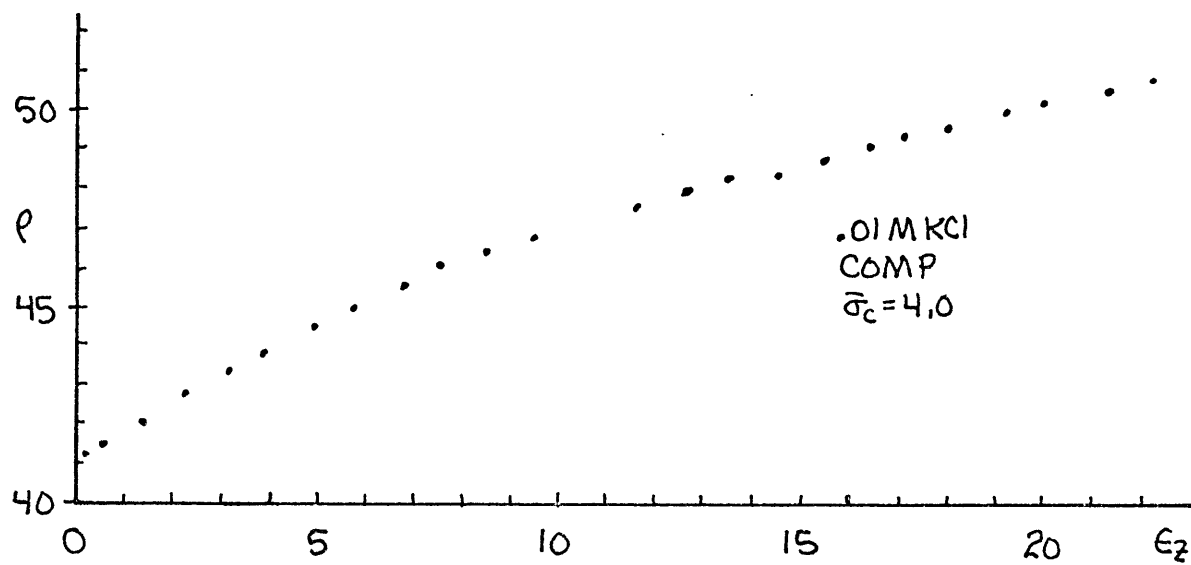
FIGURE 8-17 T 317 $\rho, \sigma_1-\sigma_2$ VS. ϵ_z
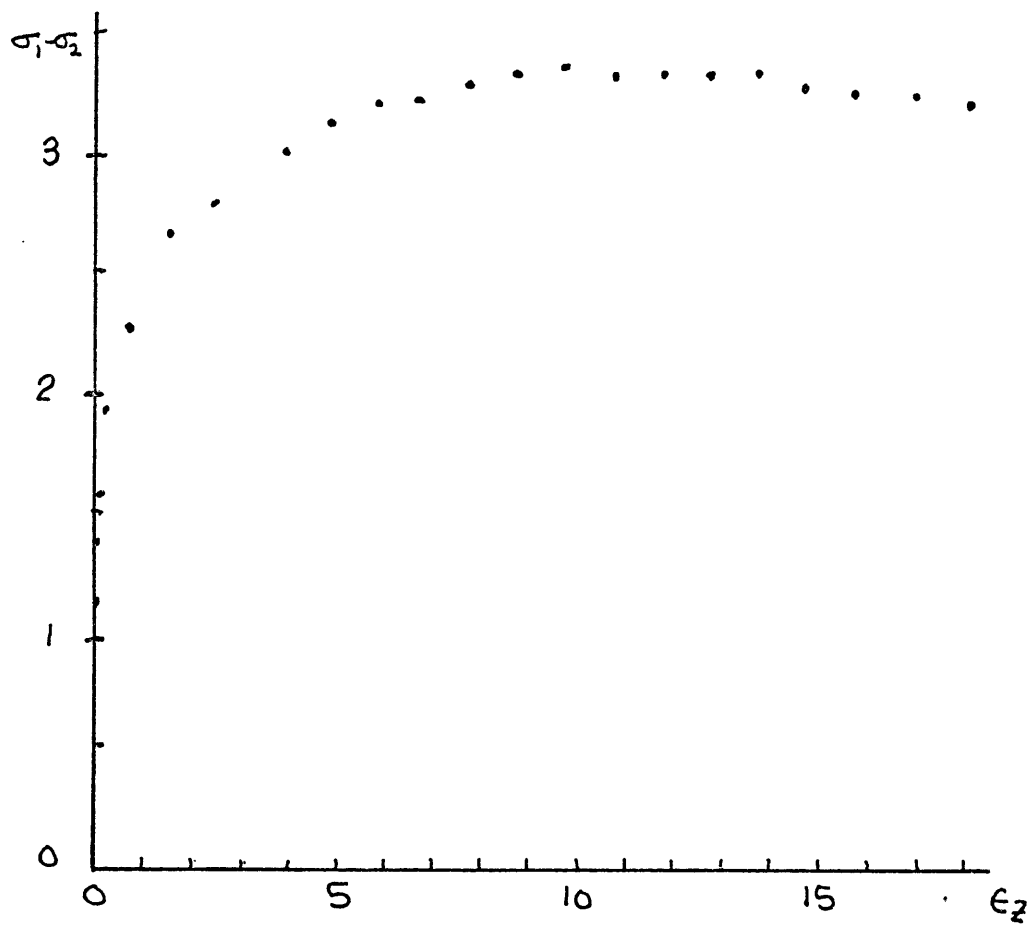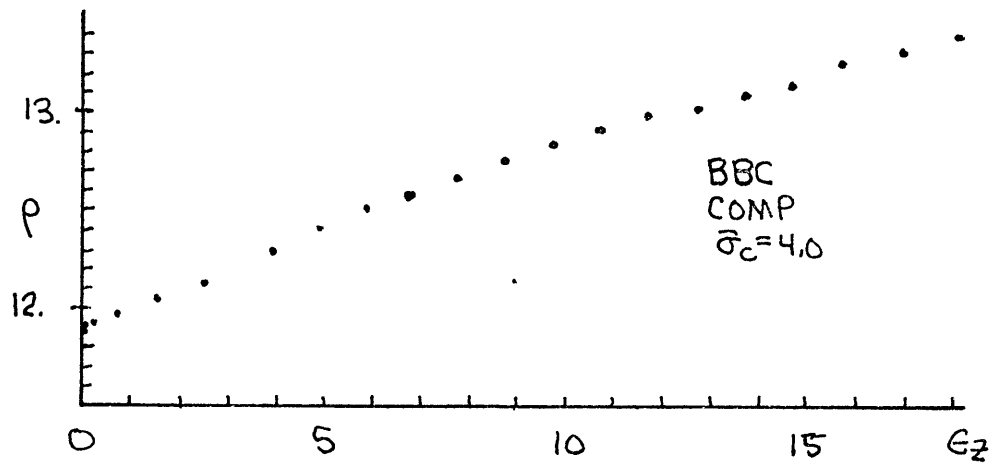
FIGURE B-18 T318 $\rho, \sigma_1 - \sigma_2$ vs. ϵ_z
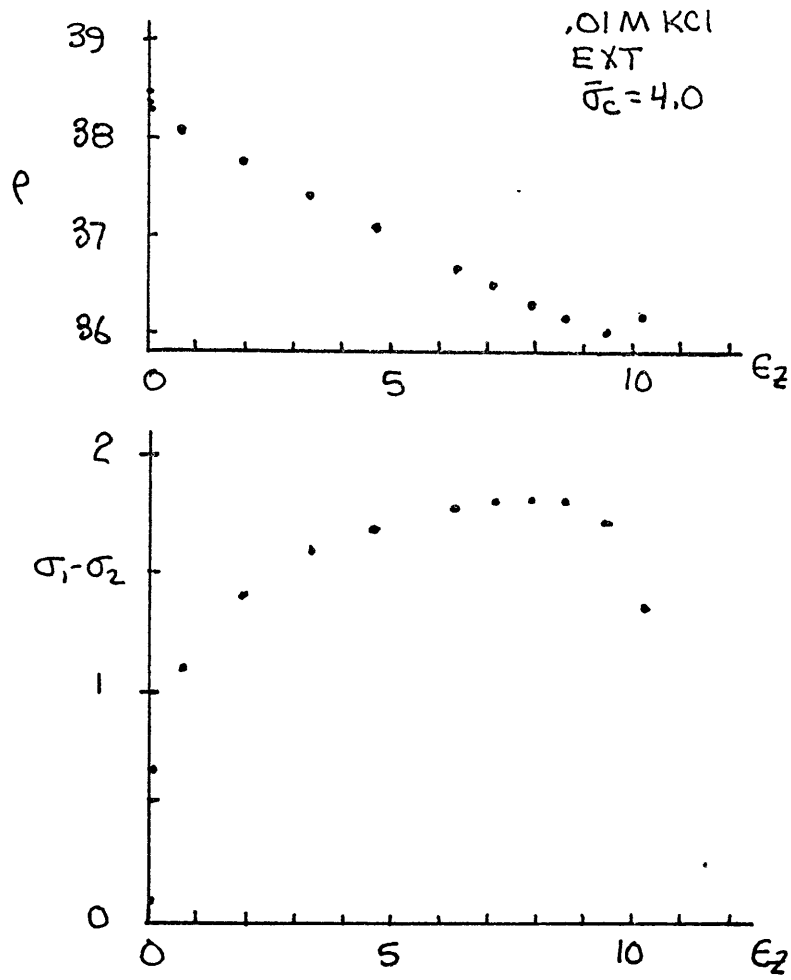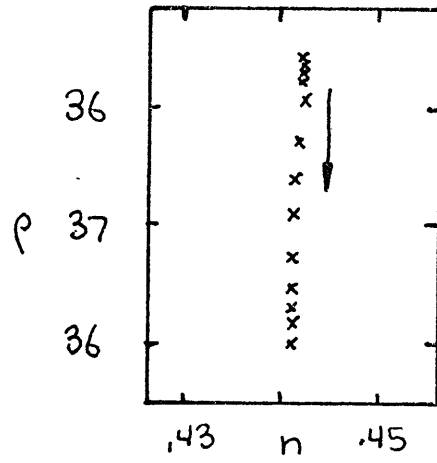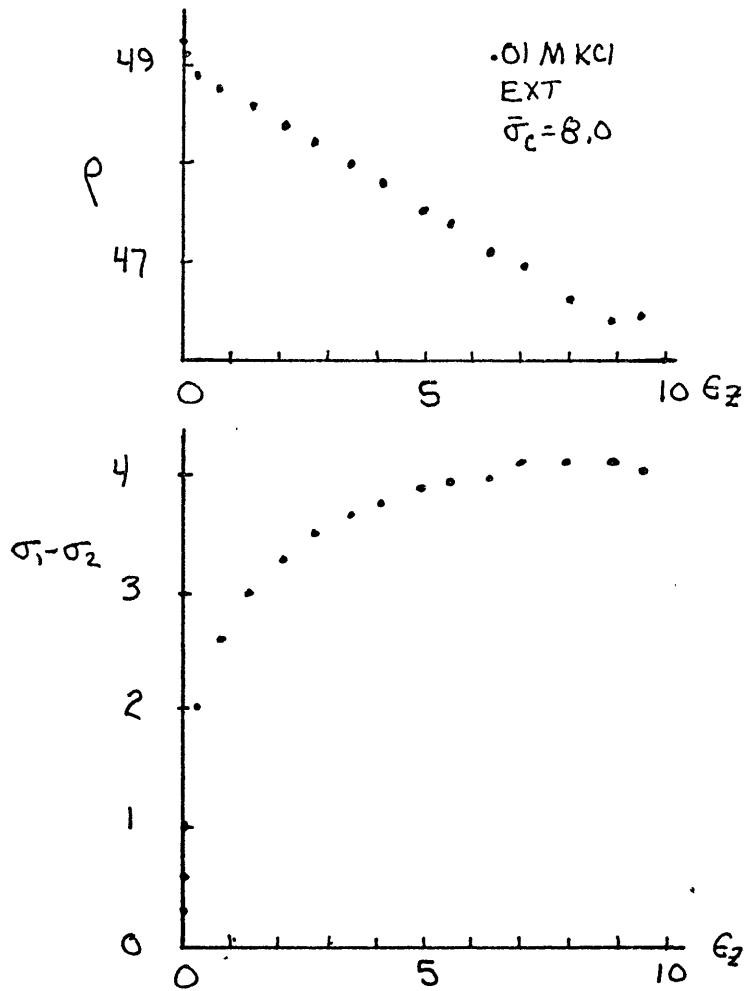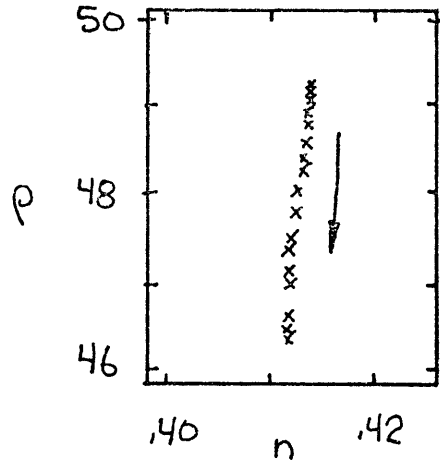
FIGURE B-19 T321 ρ vs n AND ρ,σ₁-σ₂ vs. ϵz

FIGURE B-20 T322   ρ vs n AND ρ, σ₁-σ₂ vs εᵤ

FIGURE B-21   T323 ρ vs. n AND ρ, $\sigma_1 - \sigma_2$ vs. ϵ_z
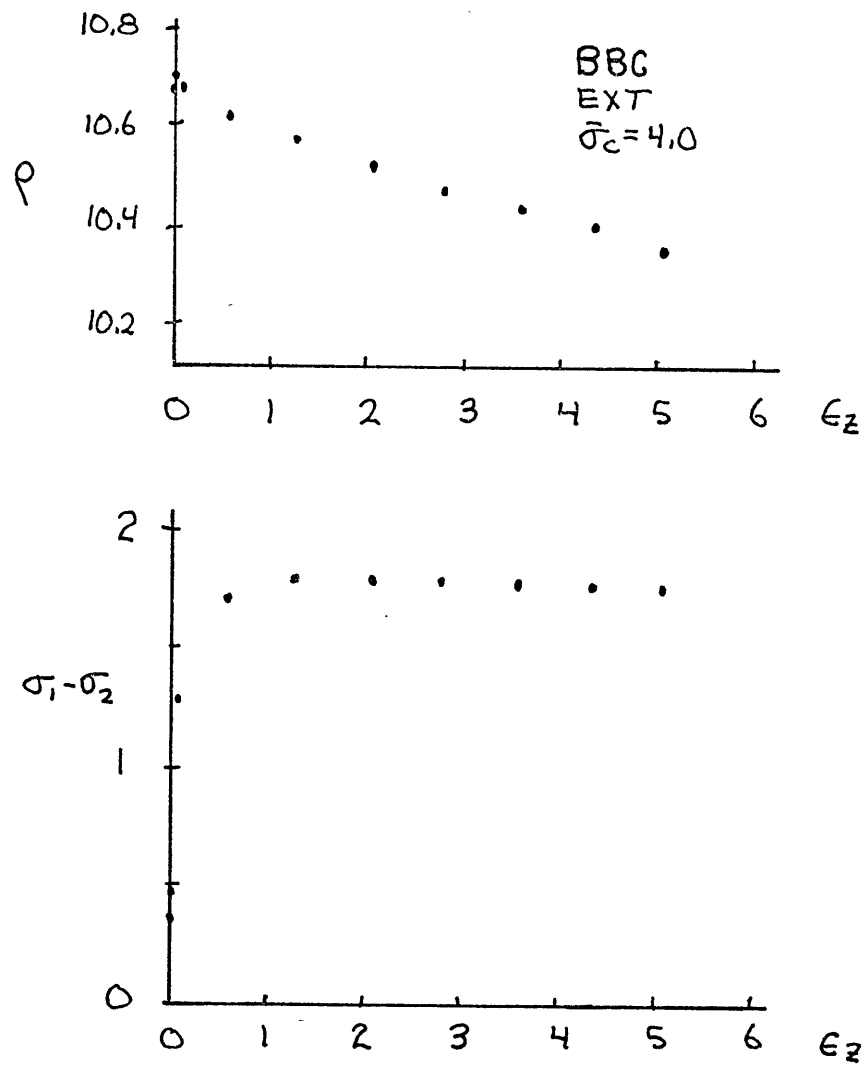
FIGURE 8-22 T324 ρ, $\sigma_1 - \sigma_2$ VS ϵ_z
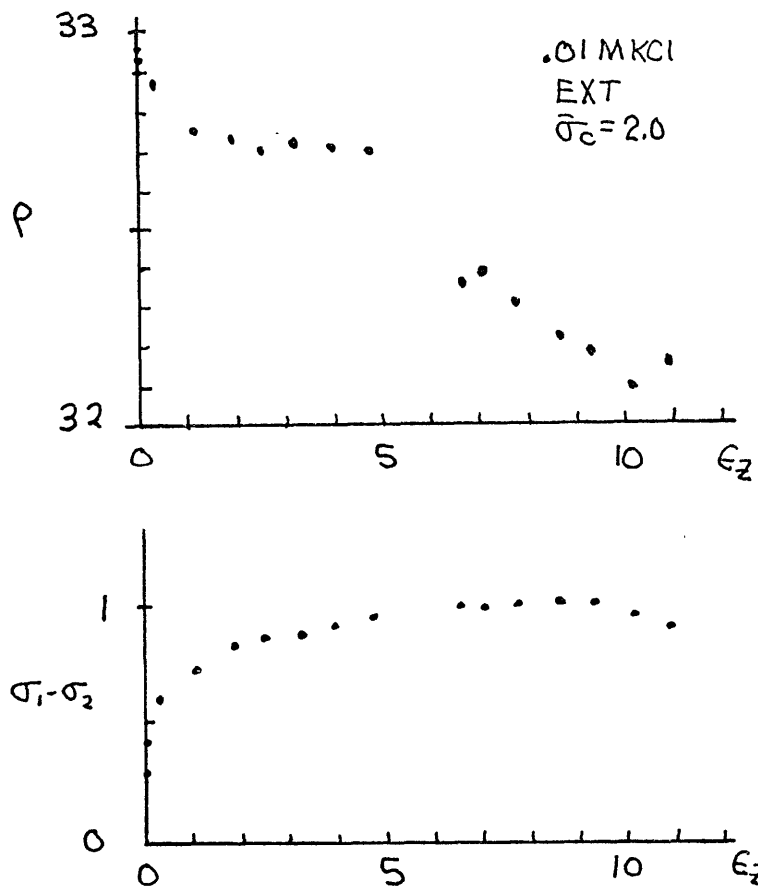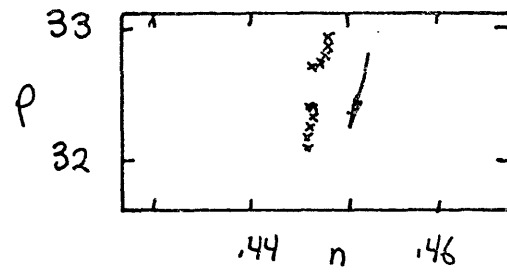
APPENDIX C: ANISOTROPIC PSEUDO-RANDOM NETWORKS

Pseudo-random networks (PRN) are the brainchild of

T. R. Madden (Madden, 1974). They were devised as a means

of investigating conduction properties of rocks. They were

first used to determine whether there was some basic reason

why the exponent in Archie's law should be 2.0 (Greenberg

and Brace, 1969). Besides being useful for studying conduction

properties of geologic materials they can be extended to

the general problem of how mixtures average properties of

the discrete elements which compose them. For example,

what should the seismic velocities of a mixture of quartz

and feldspar be if we know the properties of the individual

minerals? While there are theories which give bounds on

these numbers, the bounds are often so wide that they are

of little practical use (Hashin and Shtrikman, 1962). Pseudo-

random networks offer a much better way of dealing with

these problems.

Let us consider the problem of conduction in a rock

which has anisotropic properties. A small segment of the

rock pores are modelled by a simple network shown in Figure

C-1. The vertical and horizontal conductance of the network

are given by

$$Y_h = \frac{2CD + .5(A+B)(C+D)}{A+B+C+D} \qquad\qquad C-1$$
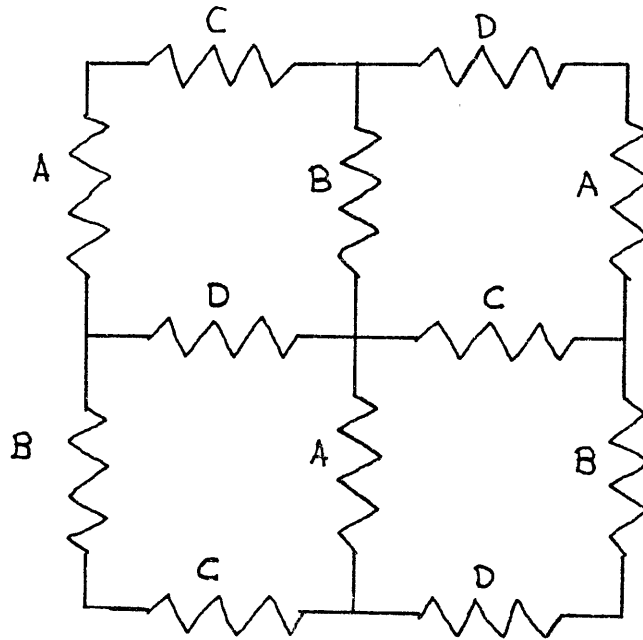
FIGURE C-I   PRN   MODEL OF ROCK PORES

$$Y_v = \frac{2AB + .5(A+B)(C+D)}{A+B+C+D} \qquad \text{C-2}$$

where A, B, C, and D are the element conductances. A distribution function of conductances and probabilities is assigned to the vertical and horizontal elements. These are referred to as the first level distributions Y_v^1 and Y_h^1. We make use of the fact that the vertical and horizontal geometric means

$$\bar{\bar{Y}} = \prod_i Y_i^{P(Y_i)} \qquad \text{C-3}$$

are a good approximate average for the network to follow the convergence of the calculations. The ratio

$$A = \bar{\bar{Y}}_h / \bar{\bar{Y}}_v \qquad \text{C-4}$$

is called the anisotropy ratio. The distribution functions of the network, Y_v^2 and Y_h^2, are now computed by using all possible combinations of A and B taken from the first level horizontal distribution Y_h^1, and C and D from the vertical distribution Y_v^1. This process, called cascading, represents the effect of combining larger and larger segments of the pore system. The cascading is repeated until the vertical and horizontal distributions converge to single values. (The usual convergence test is that the geometric and

arithmetic mean of the distribution differ by only a few percent.) This usually takes half a dozen iterations. The final conductances are called Y_v^C and Y_h^C.

The pseudo-random networks have a basic property of infinite networks in that they open circuit when enough elements are set to zero (removed). The percentage of conduction which remains when this occurs is called the critical probability. Values computed for PRN's agree with Monte Carlo estimates, but they can be computed directly (Madden, 1974). In general, they are a rather good model for rock conduction, while being inexpensive and quick computationally. Several experiments were performed to understand the behavior of anisotropic material. One point of interest is to see the effect of distribution width, as well as cascading on anisotropy.

Uniform logarithmic distributions spanning 2 to 6 orders of magnitude were used. Figure C-2 shows A^C as a function of the first level anisotropy A^1. The first thing to notice is the great dilution of the anisotropy due to cascading. For example, a distribution spanning four orders of magnitude cuts an initial anisotropy of 10. down to 1.41. The effect becomes even greater as the width of the distribution increases. Results of these computations are used in Chapter 2 to determine what is the mechanism causing the resistivity variations during loading of clays.
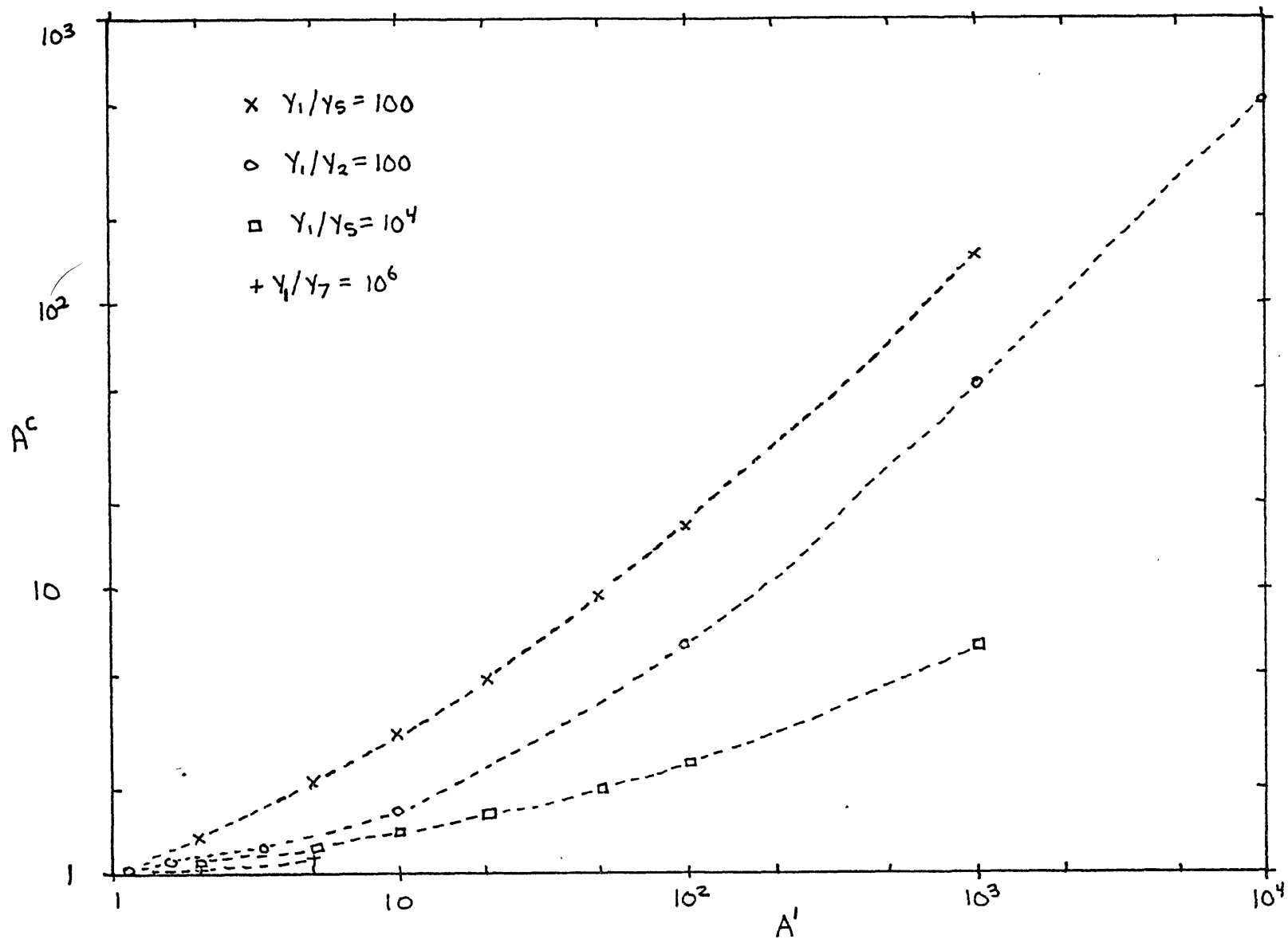
FIGURE C-2 DILUTION OF ANISOTROPY BY CASCADING   ALL DISTRIBUTIONS   LOG-UNIFORM

The legend within the figure:

x $Y_1/Y_5 = 100$

o $Y_1/Y_2 = 100$

□ $Y_1/Y_5 = 10^4$

+ $Y_1/Y_7 = 10^6$

Vertical axis label: A^c

Horizontal axis label: A'

BIOGRAPHICAL NOTE

David V. Fitterman was born in Brooklyn, New York in
1947. Several years thereafter, the bustle and filth
of the City inspired the family to move to Pueblo, Colorado.
Here, the author spent many happy years and received his
primary and secondary education.

Undergraduate study in geophysical engineering was
conducted at Colorado School of Mines. Summer employment
with Kennecott Exploration Inc. introduced the author to
several graduates of the M.I.T. geophysics program and
influenced his choice of graduate school.

Study at M.I.T. began in September 1969. Several
non-geophysical endeavors were engaged in while at M.I.T.
including a hitch-hiking trip across the country and the
construction of an apartment in Cambridge with Ken Anderson.
Most important, the author met his wife, Ruth, a person
of varied talents and interests, at M.I.T.